THE EFFECT OF WHITCOMB WINGLETS AND OTHER WINGTIP MODIFICATIONS ON WAKE VORTICES

by

Henry Frederick Faery, Jr.

Dissertation submitted to the Graduate Faculty of the
Virginia Polytechnic Institute and State University
in partial fulfillment of the requirements for the degree of
DOCTOR OF PHILOSOPHY
in
Aerospace Engineering

APPROVED:

J. F. Marchman, III, Chairman

J. A. Schetz

F. H. Lutze, Jr.

W. L. Hallauer, Jr.

M. Williams

June, 1977

Blacksburg, Virginia

ACKNOWLEDGEMENTS

I wish to express my genuine appreciation for the patient guidance, assistance, understanding, and encouragement offered by Dr. J. F. Marchman, III, my graduate advisor.

Acknowledgement is also given to the following: John Hill and Brian Forstell for their invaluable assistance in model design and building and in the actual conductance of the tests; Dr. George Inger for the idea of testing the Whitcomb winglet; Harry Dawson for his expert technical assistance throughout the entire project; Dr. J. A. Schetz for his infectious enthusiasm and encouragement which brought me to the AOE Department in the first place; and finally to Mrs. Peggy Epperly who so expertly typed the manuscript.

TABLE OF CONTENTS

LIST OF TABLES

LIST OF FIGURES

LIST OF SYMBOLS

A_c	Core radius
AR	Aspect ratio
C_D	Drag coefficient
C_L	Lift coefficient
C_P	Pressure coefficient
C_T	Wingtip chordlength
C_Y	Side force coefficient
$\mathcal{C}_L$	Centerline
K'	Constant dependent on planform and span load distribution
L/D	Lift to drag ratio
L	Lift
Q	Dynamic pressure
R	Vortex radius
V	Velocity
V_∞	Freestream velocity
V_θ, V_{TAN}	Tangential velocity
V_{AXIAL}	Axial velocity
V_Z/V_∞	Normalized axial velocity
V_θ/V_∞	Normalized tangential velocity
V'	Effective or resultant velocity
b_w	Winglet span
c	Chordlength
e	Downstream roll-up distance

s	Wingspan
w_{y_o}	Downwash velocity at point y_o
y_w	Winglet spanwise distance
z/c	Downstream distance in chordlengths
α	Angle of attack
ρ	Mass density
Γ	Circulation
Γ_o	Circulation shed from one side of a wing
θ	Winglet cant or dihedral angle

INTRODUCTION

The hazard presented to aircraft from wake vortex encounters is well-documented. The advent of the "Jumbo-Jet" type aircraft, such as the C-5, Boeing 747, L-1011, and DC-10, brought into focus the need for a system to either alleviate the hazard caused by wake vortices or to detect the location and magnitude of existent wake vortices so that other aircraft could be warned and vectored around their incipient danger. The Federal Aviation Administration has placed its primary efforts into a detection system, whereas the National Aeronautics and Space Administration, in conjunction with academic research facilities and independent laboratories, has concentrated its efforts into wake alleviation devices. Yearly conferences[1,2] are now being convened so that researchers in these fields can report their results and keep future efforts focused along probable avenues of success.

Naturally, the primary focus of the research into wake alleviation methods is directed toward the far-field case. However, it is also essential that thorough research be conducted in the near-field so that definitive, quantitative data is available for evaluating and understanding the entire flow field more precisely. It is only through a combination of research into the near-field fluid flow dynamics and the far-field merging and dissipative patterns that a final wake alleviation solution will be found.

Over the past several years a number of researchers at Virginia Polytechnic Institute and State University have conducted investigations into the effects that wingtip modifications have on wake vortex profiles.[3,4,5] Due to the facilities available, these experimental studies are limited to the near-field wake. The results, however, not only have direct applicability in terms of helicopter rotor wake problems, but they also provide accurate quantitative vortex data to assist in understanding flow dynamics and in directing further research into areas which show promise of providing significant vortex alterations. It is also felt that these near-field results could be extended into far-field vortex research using the convective and turbulent merging models which have been recently developed.[6,7,8,9] In fact, at present it appears that the most promising wake alleviation scheme revolves about the merger of two or more vortices to initiate an early breakdown and subsequent dissipation.

The trailing vortex system results from the flow due to circulation about a lifting wing (Fig. 1). The classic Joukowsky theorem, $L = \rho V \Gamma$, relates lift to circulation. Prandtl lifting line theory models the circulation as a bound vortex on the wing which turns at the wingtips and proceeds downstream. The starting vortex, left behind at the onset of lift, closes the system in accordance with the vortex laws established by Helmholtz. Various wing shapes can be modeled using superposition of such "horseshoe vortex" systems. Further, the downwash at the wing can be determined using the

Biot-Savart law in this system.

Over the years a number of studies have been conducted to determine the changes made to a wingtip trailing vortex due either to a modification of the wing span load distribution or to the introduction of turbulence into the wake. Mass injection experiments by Mason and Marchman[3] had some measure of success, showing that this method of turbulence production caused a reduced tangential velocity and an increased core radius. The injection of turbulence into the vortex through the use of wingtip-mounted splines[10] has been shown to alter the vortex structure by premature aging and dissipation. Uzel and Marchman[4] attached crossed blades, both rigid and spinning, to the wingtip to produce vortex swirl velocity reductions and core size increases. End plates to inhibit vortex roll-up and turning vanes attached at the tip to create counter-rotation to cancel the vortex formation have had little or no success in affecting the vortex.[11]

The more promising approach has been the alteration of the span load distribution to shed multiple vortices which mutually interact to reduce vortex strength, or a combination of this with turbulence production. The use of spoilers[12] to attenuate the vortex is a current project which makes use of this combination effect, and has demonstrated substantial reductions in induced rolling moment on follower aircraft. Ames Research Center is also doing extensive research into modification of flap settings[13] to minimize the wake vortex, again enjoying relative success in merging

vortices and achieving faster dissipation.

Other span load alteration efforts revolve about wingtip modifications. Reduction of the loading gradient at the wingtip has been studied using the ogee tip,[14] designed to prevent the formation of a strong concentrated tip vortex. Two tip configurations, the subwing and the split-tip,[15] producing closely spaced tip vortices have been tested by Tangler with some success in reduction of helicopter blade slap. Turnage[5] studied three simple tip modifications, one of which produced significant peak tangential velocity reductions. This paper examines the fluid flow behavior in the near-field of a wing resulting from several wingtip modifications, focusing primarily on the "Whitcomb winglet".

Although the major claims for the "Whitcomb winglet" center around improved aerodynamic efficiency at cruise conditions, it was felt that an obvious side effect should be a less intense trailing vortex since the winglets are said to reduce the induced drag. In fact, Whitcomb gives his winglets an alternate name, vortex diffusers.[16] Further, it was felt that the winglet should produce multiple wingtip vortices which could possibly merge quickly and cause early demise of the trailing vortex.

Most importantly, if it can be shown that the "Whitcomb winglet" has potential use for reducing the upset hazard to following aircraft, then there exists the possibility of producing the first "positive-work" wake alleviation device. All of the present schemes under investigation, spoilers, flap combinations, splines, etc., are

designed for use primarily in the approach-to-landing environment and they essentially are drag producers. On the contrary, the "Whitcomb winglet" is a thrust producer and a drag reducer, and it is efficient in all regimes of flight. This paper is a first step toward optimization of the winglet for wake alleviation with minimal loss of aerodynamic efficiency. The winglet tangential and axial vortex velocity profiles are analyzed and compared to profiles generated by other wingtip modifications, in particular the tips which were the subject of the Turnage report. Included also are the aerodynamic load characteristics of these tip modifications. Appendix A is a theoretical study of the downwash on the wing with attached winglets.

EXPERIMENTAL PROCEDURE

All experiments were conducted in the VPI&SU 6-Foot Subsonic Wind Tunnel. The tunnel is a continuous, single-return system having a closed 6x6 foot square test section (Fig. 2). Seven anti-turbulence screens upstream of the test section ensure a low level of turbulence. Tunnel speed is controlled by coarse and fine rheostats. For these tests the tunnel speed was kept at 2.2 inches of water using a Barocel Electric Manometer attached to a pitot-static tube placed in a disturbance-free location. Free stream temperature was monitored by a temperature probe on the wall of the test section and recorded on a Digitemp temperature gauge. The pressure in the wind tunnel test section is identical to that of the control room since they are both located inside a pressure-sealed chamber. The static pressure was measured on a Validyne Digital Barometer DB 99.

An untapered NACA 0012 wing of eight inch chord and four foot span was mounted vertically from the test section ceiling of the wind tunnel. This mounting effectively represents a wing of eight foot span with an aspect ratio of 12. The wing was placed at a six degree angle of attack to produce a strong vortex and enable comparison with previous work (Fig. 3 and Fig. 4). The wing was also mounted in the extreme forward part of the test section so that probe measurements of the vortex could be made for downstream distances of up to thirty chordlengths before the flow reached the diffuser

section of the tunnel. The wing was fitted with quarter-chord spanwise pressure taps and chordwise pressure taps immediately adjacent to the tip (Fig. 5).

All of the wingtip modifications were attached to the NACA 0012 wing. The reader is here cautioned that the terminology used to describe some of the wingtip modifications may be misleading. Usually one visualizes the modification as it affects the planform shape. The modifications discussed herein, however, describe the wingtip as seen by an observer looking along the chord line.

The first configuration tested was a simple "square" tip (Fig. 6 and Fig. 7), a tip normally employed on most helicopter rotor blades and also seen on some fixed-wing aircraft. The base configuration was the "round" tip, a half surface of revolution. From a planform view, the "round" tip also has some aerodynamic streamlining. This tip was chosen to represent a very easily manufactured tip which appears on many fixed-wing aircraft, particularly in the general aviation field. The third configuration was a "pointed" tip, which is simply an aerodynamically streamlined tip that is tapered sharply from the top and bottom surfaces toward the centerline. This shape was chosen to determine the effects that a large shear gradient at the tip would have on the vortex velocity characteristics.

The "Whitcomb winglet" was the fourth major configuration tested. The winglet configuration tested was constructed from plans obtained from Dr. Whitcomb in early 1976 and it should be noted that it includes the lower winglet of the original Whitcomb design (Fig. 8).

NASA has, however, now removed this lower portion of the winglet in their present testing and has also changed the cant angles from those of the original design. The remaining two configurations were simply the individual components of the winglet: the winglet base with the upper winglet only; and the winglet base with only the lower winglet. It should be noted that the "round" tip served as the winglet base.

The trailing vortex behind each of these wingtip configurations was probed at five and twenty chordlengths downstream by a 1/8 inch diameter five-hole yawhead probe. The probe was custom built by United Sensor Corporation for such experiments. As shown in Figure 9, the probe has one hole in the middle of the point and two holes opposite each other in the horizontal and vertical planes. By measuring pressure differences between opposite holes in the same plane the angle of the flow can be determined. The probe has demonstrated a linear response over a range of ± 10 degrees. The small holes and long pressure leads used in the test caused the pressure difference read on the manometers to slowly reach an equilibrium state. This slow response required a tunnel test time of almost one hour for each complete traverse of a vortex at any downstream station.

The probe traversing mechanism consisted of an existing traverse that provided both horizontal and vertical movements of up to four feet. The traverse is shown in Figure 4. An adapter unit (Fig. 10) was added to this traverse mechanism to allow the probe to rotate in pitch and yaw about its point. The unit was designed to

be rigid in intensely swirling flows while presenting minimal disturbance to the flow field at the point of the probe. One RPM motors provided power for probe rotation in pitch and yaw at sufficiently slow speeds to ensure positive control of the probe position (Fig. 11).

Five inclined manometers, each containing a red manometer oil with a specific gravity of .826, were used for this test. The total pressure was measured on a Dwyer manometer that was incremented in intervals of 0.02 inches of water. The total pressure was referenced to the freestream static pressure. Pressure differences in the horizontal plane were measured on two Dwyer manometers, also graduated in 0.02 inches of water. The manometers have an operating range of ± 1.1 inches of water. Vertical plane flow angularity was measured in the same manner as that of the horizontal plane. All manometers were operated using the pitot-static tube that was standard for the test. All pressure lines were standard thick-wall plastic tubing.

The procedure for the investigation of the trailing vortex was straight forward. Prior to mounting the wing for each downstream test station, the probe was aligned with the freestream by pitch and yaw movements until the pressure readings were equal on the pairs of manometers measuring pressure in the vertical and horizontal planes. The wing was then mounted in the tunnel and the wingtip attached. The vortex center was then located by moving the probe vertically until the flow yaw angle was found to be zero, and then traversing the probe laterally until the pitch angle was found to be zero. It

was necessary in several cases, particularly with the Whitcomb winglet configurations, to use a tuft grid to more quickly locate the vortex for probe insertion. Because of symmetry, the vortex center occurs where both the pitch and yaw angles are zero and the center pressure hole is reading a value close to the freestream total pressure. Once the vortex center was found, a vertical traverse was made starting from the center and proceeding six to seven inches above the center, or inboard on the wing span. A similar traverse was then made by returning to the center and travelling six to seven inches below the vortex core. This return to the center location also provided an indication of any vortex movement due to the probe movements. Spanwise measurements for this study were taken at the five and twenty chordlength stations downstream, with sample observations also made at other downstream test locations. It was encouraging to note that the previous work done by Mason and Turnage was repeatable with excellent accuracy at each of six stations from five to thirty chordlengths downstream. At the completion of each vortex traverse, the spanwise and chordwise pressure measurements on the wing surface were obtained. A Hewlett Packard 3476B digital multimeter connected to a Scanivalve P. Ducer Osc-Carrier Amplifier and pressure tubing through a 24 outlet Model D Scanivalve was used for this purpose.

The experimental vortex information was obtained in the form of pressure measurements from the yawhead probe and probe position measurements for displacement from the vortex core. Data points were established at very close intervals, .036 inches, within the vortex

core, and spaced at larger intervals outside the core. From this information, the angularity of the flow and the local static and dynamic pressures could be determined using previous work done by Mason using this same system. Mason developed a computer program and plotting routine to reduce the data obtained by this test and display it. Of necessity, the static pressure in the vortex field had to be obtained from the yawhead pressure measurements. A method described by Winternitz[17] was used for this purpose and proved to give consistent results with the pressure predicted from inviscid considerations and high repeatability. The necessary computations and considerations are well described in Mason's paper and do not need to be repeated here.

Several general assumptions are made in the development of the data reduction scheme. Inviscid theory is used, based on the original work of Betz. The flow is assumed incompressible since the Mach number never exceeded 0.1. The vortex path is assumed to parallel the freestream path. This is consistent with earlier work[18] showing that after a distance of a few chordlengths downstream of the wing the vortex travels parallel to the freestream. This study makes no conclusions as to the path of the vortex due to wall interference, although in the analysis of flow properties at the test station it is assumed that the walls have no effect. This seems justified since the vortex cores are at least 20-24 core diameters from the nearest wall. Any pressure gradient in the freestream direction would have an effect on the vortex, but the VPI 6-Foot Tunnel has a negligible

streamwise pressure gradient throughout the entire test section. The Reynolds number for all tests was approximately 370,000.

As a follow-up to these vortex profile tests, it was decided to attempt to correlate the wingtip effects on the trailing vortex with the wingtip effects on the wing aerodynamic forces. The identical wingtip modifications were mounted on a smaller aspect ratio (AR = 5), similar wing to compare their lift and drag characteristics. This wing was also placed at a six degree angle of attack and force readings were obtained through a sting-mounted six-component strain gauge balance (Fig. 12 and Fig. 13). The strain gauge balance was a SB-100 manufactured by Modern Machine and Tool Co. Normal, axial, and side force readings were obtained using Hewlett Packard 3476B Digital Multimeters (Table 1). Spanwise pressure measurements were also obtained for these wing setups. Figure 14 shows the pressure tap system for this wing.

Additionally, the aerodynamic forces were measured on the unattached winglet to assist in determining its contribution to the wing with attached winglet configuration. This test was followed by tests to determine the aerodynamic force effect of the winglet on the wing and the wing on the winglet. A yoke was constructed of heavy rigid steel bars and the winglets were attached to this yoke. The wing was then mounted on the balance system and the forces measured without the presence of the winglets. The winglet yoke was then mounted on the wind tunnel floor, but not attached to the balance system (Fig. 15a). This arrangement placed the winglets in their

proper location but not touching the wing itself. An oil film was used to seal the minute gap between the winglet and the wing to prevent airflow through the gap. Then the forces were once again measured on the wing to determine the changes due to the presence of the winglets. Lastly, the winglet was placed on the balance system to obtain the aerodynamic forces generated by the winglet alone. Following this test the wing was mounted on the tunnel floor, but not attached to the balance system or the winglet. As before, this arrangement placed the wing in its proper position although the wing was not attached nor touching the winglet (Fig. 15b). Once again an oil film was used to seal the gap between wing and winglet. This time the forces were measured on the winglet to determine the changes due to the presence of the wing. Table 2 presents the data obtained from these tests.

The final tests conducted were purely qualitative. The wing with attached winglet was submerged about one-third spanlength into a towing tank and towed at an arbitrary speed and angle of attack to attempt to obtain a reasonable flow visualization picture of the interaction of the two winglet vortices, particularly in the far-field. Dye ejection ports were placed on the upper winglet tip and the upper wing surface near the tip to mark the individual vortices. Blue dye was used for the winglet tip vortex and red dye for the wing vortex (Fig. 16).

RESULTS AND DISCUSSION

Vortex Study

The experimental vortex data is presented using the familiar plots of the vortex tangential and axial velocities versus vortex radius. Figure 17 compares a typical experimentally-obtained tangential velocity profile (square tip) with a predicted profile based on the inviscid theory of Betz and also with an empirical prediction proposed by McCormick.[19] It is obvious that the experimental results provide very adequate correlation with theory. Figure B-1 in Appendix B illustrates the coordinate system for this study.

Figures 18-23 present the tangential velocity profiles for the square, pointed, and round tips at the five and twenty chordlength downstream test locations. Since this study uses the round tip as the "base" tip then a look at its characteristic profile at the two downstream test locations provides a datum from which to discuss the experimental findings (Fig. 24). The vortex is slightly non-symmetrical at the five chordlength position due to two effects: first, the vortex is still in the roll-up stage; secondly, the interaction between the inboard side of the vortex and the downwash immediately behind the wing has a tendency to increase the tangential velocities on the inboard side. At twenty chordlengths downstream the vortex has essentially rolled up, is very symmetrical, and presents almost negligible change in core size. A look at the other figures will show that this is typical of most of the tip modifications studied.

A study of the radial circulation distribution for the various wingtips (Fig. 25 and Fig. 26) indicates that each vortex has completed the roll-up process by the twenty chordlength position. In fact, this is in excellent agreement with a theoretical prediction presented by Spreiter and Sacks.[20] They predicted roll-up to occur in accordance with

$$\frac{e}{c} = \frac{K'}{C_L}$$

Their calculations were based on the theoretical span load distribution calculated by Glauert using Prandtl lifting-line theory, and depend upon both aspect ratio and the span load distribution. For these experiments, predicted roll-up occurred between 17 and 20 chordlengths downstream, depending on the wingtip modification.

Further, a comparison of experimental results for the determination of Γ_o, the circulation shed from one side of a wing, with the analytical result presented by both Spreiter and Sacks and Corsiglia, et al,[21] shows excellent agreement for all wingtips studied. Analytical results based on

$$\Gamma_o = \frac{1}{2} C_L V_\infty c$$

predict values between 15.85 ft^2/sec and 18.97 ft^2/sec, values verified by the experiment. A similar elliptically-loaded wing, using

$$\Gamma_o = \frac{4sV_\infty C_L}{\pi AR}$$

would have a base circulation of 20-24 ft^2/sec for the same conditions.

The remainder of the discussion will primarily focus on the results determined at the twenty chordlength position, which is outside the roll-up region. Figure 27 presents a comparison of the round tip with the simple square and pointed tips at this location. Of significant note is the 27% reduction in maximum tangential velocity produced by the pointed tip. It should be further noted that this change is accompanied by a 5.8% reduction in core size, a fact which contradicts observations of some previous studies.[3,4] In those studies it was speculated that there was a trade-off between core size and swirl velocity magnitude. If one increased, then the other decreased in order to account for a constant energy within the vortex system. Here, however, a higher energy system is producing a lower velocity vortex with a tighter core. (The circulation shed by the pointed tip is about 9% higher than that shed by the round tip.) These reductions in tangential velocity and core size also seem to have little effect on the velocities in the induced flow around the vortex core.

Figures 28-33 present the axial velocity profiles for the pointed, round/base, and square tips at both test locations. These axial velocity profiles are compared in Figure 34 for the same three tip modifications. Although all three profiles exhibit a velocity deficit in the core, the pointed tip is the only one to show virtually no velocity excess at all. Perhaps this one feature is part of the

explanation for the significant reductions in tangential velocity and verifies Bilanin's[22] contention that deficits in axial velocity result in a reduction of the centerline swirl velocity. It is also conjectured that the large shear gradient imposed at the pointed tip is a major causative factor in this vortex behavior.

Figures 35-38 present the tangential velocity profiles for the Whitcomb winglet. Figures 39 and 40 combine these profiles in order to depict their relationship to the winglet and position with respect to each other and the winglet. In investigating the contributions of the individual components of the winglet on the vortex it was found that three individual vortices of like sign (same rotation direction) are produced; one vortex is shed at the tip of the upper winglet, one is shed at the juncture of the wing with the winglet, however the vortex shed from the tip of the lower winglet immediately merges with the main wing vortex. Unlike a previous report[23] which stated that "the addition of the winglets spreads the vorticity...to such an extent that a discrete vortex core is not apparent", this study shows two distinct vortices which persist for the entire downstream distance measured. In fact, a tow tank observation shows that the two vortices persist downstream for quite some distance, wrapping around each other. This clockwise rotation (as viewed upstream at the left wingtip) is evident in Figures 39 and 40. Also apparent at the twenty chordlength position is the interference of the two vortices with each other. For comparative purposes, the maximum swirl velocities in each of the two vortices at the twenty chordlength

position is about 64% less than that of the round or base tip. Each of the vortices also has a smaller core than the round tip, although once again the circulation shed by this wingtip modification is considerably higher than the rounded tip. In fact, the winglet system shed the most circulation of any tip modification studied.

Figures 41-44 present the axial velocity profiles for the two vortices produced by the Whitcomb winglet. The relative positions and movement of the vortices are depicted in Figures 45 and 46. Once again it should be observed that each vortex contains only a strong deficit in axial velocity, with no velocity excess in the core. It seems that a strong axial deficit is associated with a reduction in tangential velocity.

As previously noted, tests were also run using the wing with only one part (upper winglet or lower winglet) of the original Whitcomb design. The tangential velocity profiles for the two vortices produced by the upper winglet are presented in Figures 47-50, with their spatial relationship shown in Figures 51-52. Several points can be made concerning the effects of this configuration. First, the maximum swirl velocities have been even further reduced. Secondly, vortex #1 contains an uncharacteristic vortex core spread that has not been seen on the previous tip modifications. Thirdly, once again the axial velocity profiles exhibit a strong deficit (Figs. 53-56).

These last two observations are also obvious in the vortex profiles of the lower winglet contribution (Figs. 57-61). Although

the swirl velocity reduction with the lower winglet only is not as great as that with either the upper winglet or with the total winglet, the vortex core expansion is seen to occur. In fact, the lower winglet configuration produces the most dramatic core size increase of all the tip modifications studied (Fig. 63).

The variation in vortex core size becomes more apparent in the bar graphs depicting development of maximum swirl velocities and core sizes (Figs. 62-63). As has been well-documented there is a trade-off between swirl velocity decay and core size increase with downstream distance. However, this experiment does not show that this trade-off occurs so as to keep the product of $V_{\theta max}$ and core radius a constant.[19] It is possible that this relationship does not have validity for this experiment since all data was collected in or immediately aft of the roll-up region. It can also be shown, that for this experiment, the vortex decay rate more closely approximates that predicted by Brown[24] of $A_c \sim z^{2/3}$ and $V_{\theta max} \sim z^{-1/3}$ instead of the standard prediction of $A_c \sim z^{1/2}$ and $V_{\theta max} \sim z^{-1/2}$.

The bar graphs clearly show that: (1) the upper winglet alone is superior to the total winglet, in fact is superior to all modifications studied, in reducing the maximum tangential velocities; (2) the upper winglet vortex cores are substantially more spread than those of the total winglet; (3) the lower winglet alone is nearly as effective as the total winglet in reducing the maximum swirl velocity and has considerably more vortex core spread as it moves downstream. Of course, the lower winglet only produces one

distinct vortex, whereas the upper winglet and the total winglet each produce two distinct vortices. This fact alone makes comparison difficult, as in trying to compare the winglet configuration results to those of the round, square, or pointed tips. It would seem, however, preferable to produce multiple vortices of lesser intensity rather than a single, more intense vortex. Twin vortices provide the possibility of destructive merger; or, if remaining distinct until dissipation, these less intense vortices should present less roll-upset potential to following aircraft.

The two most promising alleviation devices currently being studied by NASA use this principle of vortex merger to reduce the rolling moment hazard to follower aircraft. These schemes are the spoiler configuration under investigation by Croom[25] and the reconfiguration of currently existing flaps to reduce the wake hazard during landing operations.[20] Unfortunately, these alleviation schemes are useful only in the landing configuration and they degrade from the performance of the aircraft. On the contrary, the Whitcomb winglet (as will be shown later) is useful throughout the entire flight regime and improves aircraft performance.

Of particular interest was a paper presented by Rossow[26] at the recent Wake Vortex Conference in Boston. He has conducted theoretical studies on flat plate fins attached at various locations on the upper or lower surfaces of a wing, and at varying cant angles. His analytical results predicted that a fin producing a vortex of opposite sign to that produced by the main wing would cause merger of

the two vortices more quickly and also faster dissipation. However, experimental work supporting Rossow's research does not show this to be the case. The experimental study indicated that two vortices of like sign would be more effective in reducing the roll-upset potential. This seems to support the work of this study. The Whitcomb winglet does produce a vortex of the same rotation as the main wing, but with one important difference; Rossow's flat plate fins are drag producers, whereas the Whitcomb winglet is a drag reducer and thrust producer.

Aerodynamic Force Study

No discussion of wingtip modifications, particularly the Whitcomb winglet configuration, would be complete without some reference to the aerodynamic performance of these tips. However, before analyzing the results of the aerodynamic force tests, it seems appropriate to discuss the purpose of the Whitcomb winglet and the rationale behind its design. The following remarks are a summary of Whitcomb's report.[16]

The winglets are small, nearly vertical, airfoil shaped, wing-like surfaces mounted at the tips of a wing. They are intended for use in subsonic flight conditions and their purpose is to reduce the drag coefficient by an amount greater than a simple wingtip extension with the same structural weight penalty. As seen in Figure 8, the primary surface is located rearward above the main wingtip with the smaller secondary surface placed forward below the tip. The upper winglet is placed rearward so that the increased velocities over the

inner surface of the winglet are not superimposed on the high velocities over the forward region of the wing upper surface, thus reducing adverse flow interference effects. The lower winglet is placed forward to help reduce the induced velocities over the upper winglet's inner surface at high wing lift coefficients. This is analogous to the placement of a slat near the leading edge of a wing. In both cases the local angle of flow at the leading edge is reduced.

To be fully effective the vertical surfaces at the tip must efficiently produce significant side forces to reduce the lift-induced inflow above the wingtip or the outflow below the tip. Thus the winglet airfoil shape, sweep, taper, incidence, and cant are predicated on this requirement for inward normal force loads. For the most satisfactory results the required normal force coefficients for the winglet should be limited to values of the same order of magnitude as the main wing lift coefficient.

The winglet airfoil is shaped to meet two requirements: (1) it should efficiently provide the desired normal force coefficient for the design wing lift coefficient and Mach number; (2) the airfoil should be shaped so that the onset of significant boundary-layer separation on the winglet surface is delayed to the conditions for which such separation occurs on the wing. The NASA general aviation airfoil has been used to meet these objectives. The upper winglet is toed out and thus has negative geometric incidence, since the effective inflow angles are greater than the winglet angles of attack required to achieve the desired normal force coefficient for design

conditions. The lower winglet is toed in for the same purpose. Outward cant of both surfaces satisfies trade-offs between induced drag reduction, skin friction, and wing bending moments. It also reduces the flow interference at the root of the winglets. Substantial taper is required to keep the normal force coefficient approximately constant along the span of the winglet. The effective sweep should be about the same as the main wing, for supercritical design conditions. The height of the upper winglet was arbitrarily chosen and is a compromise between aerodynamic and structural considerations. The lower winglet is shorter because of ground clearance considerations in takeoff and landing.

During his tests, Whitcomb achieved reductions in induced drag of about 20% with a resulting increase in wing lift-drag ratio of about 9%. This was for the design Mach number of 0.78 and near the design lift coefficient.

Figure 64 presents the results of tests done for this study. The lift-drag ratio comparison illustrates dramatically the improvement in aerodynamic efficiency produced by both the total winglet and the upper winglet alone. At the maximum lift-drag ratio for the winglet there is a 17% increase in L/D over that of the round tip, with an accompanying 15% reduction in drag coefficient. Even at this low test Reynolds number these experiments verify most of the trends in aerodynamic improvement presented in Whitcomb's paper. At higher lift coefficients than C_L = 0.55 even greater reductions in drag coefficient were measured although the lift-drag ratio improvement

is smaller. The lower winglet provides marginal improvement at all lift coefficients, but its performance is surpassed by that of the pointed tip.

Figures 65 and 66 are presentations of the test results for the winglet effects on the wing and vice-versa. It is evident from Figure 65 that the improvement in aerodynamic performance caused by the winglet attached to the wing is better than the sum of its components. The C_L and L/D for the wing/winglet system is larger than the sum of the wing and winglet contributions separately, and the C_D for the combination is smaller. In examining Figure 66a it is apparent that although the presence of the winglet slightly increases the drag coefficient for the wing, the accompanying lift coefficient increase more than offsets this, resulting in an overall increase in lift-drag ratio. Figure 66b shows the dramatic effects of the presence of the wing on the winglet. The spanwise flow off the wing effectively increases the winglet lift coefficient fourfold, and does even better in decreasing the winglet drag coefficient. As a result the winglet L/D is boosted remarkably. This can be easily explained using the schematic drawing of the winglet forces in Figure 67. The spanwise flow around the wingtip effectively provides a large change in angle of attack on the winglet due to the vortex velocity component V_0. This is exactly analogous to the effect of the downwash on the freestream velocity component. An optimally designed winglet angle of attack could result in a net thrust (negative C_D) as well as higher lift.

Theoretical work done by Whitcomb indicates that to achieve the reduction in induced drag desired by the winglets requires not only substantial inward normal loads on the winglets but also significant increases in the upward loads on the outboard section of the wing. It can be seen that the winglets have the effect on the wing of increasing the loading on the outboard section of the wing. A look at the spanwise pressure distribution along the quarter chord for the various wingtip configurations verifies this more clearly (Fig. 68). The pressure distributions for the total winglet and the upper winglet alone are nearly the same and substantially higher on the outboard section of the wing than that produced by the round or square tips. Of interest is the nearly identical distribution for the pointed tip and lower winglet configurations. A comparison of these pressure distributions with the vortex profiles clearly indicates that a reduction in maximum swirl velocity appears to be linked to a span load increase near the tips.

Tow Tank Study

The observations made through the flow visualization study in the towing tank are summarized by the sketch in Figure 69. As stated previously, the two vortices from the winglet were marked with different color dyes in order to observe their interaction in the far-field. The vortices remained distinct for quite some downstream distance, with the winglet tip vortex rotating about the main wing vortex. The main wing vortex appeared undisturbed throughout most of this process. The tip vortex tended to stretch itself about the

main vortex and eventually diffused so that only the main wing vortex remained, and even it looked somewhat dissipated. Essentially it appeared that about half of the vorticity had been dissipated far downstream, a very significant achievement in terms of reducing the rolling moment hazard to following aircraft. There were also some indications of the sinusoidal Crow instability being initiated in the break-up process.

CONCLUSIONS AND RECOMMENDATIONS

A wind tunnel investigation has been conducted on six different wingtip configurations to determine their vortex characteristics in the near-field and their aerodynamic performance over a limited range of angles of attack. The Whitcomb winglet has been compared with its components and with three simple tip modifications. Several conclusions can be reached:

1. Either the Whitcomb winglet or the upper winglet configuration is superior in all aspects to the tip modifications studied.

(a) The winglet's 17% increase in lift-drag ratio, coupled with a 15% reduction in drag coefficient, further substantiate its contribution to aerodynamic performance improvement.

(b) The 64% reduction in maximum tangential velocity is a significant achievement. Additionally, it is felt that the twin vortices of lesser intensity have greater potential for wake-alleviation research efforts than a single vortex of larger combined intensity.

2. When comparing the winglet results with those of the upper winglet alone, it would appear that the latter configuration has more promise. Its vortices are less intense and one of them has a tendency for early decay. The lift-drag ratio increase and drag coefficient reduction are very comparable to the total winglet.

3. The lower winglet configuration shows remarkable ability to decrease the vortex tangential velocity and cause early decay.

However, its aerodynamic performance improvement is marginal.

4. The pointed tip is very effective in reducing the vortex swirl velocities and also does well in improving aerodynamic efficiency. It is felt that the large shears produced as the flow goes around the pointed wingtip result in vortex velocity reduction and dissipation in much the same manner as the shears caused by the interaction of vortices from the Whitcomb winglet.

5. Further investigation should be made into the use of both the pointed tip and the lower winglet configuration for helicopter blades. They have possible potential in reducing rotor noise and improving blade efficiency.

6. It is felt that fruitful research can be done into optimization of the upper winglet configuration. Analytical merger models, particularly the new Rossow model, should be applied to determine if more rapid vortex dissipation can be produced. The far-field vortex pattern of the upper winglet should be analyzed in facilities capable of this testing. Such testing and analysis could possibly produce an optimum vortex diffuser at minimum loss of current aerodynamic improvement.

REFERENCES

1. Wake Vortex Minimization Conference, sponsored by NASA, Feb. 1976, Washington, D.C.

2. Wake Vortex Conference, sponsored by Department of Transportation, March 1977, Boston, MA.

3. Marchman, J. F. and Mason, W. H., "Farfield Structure of an Aircraft Trailing Vortex Including Effects of Mass Injection," NASA Report CR-62078, April, 1972.

4. Marchman, J. F. and Uzel, J. N., "The Effect of Wing-Tip Modifications on Aircraft Wake Turbulence," College of Engineering, VPI and SU, VPI-E-72-8, July, 1972.

5. Turnage, J. O., "Tip Modification Effects on Helicopter Rotor Vortices," Masters Thesis, College of Engineering, VPI and SU, August, 1975.

6. Rossow, V. J., "Convective Merging of Vortex Cores in Lift-Generated Wakes," AIAA Paper No. 76-415, San Diego, July, 1976.

7. Rossow, V. J., "Theoretical Study of Lift-Generated Vortex Wakes Designed to Avoid Roll Up," AIAA Journal, Vol. 13, No. 4, April, 1975, pp. 476-484.

8. Bilanin, A. J., Teske, M. E., Donaldson, C. duP. and Snedeker, R. S., "Viscous Effects in Aircraft Trailing Vortices," NASA Symposium on Wake Vortex Minimization, Washington, D.C., Feb., 1976, pp. 55-122.

9. Bilanin, A. J., Teske, M. E., and Williamson, G. G., "Vortex Interactions and Decay in Aircraft Wakes," ARAP (submitted for publication AIAA Journal), July, 1976.

10. Patterson, J. C., Jr., Hastings, E. C., Jr., and Jordan, F. L., Jr., "Ground Development and Flight Correlation of the Vortex Attenuating Spline Device," NASA Symposium on Wake Vortex Minimization, Washington, D.C., Feb. 25 and 26, 1976, pp. 275-302.

11. Dunham, R. E., Jr., "Exploratory Concepts Found to be Unsuccessful for Aircraft Wake Vortex Minimization," NASA Symposium on Wake Vortex Minimization, Washington, D.C., Feb. 25 and 26, 1976, pp. 218-257.

12. Croom, D. R., "The Development of the Use of Spoilers as Vortex Attenuators," NASA Symposium on Wake Vortex Minimization, Washington, D.C., Feb. 25 and 26, pp. 337-370.

13. Corsiglia, V. R. and Dunham, R. E., "Aircraft Wake-Vortex Minimization by Use of Flaps," NASA Symposium on Wake Vortex Minimization, Washington, D.C., Feb., 1976, pp. 303-336.

14. Landgrebe, A. J. and Bellinger, E. D., "Experimental Investigation of Model Variable-Geometry and Ogee Tip Rotors," Preprint No. 703, 29th Annual National Forum of the American Helicopter Society, May, 1973.

15. Tangler, J. L., "The Design and Testing of a Tip to Reduce Blade Slap," Preprint No. 963, 31st Annual National Forum of the American Helicopter Society, May, 1975.

16. Whitcomb, R. T., "A Design Approach and Selected Wing-Tunnel Results at High Subsonic Speeds for Wing-Tip Mounted Winglets," NASA TN D-8260, July, 1976.

17. Winternitz, F. A. L., "Probe Measurements in Three-Dimensional Flow," Aircraft Engineering, August, 1956, p. 273.

18. Mason, W. H. and Marchman, J. F., "Investigation of an Aircraft Trailing Vortex Using a Tuft Grid," College of Engineering, VPI and SU, VPI-E-71-17, August, 1971.

19. McCormick, B. W., Tangler, J. L., and Sherrieb, H. E., "Structure of Trailing Vortices," Journal of Aircraft, Vol. 5, No. 3, May-June, 1968, pp. 260-267.

20. Spreiter, J. R. and Sacks, A. H., "The Rolling Up of the Trailing Vortex Sheet and Its Effect on the Downwash Behind Wings," Journal of the Aeronautical Sciences, Vol. 18, Jan., 1951, pp. 21-32.

21. Corsiglia, V. R., Schwind, R. G., and Chigier, N. A., "Rapid Scanning, Three-Dimensional Hot-Wire Anemometer Surveys of Wing-Tip Vortices," Journal of Aircraft, Vol. 10, No. 12, Dec., 1973, pp. 752-757.

22. Bilanin, A. J. and Donaldson, C. duP., "Estimation of Velocities and Roll-Up in Aircraft Vortex Wakes," Journal of Aircraft, Vol. 12, No. 7, July, 1975, pp. 578-585.

23. Flechner, S. G., Jacobs, P. F., and Whitcomb, R. T., "A High Subsonic Speed Wind-Tunnel Investigation of Winglets on a Representative Second-Generation Jet Transport Wing," NASA TN D-8264, July, 1976.

24. Brown, C. E., "Aerodynamics of Wake Vortices," AIAA Journal, Vol. 11, April, 1973, pp. 531-536.

25. Croom, D. R., "Low-Speed Wind Tunnel Investigation of Various Segments of Flight Spoilers as Trailing-Vortex-Alleviation Devices on a Transport Aircraft Model," NASA TN D-8162, March, 1976.

26. Rossow, V. J., "Alleviation of Lift-Generated Wakes by Vortex Merger and Dispersion," DOT Wake Vortex Conference, Boston, MA, March, 1977.

27. Blackwell, J. A., Jr., "Numerical Method to Calculate the Induced Drag or Optimum Loading for Arbitrary Non-Planar Aircraft," NASA SP-405, May 17, 1976, pp. 49-70.

28. Feifel, W. M., "Optimization and Design of Three-Dimensional Aerodynamic Configurations of Arbitrary Shape by a Vortex Lattice Method," NASA SP-405, May 17, 1976, pp. 71-88.

29. Lundry, J. L., "A Numerical Solution for the Minimum Induced Drag and the Corresponding Loading of Nonplanar Wings," NASA CR-1218, Nov. 1968.

30. Ishimitsu, K. K., Van Devender, N., Dodson, R., "Design and Analysis of Winglets for Military Aircraft," Wright Aeronautical Laboratories Rpt. No. AFFDL-TR-76-6, 1976.

31. Kuethe, A. M. and Chow, C., Foundations of Aerodynamics, John Wiley and Sons, New York, 1976.

32. Pope, A., Basic Wing and Airfoil Theory, McGraw Hill Book Company, Inc., New York, 1951.

APPENDIX A

DOWNWASH STUDY

APPENDIX A

DOWNWASH STUDY

Background

As a complement to this experimental vortex study it was decided to attempt to determine theoretically the effects of the winglet lift distribution on the main wing downwash pattern and the effect of different winglet cant (or dihedral) angles on the same downwash pattern. A number of investigators, notably Blackwell,[27] Feifel,[28] Lundry,[29] and Ishimitsu,[30] have made theoretical studies on the design loading of non-planar wings to achieve minimum induced drag. Their studies have looked at the wing-winglet problem using the vortex lattice method, a very powerful mathematical tool for three-dimensional potential flow analysis. The vortex lattice method appears to be an extremely valuable tool to predict near-field induced drag in order to optimize the aerodynamic load distribution over the wing.

However, for this study it was obvious that an extremely simple computer code could be developed, which utilized the experimental data, in order to analyze changing trends in the downwash pattern caused by changes in the wing-winglet combination. Naturally, increasing downwash velocities indicate increases in induced drag. The changes of most experimental interest are the winglet dihedral angle and the winglet lift distribution. Obviously, the winglet lift distribution is primarily affected by planform shape, airfoil shape,

incidence angle, twist, and even dihedral angle. For the purposes of this study the winglet is assumed to have an elliptic lift distribution throughout the entire range of dihedral angles.

Development

The Biot-Savart Law, found in any good aerodynamics text,[31] is the basic tool used for this treatment. The Biot-Savart Law is developed from potential flow theory, in which the properties and motion of a theoretical vortex are treated as an irrotational flow with infinite vorticity at the center. The center point is referred to as a point vortex whose strength is defined as the circulation about that point. The Biot-Savart Law mathematically describes how this point vortex induces a velocity at points in the surrounding flowfield. Fig. A-1 illustrates the law, showing a velocity increment dV being induced at point P by an increment of the point vortex filament which stretches from $-\infty$ to $+\infty$.

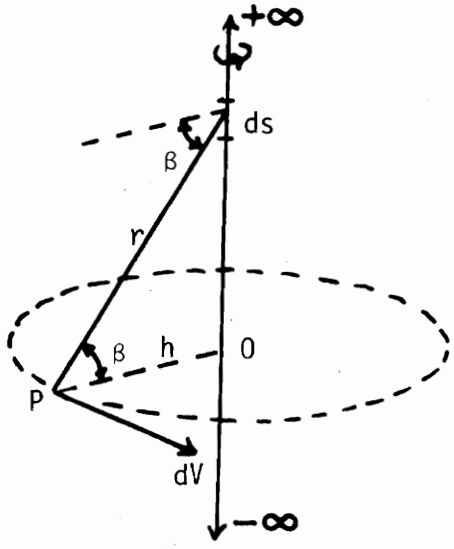

Fig. A-1. Illustration of Biot-Savart Law.

The Biot-Savart Law is written

$$dV = \frac{\Gamma}{4\pi} \frac{\cos \beta \, ds}{r^2} \tag{1}$$

or

$$V = \frac{\Gamma}{4\pi} \int_{-\infty}^{+\infty} \frac{\cos \beta \, ds}{r^2} \tag{2}$$

where Γ is the circulation strength of the vortex filament, r is the distance between the filament and the point P, and β is the angle between the length r and the normal to the filament. The induced velocity is perpendicular to the plane containing the length ds and the point P.

Prandtl's lifting line theory, based on the laws of Helmholtz and the Kutta-Joukowsky theorem, provides the structure within which the Biot-Savart Law can be used to analyze the wing downwash velocities. The wing is treated as a bound vortex which turns 90° at the wingtips and proceeds downstream, called a horseshoe vortex. However, since the lift distribution along the lifting line (bound vortex) is usually not uniform, the wing is then represented by a superposition of horseshoe vortex elements of various strengths (Fig. A-2a). From this figure we can see that a horseshoe vortex is generated at each point on the wing where a lift change occurs. Figure A-2b illustrates this same system for a continuous circulation distribution, and the resultant downwash velocity field.

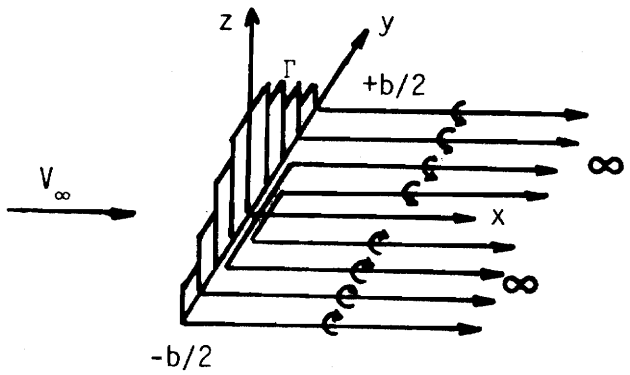

a. Horseshoe Vortex System

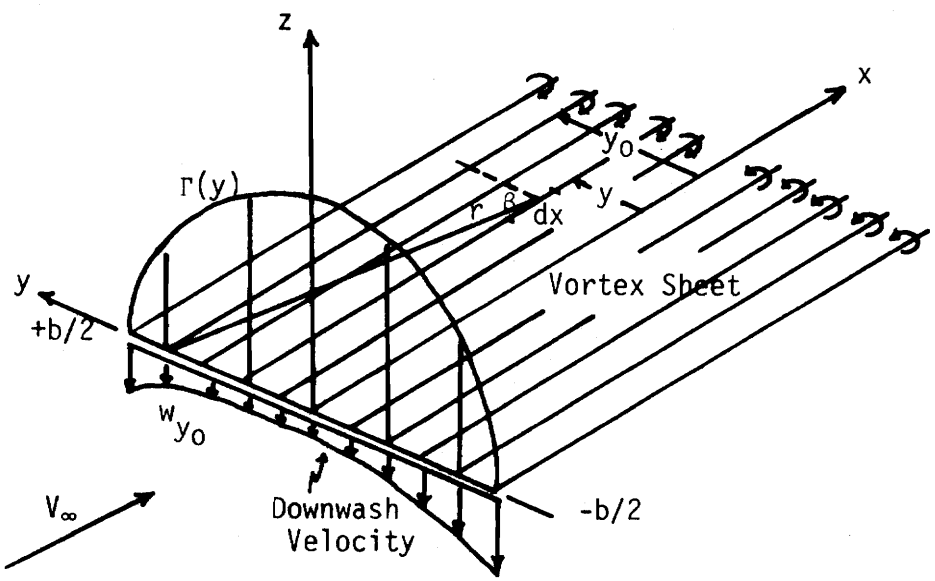

b. Downwash Due to Continuous Circulation Distribution

Fig. A-2. Induced Downwash.

Using the Biot-Savart Law in conjunction with Fig. A-3 and the coordinate system shown in Fig. A-2b, we can develop the expression for downwash velocity along the wing span.

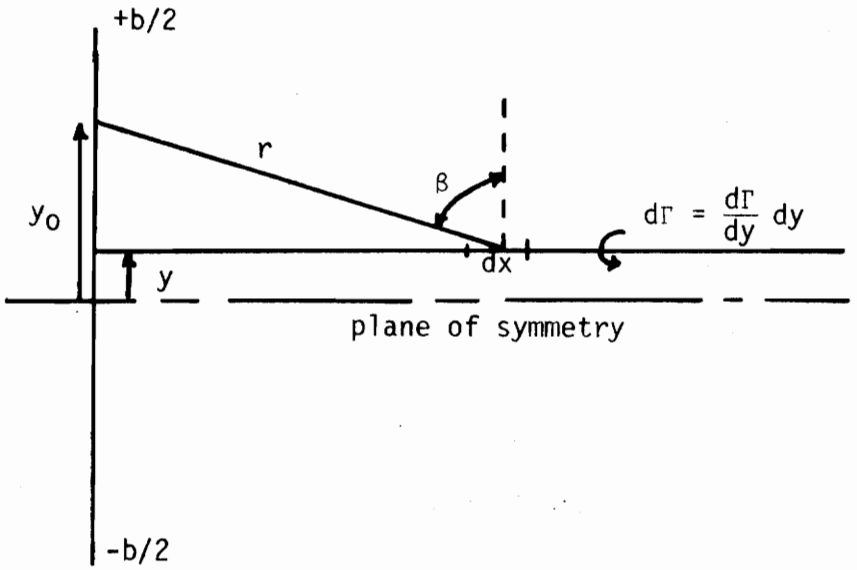

Fig. A-3. Induced Velocity at Point y_o.

$$d\, w_{y_o} = \frac{d\Gamma}{4\pi} \int_0^{\infty} \frac{\cos \beta \, dx}{r^2}$$

since we're only interested in the downwash due to the downstream effects. Using the trigonometric relationships

$$r = (y_o - y) \sec \beta$$

$$x = s = (y_o - y) \tan \beta$$

$$dx = ds = (y_o - y) \sec^2 \beta \, d\beta$$

we can evaluate the integral

$$\int_0^{\infty} \frac{\cos \beta \, dx}{r^2} = \int_0^{\infty} \frac{\cos \beta \, (y_o - y) \sec^2 \beta \, d\beta}{(y_o - y)^2 \sec^2 \beta}$$

evaluating the limits using $x = (y_o - y) \tan \beta$ transforms the limits to $0 \leq \beta \leq \frac{\pi}{2}$. Therefore the integral becomes

$$\frac{1}{(y_o - y)} \int_0^{\frac{\pi}{2}} \cos \beta \, d\beta = \frac{1}{(y_o - y)}$$

Since $d\Gamma = \frac{d\Gamma}{dy} dy$ we can write the downwash velocity as

$$w_{y_o} = - \frac{1}{4\pi} \int_{-b/2}^{+b/2} \frac{d\Gamma/dy}{(y_o - y)} dy \qquad (3)$$

The minus sign accounts for the fact that downwash is considered positive in the downward direction. The downwash velocity equation (3) can readily be used with an experimental pressure distribution and numerical integration techniques to determine the spanwise downwash distribution. The only input data required is the slope of the lift distribution curve at various points along the span. This is done for the experimental lift distributions of both the wing with square tips and the wing with attached winglets. The results are shown in Figure A-8, and discussed later in this appendix.

In order to determine the effect of the winglet dihedral angle on the wing downwash distribution it was necessary to develop an expression for the downwash on the main wing due to the lift distribution on the winglet itself. Fig. A-4 illustrates the basic

Biot-Savart conceptual approach.

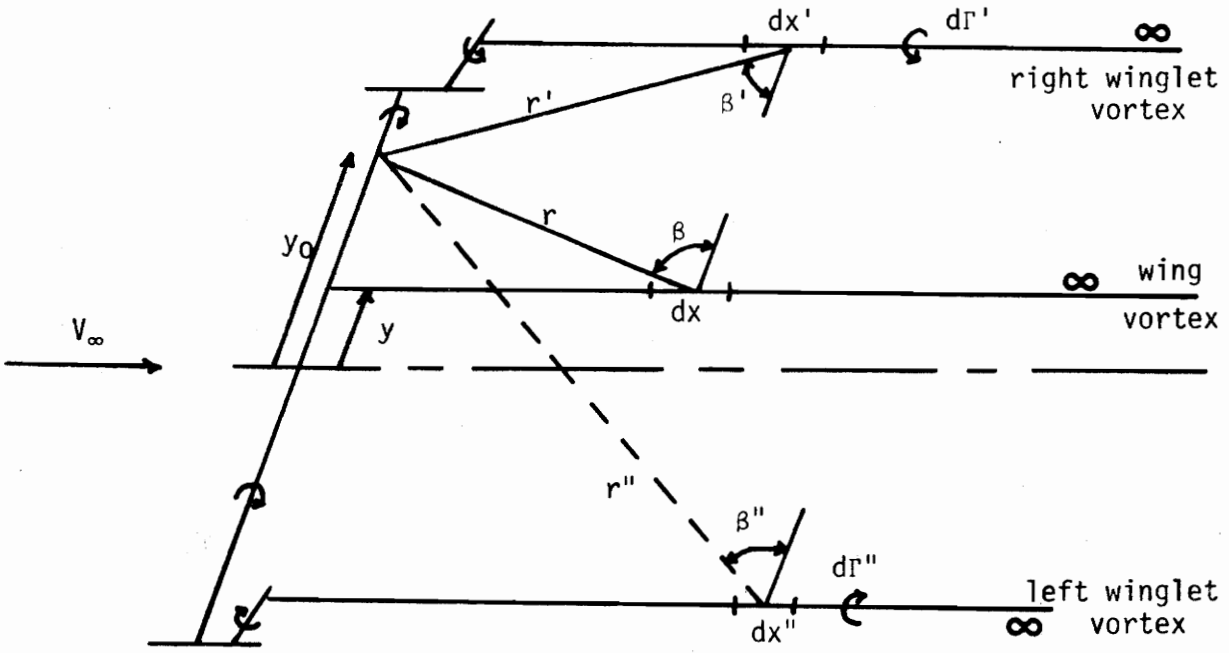

Fig. A-4. Induced Velocity at y_o Due to Wing and Winglets.

The following development will apply for the effects on the wing due to the right wingtip winglet. The effects of the left winglet will be the same, in mirror-fashion, and can be simply added. The following assumptions are applicable:

(1) The sweepback angle of the winglet quarter-chord provides negligible contribution.

(2) The lower winglet contribution is negligible. (This development is for an upper winglet configuration.)

(3) The total downwash on the wing is simply a superposition of the wing downwash due to wing lift plus wing downwash due to the lift of the left and right winglets.

(4) The effect of the winglet bound vortex on the wing bound vortex is negligible.

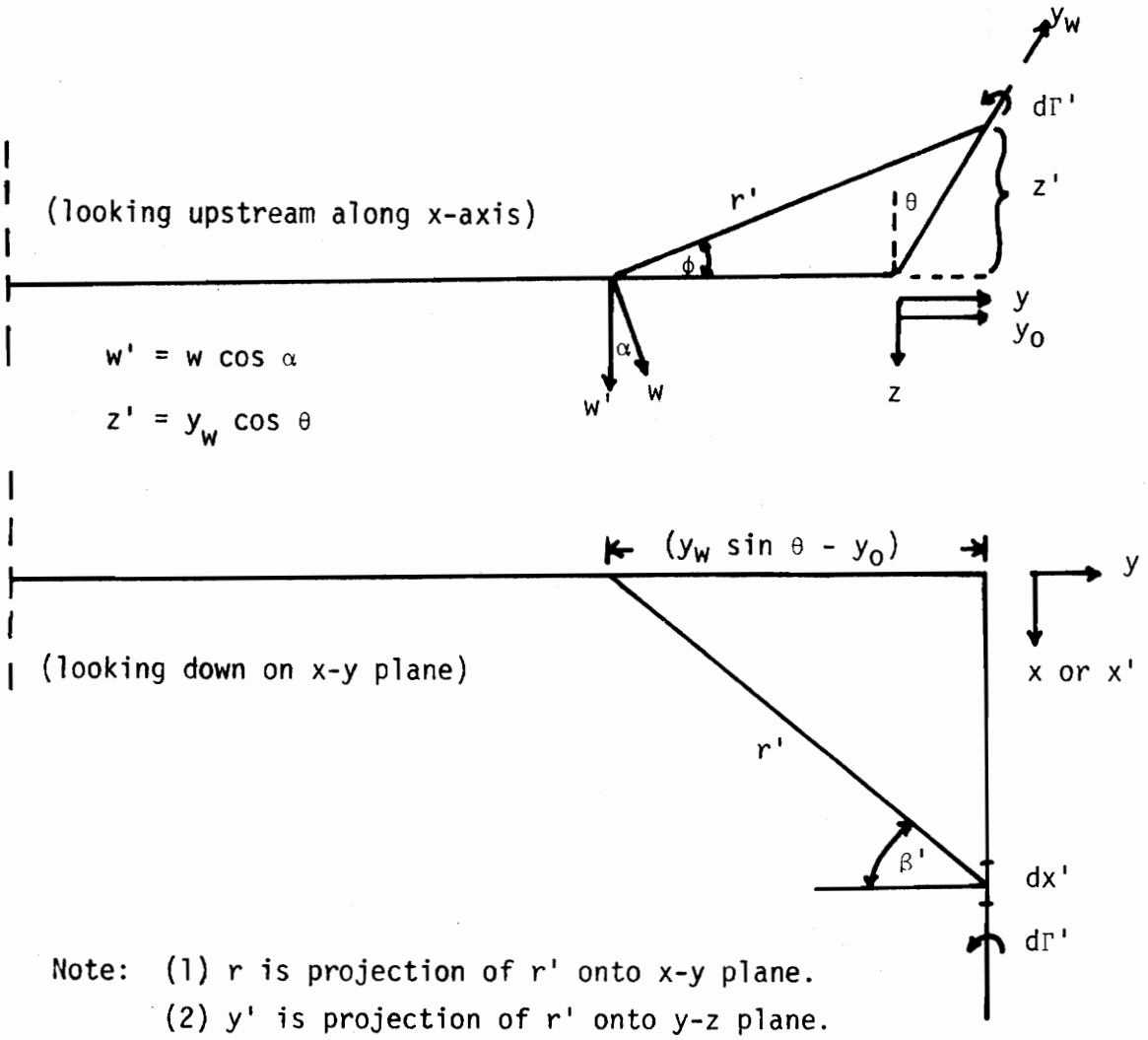

Note: (1) r is projection of r' onto x-y plane.
(2) y' is projection of r' onto y-z plane.
(3) $(y_w \sin \theta - y_o)$ is projection of y' onto x-y plane.

Fig. A-5. Downwash on Wing Due to Winglet.

$$\sec \beta' = \frac{r'}{y'} \qquad \cos \phi = \frac{(y_w \sin \theta - y_o)}{y'} \tag{4}$$

$$\therefore\ r' = \frac{(y_w \sin \theta - y_o)}{\cos \phi} \sec \beta'$$

$$\tan \phi = \frac{z'}{(y_w \sin \theta - y_o)} \Rightarrow \tan^2 \phi = \frac{z'^2}{(y_w \sin \theta - y_o)^2}$$

and

$$\tan^2 \phi = \sec^2 \phi - 1 = \frac{1}{\cos^2 \phi} - 1$$

$$\therefore\ \frac{1}{\cos^2 \phi} = \frac{z'^2}{(y_w \sin \theta - y_o)^2} + 1 \tag{5}$$

$$r'^2 = \frac{(y_w \sin \theta - y_o)^2}{\cos^2 \phi} \sec^2 \beta'$$

finally

$$r'^2 = \sec^2 \beta'[(y_w \sin \theta - y_o)^2 + z'^2]$$

or

$$r'^2 = \sec^2 \beta'[(y_w \sin \theta - y_o)^2 + (y_w \cos \theta)^2] \tag{6}$$

Now

$$\tan \beta' = \frac{x'}{y'} \Rightarrow x' = \frac{(y_w \sin \theta - y_o)}{\cos \phi} \tan \beta'$$

squaring this expression for x' and substituting (5) yields

$$x'^2 = \tan^2 \beta'[(y_w \sin \theta - y_o)^2 + (y_w \cos \theta)^2] \tag{7}$$

taking the square root and differentiating gives the expression for dx'

$$dx' = \sec^2 \beta' [(y_w \sin \theta - y_o)^2 + (y_w \cos \theta)^2]^{1/2} \, d\beta' \tag{8}$$

Using the trigonometric and geometric interpretations of Fig. A-5, we can continue the development

$$dw = - \frac{d\Gamma}{4\pi} \int_0^{\infty} \frac{\cos \beta' \, dx'}{r'^2} \tag{9}$$

making substitutions of (6) and (8) into (9) gives

$$dw = - \frac{d\Gamma}{4\pi} \int_0^{\pi/2} \frac{\cos \beta' \, d\beta'}{[(y_w \sin \quad - y_o)^2 + (y_w \cos \quad)^2]^{1/2}} \tag{10}$$

but we want w' and w' = w cos α

$$\therefore \; dw' \sim \int_0^{\pi/2} \frac{\cos \alpha \cos \beta' \, d\beta'}{r'^2} \tag{11}$$

$$\cos \alpha = \frac{r}{r'} \tag{12}$$

$$r^2 = x'^2 + (y_w \sin \theta - y_o)^2 \tag{13}$$

$$\therefore \cos \alpha = \frac{\{\tan^2 \beta' [(y_w \sin \theta - y_o)^2 + (y_w \cos \theta)^2] + (y_w \sin \theta - y_o)^2\}^{1/2}}{\sec \beta' [(y_w \sin \theta - y_o)^2 + (y_w \cos \theta)^2]^{1/2}} \tag{14}$$

(10) now becomes

$$dw = \frac{-d\Gamma}{4\pi} \int_0^{\pi/2} \cdot \frac{\cos^2\beta' \{\tan^2\beta' [(y_w \sin\theta - y_o)^2 + (y_w \cos\theta)^2] + (y_w \sin\theta - y_o)^2\}^{1/2} d\beta'}{[(y_w \sin\theta - y_o)^2 + (y_w \cos\theta)^2]} \tag{15}$$

but $d\Gamma = \frac{d\Gamma}{dy_w} dy_w$, and we will assume an elliptic lift distribution[32] where

$$\Gamma = \Gamma_s \sqrt{1 - \left(\frac{y}{b/2}\right)^2} \tag{16}$$

and, according to Spreiter and Sacks[14]

$$\Gamma_s = \frac{1}{2} V_\infty C C_\ell \tag{17}$$

where

C_ℓ = winglet section lift coefficient at root

C = winglet root chord length

$$\frac{d\Gamma}{dy_w} = \frac{-\Gamma_s y_w}{\left(\frac{b_w}{2}\right)\left[\left(\frac{b_w}{2}\right)^2 - y_w^2\right]^{1/2}}$$

therefore

$$w'_{y_o} = -\frac{1}{4\pi}\int_{y_{w_1}}^{y_{w_2}}\left(-\frac{V_\infty\, C\, C_\ell}{b_w}\right)\left(\frac{y_w\, dy_w}{\left[\left(\frac{b_w}{2}\right)^2 - y_w^2\right]^{1/2}}\right)$$

$$\int_0^{\pi/2}\frac{\cos^2\beta'\{\tan^2\beta'[(y_w\sin\theta - y_o)^2 + (y_w\cos\theta)^2] + (y_w\sin\theta - y_o)^2\}^{1/2}d\beta'}{[(y_w\sin\theta - y_o)^2 + (y_w\cos\theta)^2]} \qquad (18)$$

Fig. A-6 illustrates the load distribution for this development

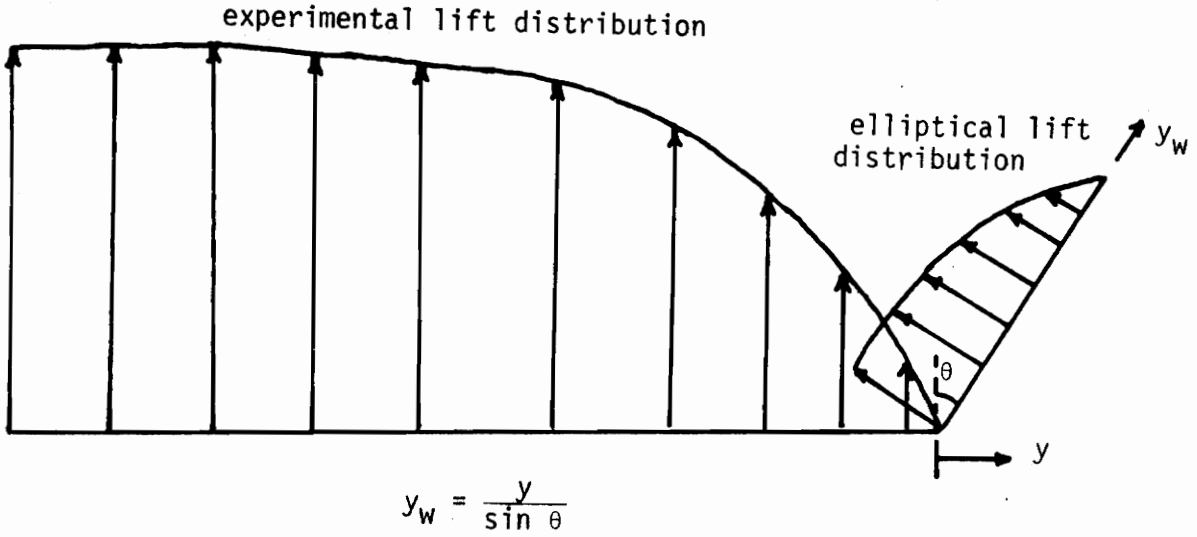

Fig. A-6. Wing/Winglet Lift Distribution.

placing everything together leads to

$$w'_{y_o} = \frac{V_\infty \, C \, C_\ell}{4\pi b_w \sin^2\theta} \int_0^{y_w} \frac{y \, dy}{\left[(y-y_o)^2 + (yctn\theta)^2\right]\left[\left(\frac{b_w}{2}\right)^2 - \frac{y^2}{\sin^2\theta}\right]^{1/2}}$$

$$\int_0^{\pi/2} \cos^2\beta' \left\{ \tan^2\beta' \left[(y-y_o)^2 + (yctn\theta)^2\right] + (y-y_o)^2 \right\}^{1/2} d\beta' \qquad (19)$$

letting $A = (y-y_o)^2$ and $K = (yctn\theta)^2$ simplifies this expression to

$$w'_{y_o} = \frac{V_\infty \, C \, C_\ell}{4\pi b_w \sin^2\theta} \int_0^{y_w} \frac{y \, dy}{(A+K)\left[\left(\frac{b_w}{2}\right)^2 - \frac{y^2}{\sin^2\theta}\right]^{1/2}}$$

$$\int_0^{\pi/2} \cos^2\beta' \left[\tan^2\beta'(A+K) + A\right]^{1/2} d\beta' \qquad (20)$$

we can solve the second integral exactly by the following substitutions

$$\tan^2\beta' = \sec^2\beta' - 1$$

$$\therefore \int_0^{\pi/2} \cos^2\beta' \left[\tan^2\beta'(A+K)+A\right]^{1/2} d\beta' = \int_0^{\pi/2} \cos^2\beta' \left[(A+K)\sec^2\beta' - K\right]^{1/2} d\beta' \qquad (21)$$

Since $\sec^2\beta' = \frac{1}{\cos^2\beta'}$, then this integral becomes

$$\int_0^{\pi/2} \cos \beta' [A + K \sin^2 \beta']^{1/2} \, d\beta' \tag{22}$$

now let $x = \sin \beta'$

$\therefore dx = \cos \beta' \, d\beta'$

placing these into (21) gives

$$\int_0^1 [A + Kx^2]^{1/2} \, dx \tag{23}$$

The above integral can be solved exactly using an integral table. The solution is

$$\frac{K^{1/2}}{2} \left\{ \left[\frac{A}{K} + 1\right]^{1/2} + \frac{A}{K} \ell n \left[1 + \left(\frac{A}{K} + 1\right)^{1/2}\right] - \frac{A}{K} \ell n \left[\frac{A}{K}\right]^{1/2} \right\} \tag{24}$$

placing this back into equation (19) and using the following expressions

$$D = \frac{V_\infty \, C \, C_\ell}{4\pi b_w \sin^2 \theta} \tag{25}$$

$$C = \left[\left(\frac{b_w}{2}\right)^2 - \left(\frac{y^2}{\sin^2 \theta}\right)\right]^{1/2} \tag{26}$$

we arrive at the final expression for the downwash on the wing due to an elliptical lift distribution on a winglet

$$w'_{y_o} = D \int_0^{y_w} \frac{K^{1/2} y \left\{ \left[\frac{A}{K} + 1 \right]^{1/2} + \frac{A}{K} \ell n \left[1 + \left(\frac{A}{K} + 1 \right)^{1/2} \right] - \frac{A}{K} \ell n \left[\frac{A}{K} \right]^{1/2} \right\} dy}{C(A + K)} \tag{27}$$

where

$$A = [y - y_o]^2$$

$$B = (y \text{ ctn } \theta)^2$$

Equation (27) can now be readily integrated numerically using coordinates y and y_o and dihedral angles θ.

Computer Results

Figure A-7 is the computer code used to determine the downwash on the wing due to an experimentally obtained lift distribution. The only input required is the slope of the lift curve (or circulation curve) at various points across the wing. Figure A-8 shows the results for the wing with square tips and the wing with attached winglets. The results are as expected. The higher loading at the tips caused by the winglets produces a very rapid increase in downwash in this very small region. There appears to be about an 80% increase in downwash over the entire wing with attached winglets. However, with such small downwash magnitudes compared to a freestream velocity of 100fps, the resultant change in induced drag is small indeed, a fact verified by the experiments.

Figure A-9 is the simple computer program developed to determine the effect that different dihedral angles would have on the downwash distribution over the wing due to an elliptical lift distribution on the right winglet. This particular example is set up for a 15° dihedral angle and gives results in the form of a normalized downwash equal to $4\pi b_w w/V_\infty CC_\ell$. These results have been plotted in Figure A-10 for this normalized downwash.

Of interest is the rather large increase in downwash between dihedral angles of 15° and 20°. It appears that significant induced drag increases will occur for dihedral angles greater than 15°. Also of note is the reduction of downwash near the wingtip for dihedral angles up to about 30°-35°. Dihedral angles greater than that produce continuously increasing downwash from the left wingtip to the right wingtip.

There also appears to be a definite break in the downwash pattern at $\theta = 60°$. At that dihedral angle the downwash pattern has the largest magnitude across the entire span. At $\theta = 61°$ the downwash immediately reduces to values similar to the smaller dihedral angles, but with a different tip pattern. ($\theta = 65°$ is plotted in Fig. A-10.) It is conjectured that this break is indicative of the point at which the wing-winglet combination no longer produces two distinct vortices, but rather acts simply as a wing with a bent tip which sheds only one vortex. The 65° dihedral angle plot indicates that a simple wingtip extension is not as effective as a canted winglet in reducing the induced drag.

The last figure (Fig. A-11) illustrates an attempt to superpose the winglet results with those of the experimental square tip in order to obtain the experimental winglet results. Using the normal component of the winglet side force coefficient, which is the winglet lift coefficient, it is apparent that the effect of the winglet on the wing is underestimated to a large extent. Therefore another attempt merely forced a curve fit for the downwash at the wing root. From this attempt it becomes apparent either that the winglet model does a poor job of estimating the downwash at the wingtip or that an elliptical lift distribution is not the best guess for the winglet. From the experimental results of Whitcomb it seems that the latter conjecture holds more promise. The winglet gives its best results when the winglet root is highly loaded and the lift distribution is quite non-elliptical. Another source of error is the measurement of the slope of the lift distribution curve for the experimental results of the wing-winglet configuration, particularly in the region of the wingtip.

Recommendations

An experimental study to correlate the effects of the winglet dihedral angle on the wing downwash pattern should be undertaken. This study should also look at the vortex pattern for each different dihedral angle. Lastly, the winglet should be fitted with spanwise pressure taps to determine its exact lift distribution.

```
      DIMENSION YB(41),CIRCL(41),DGAMMA(41),DWASH(41)
      I=0
   10 CONTINUE
      I=I+1
      READ(5,500,END=999)YB(I),CIRCL(I)
      GO TO 10
  999 M=I-1
      WRITE(6,600)
      WRITE(6,601)(YB(I),CIRCL(I),I=1,M)
      DO 30 K=1,40
      CONST=-1.625+(K-1)*0.0834
      DO 100 I=1,M
  100 DGAMMA(I)=CIRCL(I)/(CONST-YB(I))
      I=I-1
      WRITE(6,700)CONST
      WRITE(6,701)(DGAMMA(N),N=1,I)
      CALL QTFG(YB,DGAMMA,DWASH,41)
      DWASH(41)=DWASH(41)/(4.0*3.1416)
      WRITE(6,800)DWASH(41)
   30 CONTINUE
      STOP
  500 FORMAT(2F10.4)
  600 FORMAT(3X,6(5X,'YB',5X,'CIRCL'))
  601 FORMAT(4X,6(2X,F7.4,2X,F7.3))
  700 FORMAT(/10X,'CONST=',F7.4)
  701 FORMAT(13X,'DGAMMA=',10F10.5/,4(20X,10F10.5/))
  800 FORMAT(13X,'DWASH=',F20.5)
      END

      SUBROUTINE QTFG(X,Y,Z,NDIM)
      DIMENSION X(1),Y(1),Z(1)
      SUM2=0
      IF(NDIM-1)4,3,1
C     INTEGRATION LOOP
    1 DO 2 I=2,NDIM
      SUM1=SUM2
      SUM2=SUM2+.5*(X(I)-X(I-1))*(Y(I)+Y(I-1))
    2 Z(I-1)=SUM1
    3 Z(NDIM)=SUM2
    4 RETURN
      END
```

Documentation

1. YB is y coordinate along wing span (an input).

2. CIRCL is $d\Gamma/dy$ (experimental) at each y position (an input).

3. CONST is y_0 coordinate along wing span.

4. DWASH is w_{y_0}.

Fig. A-7. Computer Code for Use with Experimental Lift Distribution.

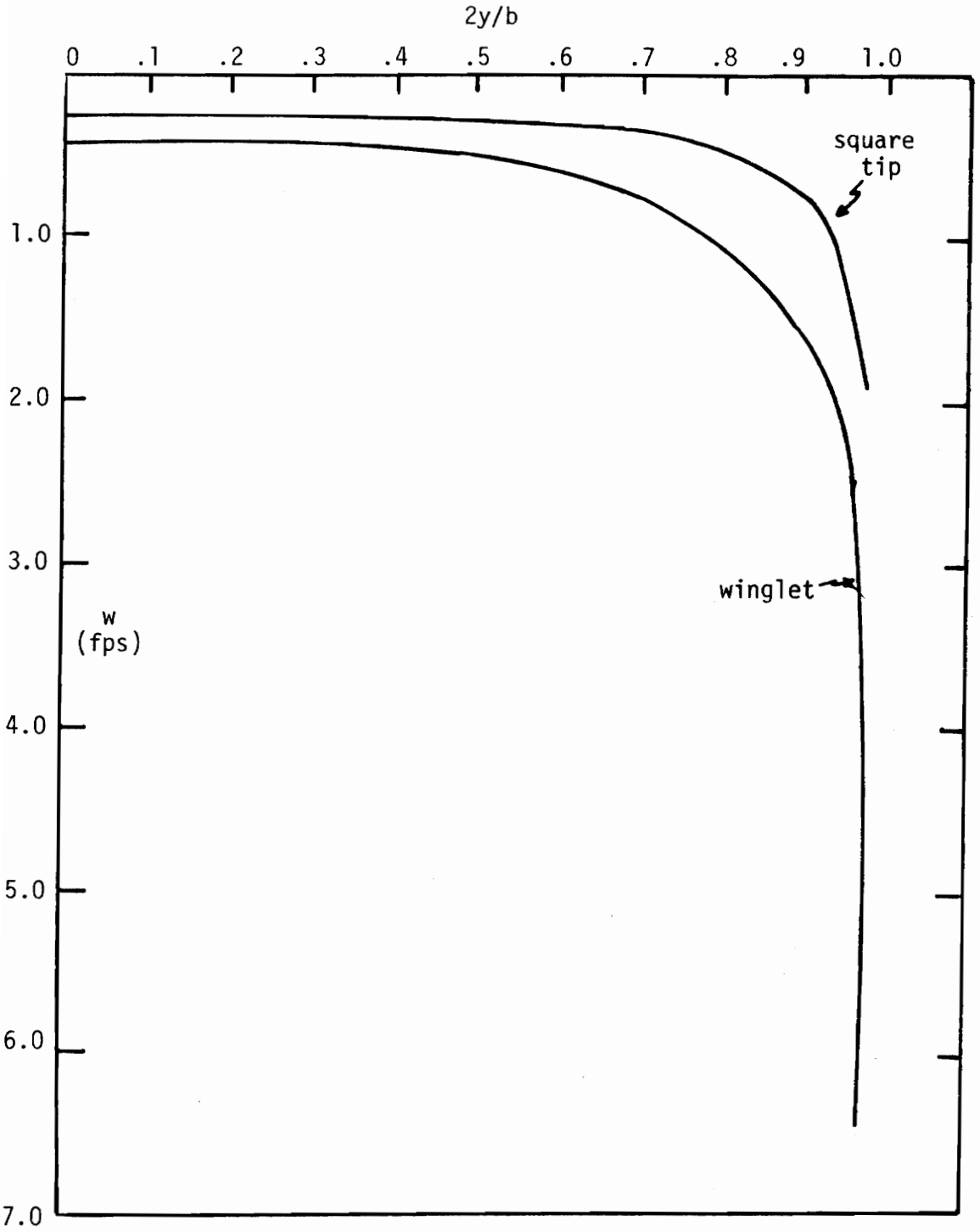

Fig. A-8. Downwash Distribution.

```
//WATFIV
      DIMENSION YB(41),B(41),C(41),A(41),FN(41),DWASH(41)
      I=0
   10 CONTINUE
      I=I+1
      READ(5,500,END=999)YB(I)
      B(I)=13.9282*(YB(I))**2
      C(I)=SQRT(0.4444-(14.9282*(YB(I))**2))
      GO TO 10
  999 M=I-1
      WRITE(6,600)
      WRITE(6,601)(YB(I),B(I),C(I),I=1,M)
      DO 30 K=1,40
      CONST=-0.0391-(K-1)*0.0834
      DO 100 I=1,M
  100 A(I)=(YB(I)-CONST)**2
      DO 200 I=1,M
  200 FN(I)=YB(I)*SQRT(B(I))*(SQRT(A(I)/B(I)+1)+A(I)/B(I)*ALOG(1+SQRT
     1(A(I)/B(I)+1))-A(I)/B(I)*ALOG(SQRT(A(I)/B(I))))/((A(I)+B(I))*C(I))
      I=I-1
      WRITE(6,700)CONST
      WRITE(6,701)(FN(N),N=1,I)
      CALL WIFG(YB,FN,DWASH,41)
      DWASH(41)=DWASH(41)/.066987
      WRITE(6,800)DWASH(41)
   30 CONTINUE
      STOP
  500 FORMAT(F10.5)
  600 FORMAT(2X,'YB',4(8X,'B',8X,'C',7X,'YB'))
  601 FORMAT(4(F7.5,2X,F7.5,2X,F7.5,2X))
  700 FORMAT(/10X,'CONST=',F7.4)
  701 FORMAT(13X,'FN=',10F10.5/,4(20X,10F10.5/))
  800 FORMAT(13X,'DWASH=',F20.5)
      END
```

Note: Subroutine is same as in Fig. A-7.

Fig. A-9. Computer Code to Determine Winglet Effect at θ = 15°.

Documentation

1. YB is y coordinate along wing span (an input).
2. $B = (y \text{ ctn } \theta)^2$.
3. $C = \left[\left(\frac{b_w}{2}\right)^2 - \left(\frac{y^2}{\sin^2\theta}\right)\right]^{1/2}$.
4. $A = [y - y_o]^2$.
5. CONST is y_o coordinate along wing span.
6. DWASH is $\frac{4\pi b_w \, w_{y_o} \, (\sin^2\theta)}{V_\infty \, C \, C_\ell}$.

Fig. A-9. (continued).

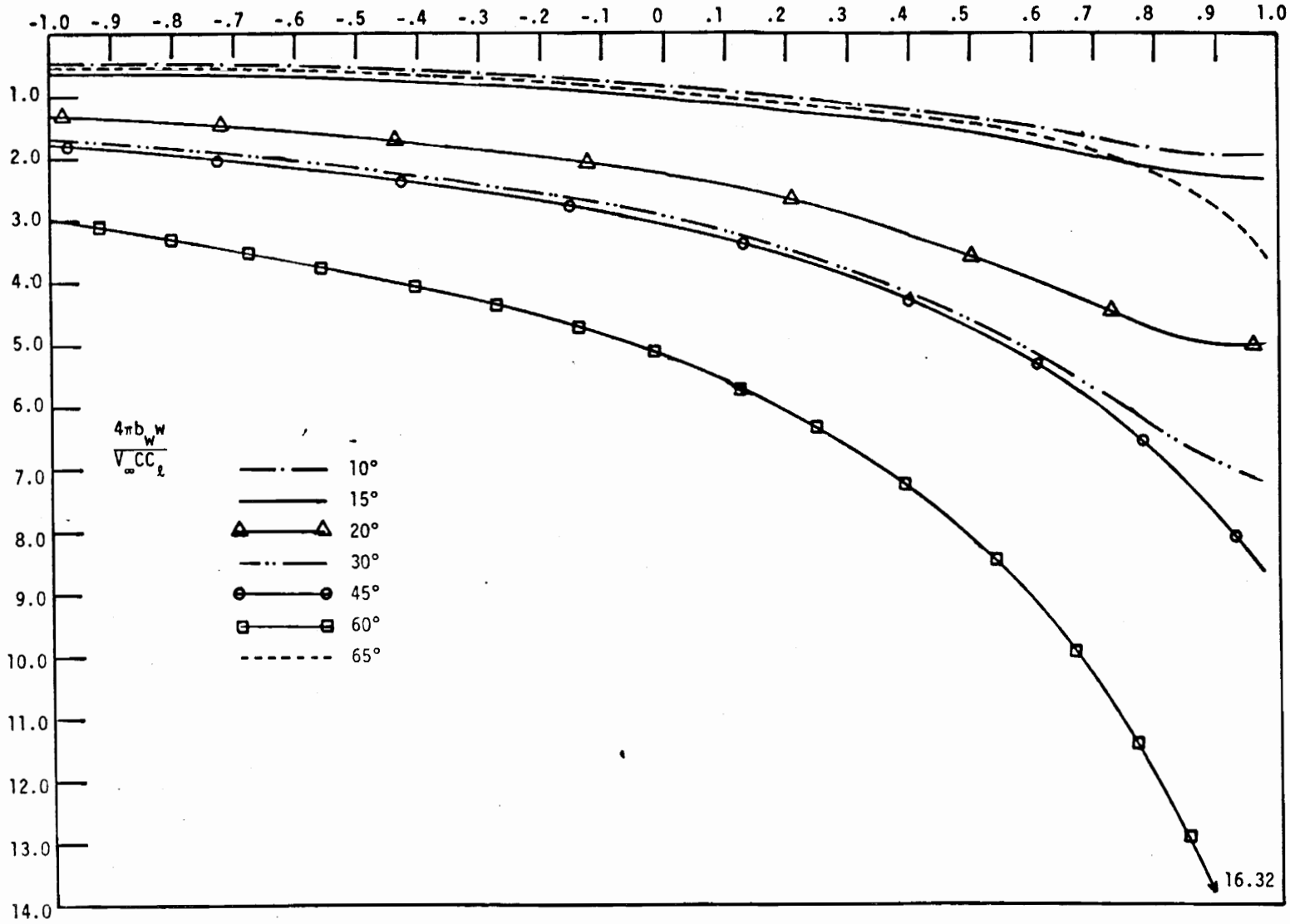

Fig. A-10. Effects of Winglet Dihedral on Downwash.

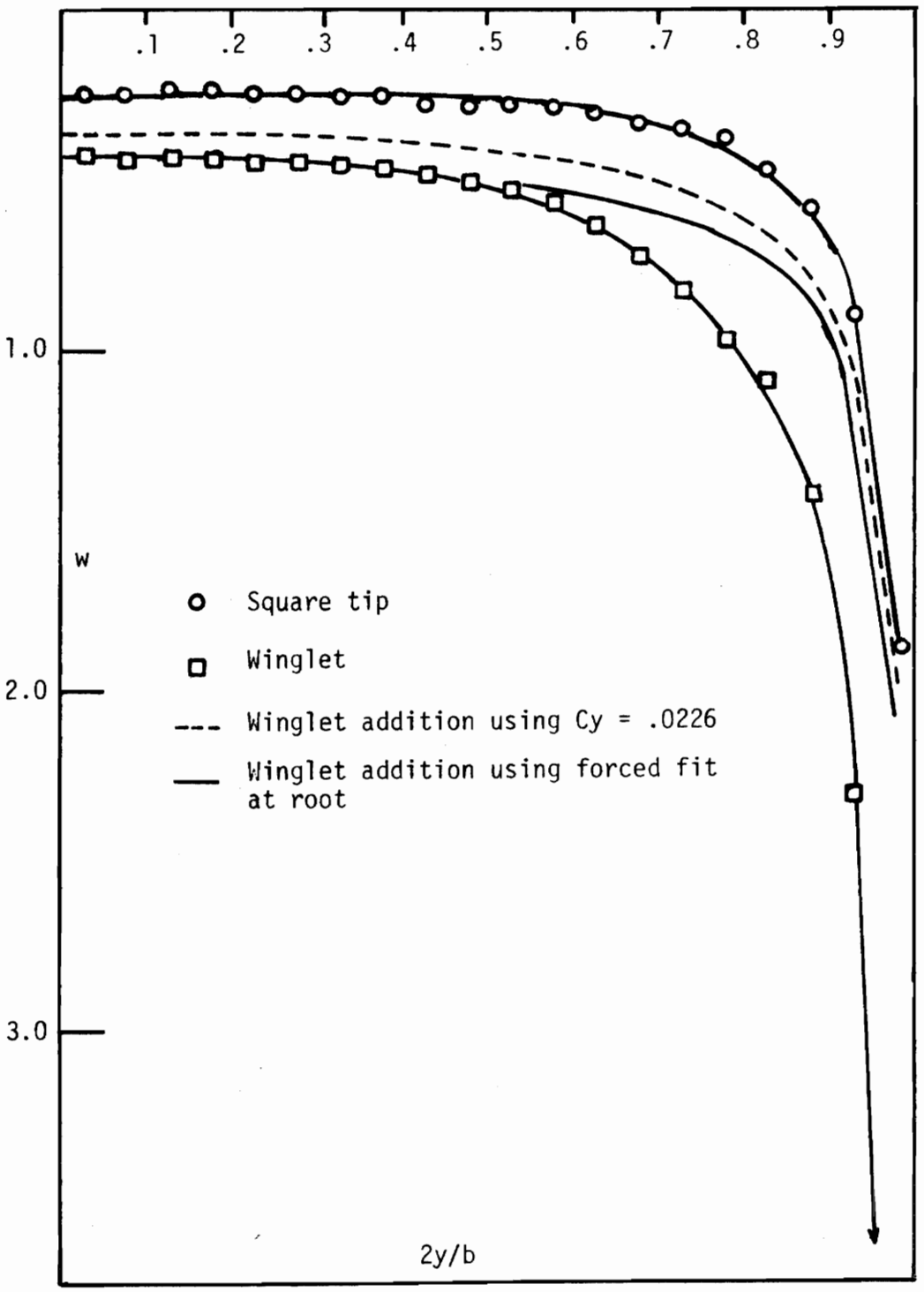

Fig. A-11. Superposition of Winglet Downwash on Square Tip Downwash.

APPENDIX B

TABULATED EXPERIMENTAL DATA

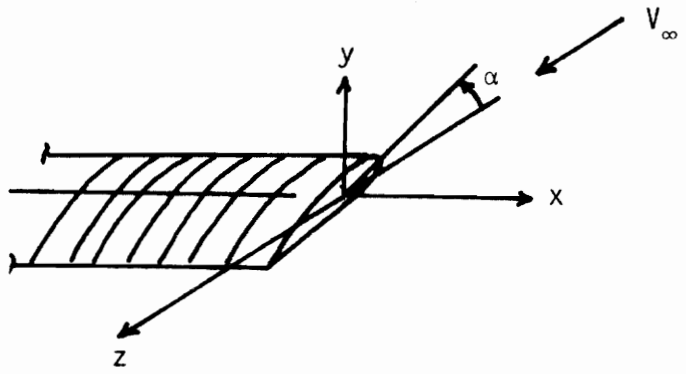

a. Sign Convention

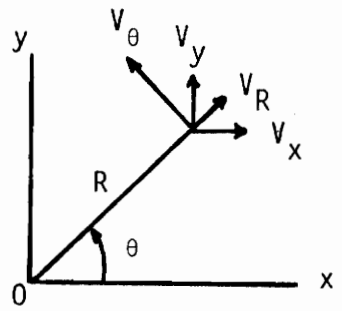

b. Relation Between x, y and R, θ

Fig. B-1. Coordinate System.

TABLE B-1

SQUARE TIP

INBOARD PROFILES FOR Z/C = 5, V_∞ = 103.457 ft/sec

R (ft)	V_z (fps)	V_r (fps)	V_θ (fps)
0.0	93.526	-2.164	- 0.525
0.002	95.906	-2.896	-10.750
0.005	98.001	-3.372	-19.474
0.007	100.332	-4.034	-27.855
0.010	103.918	-4.252	-35.269
0.012	105.774	-4.652	-45.796
0.019	111.262	-4.308	-50.861
0.022	116.691	-4.358	-56.445
0.026	118.625	-4.379	-58.383
0.030	118.294	-4.539	-57.540
0.034	114.037	-4.677	-52.999
0.038	110.182	-4.296	-47.972
0.042	107.675	-3.713	-43.711
0.051	104.135	-2.474	-36.329
0.059	101.764	-1.374	-30.875
0.067	100.955	-0.907	-27.337
0.093	99.575	-0.808	-20.164
0.134	99.430	-0.555	-15.002
0.218	99.313	-0.309	- 9.668
0.301	99.214	-0.298	- 7.301
0.384	99.006	-0.507	- 6.082
0.468	98.918	-0.722	- 5.115

Note: Data for all tables is for Q = 2.2 in. water and $\alpha = 6°$.

TABLE B-2

SQUARE TIP

OUTBOARD PROFILES FOR Z/C = 5, V_∞ = 103.342 ft/sec

R (ft)	V_z (fps)	V_r (fps)	V_θ (fps)
0.0	93.723	-2.167	0.0
0.002	95.163	-2.206	11.560
0.005	96.344	-1.147	20.588
0.007	97.174	-0.603	30.582
0.010	97.724	0.150	36.295
0.013	96.893	0.961	39.795
0.016	95.183	1.179	43.269
0.019	93.987	1.154	46.858
0.023	93.200	1.342	49.192
0.026	93.008	1.541	49.798
0.030	93.885	1.713	49.421
0.034	95.046	2.106	47.754
0.038	96.186	1.907	45.202
0.043	96.610	1.519	43.304
0.051	97.919	0.734	38.152
0.059	98.060	-0.876	33.374
0.067	97.865	-1.047	29.892
0.093	99.127	-1.677	23.794
0.134	98.771	-2.069	17.025
0.218	98.786	-1.839	13.230
0.301	98.559	-2.045	10.172
0.384	98.200	-2.035	8.719
0.468	97.691	-1.800	7.517

TABLE B-3

SQUARE TIP

INBOARD PROFILES FOR Z/C = 20, V_∞ = 102.929 ft/sec

R (ft)	V_z (fps)	V_r (fps)	V_θ (fps)
0.0	91.857	-1.896	0.0
0.002	92.839	-2.154	- 6.858
0.005	93.276	-2.635	-14.090
0.007	94.453	-2.439	-19.442
0.010	95.479	-2.916	-25.987
0.012	96.240	-2.716	-27.960
0.016	100.300	-3.619	-35.900
0.019	102.577	-3.647	-39.882
0.022	106.025	-3.690	-44.662
0.026	107.299	-4.258	-44.452
0.030	111.622	-4.290	-49.625
0.034	111.642	-4.643	-48.894
0.038	109.257	-4.268	-45.016
0.042	107.756	-3.880	-41.480
0.051	104.120	-2.855	-34.370
0.059	102.015	-1.988	-29.468
0.067	101.747	-1.555	-26.649
0.093	101.008	-1.078	-20.315
0.134	100.228	-1.028	-15.431
0.218	99.784	-1.427	-11.332
0.301	100.474	-1.226	- 9.196
0.384	100.281	-1.646	- 7.557
0.468	100.232	-1.428	- 6.621

TABLE B-4

SQUARE TIP

OUTBOARD PROFILES FOR Z/C = 20, V_∞ = 102.862 ft/sec

R (ft)	V_z (fps)	V_r (fps)	V_θ (fps)
0.0	92.037	-2.134	0.0
0.002	92.091	-1.906	6.522
0.005	92.805	-1.241	12.441
0.007	93.046	-0.594	18.831
0.010	93.527	-1.544	23.650
0.012	93.099	-1.564	28.227
0.016	94.435	-1.632	32.879
0.019	94.443	-0.810	36.527
0.022	94.930	-0.447	39.826
0.026	95.275	-0.268	41.071
0.030	96.053	0.500	42.750
0.034	97.821	0.641	42.073
0.038	98.483	1.031	41.251
0.042	99.662	0.416	38.812
0.051	100.132	-0.351	34.463
0.059	99.961	-1.113	29.200
0.067	100.389	-1.727	26.365
0.093	101.027	-1.918	20.289
0.134	100.934	-2.107	15.302
0.218	100.953	-1.884	10.977
0.301	99.639	-1.635	9.396
0.384	99.513	-1.196	8.133
0.468	99.301	-1.188	7.014

TABLE B-5

POINTED TIP

INBOARD PROFILES FOR Z/C = 5, V_∞ = 102.570 ft/sec

R (ft)	V_z (fps)	V_r (fps)	V_θ (fps)
0.0	75.887	-1.566	0.316
0.002	79.838	-2.464	-11.112
0.005	84.917	-3.524	-20.304
0.007	91.630	-4.442	-28.411
0.010	97.972	-5.246	-33.802
0.012	102.342	-5.797	-36.782
0.016	105.814	-5.373	-38.936
0.019	106.198	-4.993	-37.980
0.023	106.106	-4.039	-37.021
0.026	105.233	-2.680	-35.571
0.030	103.533	-2.048	-33.335
0.034	102.394	-1.614	-32.029
0.038	101.789	-1.389	-30.963
0.042	101.293	-1.365	-29.728
0.051	101.033	-0.934	-27.845
0.059	100.046	-0.678	-25.813
0.067	99.561	-0.643	-23.601
0.093	98.591	-0.573	-18.649
0.134	98.604	-0.336	-14.912
0.218	98.457	-0.523	- 9.563
0.301	98.462	-0.298	- 6.971
0.384	98.251	-0.505	- 5.767
0.468	98.202	-0.721	- 5.295

TABLE B-6

POINTED TIP

OUTBOARD PROFILES FOR Z/C = 5, V_∞ = 102.455 ft/sec

R (ft)	V_z (fps)	V_r (fps)	V_θ (fps)
0.0	75.898	-1.849	0.635
0.002	77.938	-1.626	11.377
0.005	80.716	-0.698	21.563
0.007	86.548	1.163	29.270
0.010	91.145	1.948	34.406
0.013	94.735	2.530	37.197
0.016	97.515	2.736	38.627
0.019	99.095	2.437	38.617
0.023	99.504	2.022	38.127
0.026	99.527	1.236	37.101
0.030	99.012	0.482	35.152
0.034	98.661	-0.310	34.290
0.038	98.329	-0.904	33.201
0.043	97.839	-1.291	31.894
0.051	97.632	-1.481	30.268
0.059	97.767	-1.677	27.890
0.067	98.320	-1.677	25.909
0.093	98.712	-2.086	21.632
0.134	97.883	-2.047	15.809
0.218	98.176	-1.830	13.569
0.301	97.874	-1.814	10.561
0.384	97.162	-1.574	8.627
0.468	96.645	-1.559	7.419

TABLE B-7

POINTED TIP

INBOARD PROFILES FOR Z/C = 20, V_∞ = 104.415 ft/sec

R (ft)	V_z (fps)	V_r (fps)	V_θ (fps)
0.0	90.867	-2.120	0.275
0.002	91.631	-1.897	- 6.858
0.005	93.266	-3.121	-12.844
0.007	95.409	-3.832	-18.942
0.010	97.778	-4.723	-23.359
0.012	99.561	-4.066	-27.405
0.016	101.782	-3.655	-29.496
0.019	103.291	-3.257	-31.268
0.023	104.479	-2.866	-32.181
0.026	104.183	-3.473	-31.634
0.030	103.176	-2.635	-30.619
0.034	102.563	-2.204	-29.723
0.038	102.961	-2.210	-29.347
0.042	102.922	-2.000	-29.037
0.051	103.139	-1.371	-27.558
0.059	102.288	-1.120	-25.287
0.067	101.775	-1.091	-23.279
0.093	101.514	-1.055	-18.856
0.134	100.970	-0.802	-15.375
0.218	100.567	-0.773	-11.657
0.301	101.025	-1.218	- 9.500
0.384	101.272	-1.439	- 7.300
0.468	101.365	-1.659	- 6.589

TABLE B-8

POINTED TIP

OUTBOARD PROFILES FOR Z/C = 20, V_∞ = 104.653 ft/sec

R (ft)	V_z (fps)	V_r (fps)	V_θ (fps)
0.0	91.109	-2.125	- 0.276
0.002	90.665	-1.138	5.167
0.005	93.464	-1.007	13.800
0.007	94.723	-1.064	17.764
0.010	96.148	-0.001	21.896
0.012	97.799	0.338	25.536
0.016	98.654	0.480	28.918
0.019	100.323	-0.257	31.070
0.022	101.231	0.118	32.009
0.026	101.318	0.108	32.480
0.030	101.650	0.522	31.828
0.034	101.483	0.330	31.025
0.038	101.238	-0.491	30.022
0.042	100.757	-0.891	29.311
0.051	100.997	-1.098	27.888
0.059	101.417	-1.520	25.705
0.067	101.763	-1.733	24.263
0.093	101.978	-1.713	19.616
0.134	101.775	-1.693	15.917
0.218	101.998	-1.468	12.125
0.301	100.086	-1.409	9.564
0.384	100.525	-1.199	9.251
0.468	100.242	-0.964	7.744

TABLE B-9

ROUND/BASE TIP

INBOARD PROFILES FOR Z/C = 5, V_∞ = 104.199 ft/sec

R (ft)	V_z (fps)	V_r (fps)	V_θ (fps)
0.0	79.973	-1.651	0.0
0.002	81.865	-2.235	- 9.005
0.005	84.207	-2.809	-21.726
0.007	87.896	-5.478	-29.263
0.010	95.536	-6.805	-40.817
0.012	104.947	-6.943	-50.296
0.016	119.224	-7.205	-60.995
0.019	122.643	-7.161	-62.919
0.022	139.451	-8.005	-73.315
0.026	116.152	-6.931	-55.814
0.030	110.161	-6.331	-48.168
0.034	106.941	-4.868	-42.418
0.038	105.468	-3.104	-38.275
0.042	103.971	-2.666	-34.666
0.051	101.364	-1.757	-28.954
0.059	100.616	-1.074	-25.060
0.067	100.739	-0.842	-22.131
0.093	98.866	-0.533	-17.905
0.134	99.725	-0.536	-12.678
0.218	99.847	-0.082	- 8.638
0.301	99.488	-0.284	- 6.680
0.384	99.491	-0.059	- 6.199
0.468	99.479	-0.279	- 5.714

TABLE B-10

ROUND/BASE TIP

OUTBOARD PROFILES FOR Z/C = 5, V_∞ = 104.131 ft/sec

R (ft)	V_z (fps)	V_r (fps)	V_θ (fps)
0.0	79.875	-1.649	0.320
0.002	80.979	-1.139	8.919
0.005	81.251	-0.410	20.357
0.007	83.150	0.688	29.284
0.010	84.645	2.155	37.107
0.012	86.384	3.088	41.464
0.016	88.337	3.923	46.003
0.019	90.025	4.573	48.512
0.022	92.425	5.241	48.383
0.026	94.724	5.119	46.851
0.030	96.742	5.077	43.664
0.034	98.270	4.019	40.912
0.038	98.972	2.592	38.325
0.042	99.504	1.574	35.946
0.051	99.002	0.633	30.621
0.059	99.040	-0.394	26.818
0.067	99.492	-0.818	24.210
0.093	100.066	-1.014	18.522
0.134	98.355	-1.167	15.587
0.218	99.288	-1.399	11.558
0.301	98.756	-1.378	9.368
0.384	98.376	-1.141	8.117
0.468	97.937	-1.351	6.869

TABLE B-11

ROUND/BASE TIP

INBOARD PROFILES FOR Z/C = 20, V_∞ = 105.043 ft/sec

R (ft)	V_z (fps)	V_r (fps)	V_θ (fps)
0.0	80.357	-1.938	0.0
0.002	80.856	-2.781	- 6.522
0.005	83.352	-0.428	-15.854
0.007	84.841	-0.009	-21.345
0.010	88.334	-1.188	-28.294
0.012	94.795	-2.307	-34.881
0.016	100.268	-2.850	-39.555
0.019	106.492	-3.551	-44.679
0.023	109.283	-3.205	-45.848
0.026	110.858	-3.233	-47.102
0.030	108.367	-3.556	-41.220
0.034	108.136	-2.567	-38.823
0.038	104.520	-1.847	-32.306
0.042	103.586	-1.597	-29.564
0.051	104.319	-0.971	-26.901
0.059	103.943	-0.727	-24.130
0.067	103.466	-0.908	-22.074
0.093	102.826	-0.640	-16.976
0.134	102.329	-0.823	-13.548
0.218	102.404	-1.251	-10.480
0.301	103.236	-1.268	- 8.024
0.384	102.906	-1.474	- 6.584
0.468	102.817	-1.688	- 5.614

TABLE B-12

ROUND/BASE TIP

OUTBOARD PROFILES FOR Z/C = 20, V_∞ = 104.968 ft/sec

R (ft)	V_z (fps)	V_r (fps)	V_θ (fps)
0.0	80.471	-1.661	0.0
0.002	80.292	-2.501	6.424
0.005	81.761	-3.067	12.774
0.007	81.861	-2.272	19.464
0.010	83.164	-2.569	24.680
0.012	85.931	-2.618	29.359
0.016	88.920	-2.439	34.227
0.019	92.993	-2.304	38.850
0.023	94.897	-1.055	41.710
0.026	98.103	-0.513	41.734
0.030	99.809	-0.141	40.860
0.034	101.635	-0.386	38.867
0.038	102.227	-0.991	35.833
0.042	101.850	-1.370	33.018
0.051	101.935	-1.762	28.782
0.059	102.900	-1.981	26.364
0.067	103.220	-2.187	23.943
0.093	103.210	-2.167	19.193
0.134	102.901	-2.146	14.836
0.218	103.438	-1.932	11.297
0.301	101.660	-1.669	10.007
0.384	102.345	-1.246	9.166
0.468	102.038	-1.234	7.931

TABLE B-13

WINGLET (VORTEX 1)

INBOARD PROFILES FOR Z/C = 5, V_∞ = 103.743 ft/sec

R (ft)	V_z (fps)	V_r (fps)	V_θ (fps)
0.0	77.055	-1.591	0.622
0.002	79.221	-1.639	- 5.596
0.005	82.252	-2.501	-11.277
0.008	86.398	-3.301	-14.921
0.010	89.175	-3.794	-16.521
0.013	91.616	-4.029	-16.805
0.016	94.480	-3.571	-16.186
0.019	94.807	-3.118	-15.055
0.023	95.218	-2.894	-14.062
0.026	95.287	-2.438	-12.546
0.030	95.309	-2.209	-11.310
0.034	95.401	-1.981	-10.586
0.038	95.246	-1.977	- 9.858
0.043	95.227	-1.975	- 9.347
0.051	95.179	-1.972	- 8.327
0.059	96.625	-2.001	- 7.744
0.067	97.677	-1.798	- 6.916
0.093	98.694	-1.818	- 4.894
0.134	95.809	-1.752	- 5.286
0.218	98.366	-1.812	- 5.883
0.301	98.541	-1.592	- 4.898
0.384	98.458	-1.366	- 3.923
0.468	98.315	-1.361	- 3.672

TABLE B-14

WINGLET (VORTEX 1)

OUTBOARD PROFILES FOR Z/C = 5, V_∞ = 104.283 ft/sec

R (ft)	V_z (fps)	V_r (fps)	V_θ (fps)
0.0	77.506	-1.883	0.0
0.002	77.766	-1.047	6.559
0.005	79.670	-0.576	13.057
0.008	82.427	-0.172	17.525
0.010	86.388	0.393	21.089
0.013	89.297	0.733	22.365
0.016	92.301	0.825	22.249
0.019	93.695	0.313	21.095
0.023	94.660	-0.398	19.614
0.026	95.347	-0.870	18.636
0.030	96.060	-1.563	17.366
0.034	96.601	-1.571	16.192
0.038	97.221	-1.807	15.417
0.043	97.410	-1.809	14.617
0.051	97.072	-1.799	13.950
0.059	95.597	-1.535	13.675
0.067	95.139	-1.524	13.679
0.093	96.818	-1.343	14.489
0.134	98.750	-1.385	11.798
0.218	98.544	-1.596	9.326
0.301	97.840	-1.800	7.600
0.384	97.408	-1.788	6.618
0.468	97.321	-1.104	6.412

TABLE B-15

WINGLET (VORTEX 2)

INBOARD PROFILES FOR Z/C = 5, V_∞ = 105.097 ft/sec

R (ft)	V_z (fps)	V_r (fps)	V_θ (fps)
0.0	66.212	-1.367	- 0.377
0.002	69.387	-1.120	- 7.758
0.005	71.204	-1.807	-13.866
0.007	81.371	-3.338	-19.814
0.010	86.732	-3.854	-22.927
0.012	90.510	-3.612	-24.175
0.016	94.435	-2.705	-24.324
0.019	96.105	-1.813	-23.244
0.022	97.393	-1.159	-21.987
0.026	97.957	-0.492	-20.528
0.030	98.494	0.626	-18.557
0.034	98.914	1.294	-16.821
0.038	99.114	1.292	-15.923
0.042	99.218	1.743	-14.928
0.051	100.028	1.704	-13.835
0.059	99.312	1.759	-12.289
0.067	99.096	1.779	-11.504
0.093	100.166	1.729	- 9.457
0.134	100.150	1.742	- 6.740
0.218	100.008	1.755	- 5.257
0.301	99.999	1.085	- 3.994
0.384	99.966	0.639	- 3.493
0.468	99.950	0.188	- 3.492

TABLE B-16

WINGLET (VORTEX 2)

OUTBOARD PROFILES FOR Z/C = 5, V_∞ = 105.211 ft/sec

R (ft)	V_z (fps)	V_r (fps)	V_θ (fps)
0.0	67.113	-1.049	0.759
0.002	69.505	-1.128	9.943
0.005	74.026	-0.388	17.958
0.007	80.176	1.250	23.173
0.010	86.485	2.622	26.391
0.013	90.571	3.297	26.952
0.016	94.623	3.487	25.883
0.019	96.687	2.687	24.559
0.023	97.697	2.420	23.083
0.026	98.473	1.950	21.200
0.030	98.870	1.725	19.439
0.034	99.470	1.709	17.932
0.038	99.910	1.692	17.246
0.043	100.147	1.467	15.974
0.051	100.206	1.699	14.429
0.059	100.729	1.680	13.115
0.067	101.078	1.890	11.879
0.093	99.214	2.012	10.331
0.134	99.936	1.974	9.207
0.218	99.158	1.808	6.954
0.301	98.936	1.824	6.223
0.384	98.791	1.605	5.979
0.468	98.907	1.145	5.736

TABLE B-17

WINGLET (VORTEX 1)

INBOARD PROFILES FOR Z/C = 20, V_∞ = 105.183 ft/sec

R (ft)	V_z (fps)	V_r (fps)	V_θ (fps)
0.0	89.804	-1.854	- 0.562
0.002	90.939	-2.125	- 2.510
0.005	92.505	-2.156	- 6.038
0.007	94.136	-2.425	- 7.551
0.010	94.750	-2.202	- 9.603
0.012	96.215	-2.231	-10.716
0.016	97.401	-2.254	-11.356
0.019	98.748	-2.956	-11.094
0.023	99.447	-2.739	-10.533
0.026	99.558	-2.516	-10.268
0.030	99.917	-1.849	- 9.980
0.034	100.015	-1.401	- 9.236
0.038	100.654	-1.640	- 9.021
0.042	100.733	-1.640	- 8.234
0.051	101.171	-1.650	- 7.694
0.059	101.254	-1.651	- 6.953
0.067	101.294	-1.873	- 6.194
0.093	101.788	-1.882	- 4.931
0.134	101.893	-2.105	- 4.700
0.218	102.725	-2.779	- 3.420
0.301	102.620	-4.314	- 1.719
0.384	102.755	-6.284	- 2.465
0.468	102.772	-6.718	- 5.650

TABLE B-18

WINGLET (VORTEX 1)

OUTBOARD PROFILES FOR Z/C = 20, V_∞ = 105.487 ft/sec

R (ft)	V_z (fps)	V_r (fps)	V_θ (fps)
0.0	89.761	-1.853	0.0
0.002	89.336	-2.352	5.068
0.005	90.380	-1.875	9.028
0.007	91.425	-2.146	10.921
0.010	92.628	-1.694	14.584
0.012	92.271	-1.443	14.289
0.016	93.968	-0.069	16.375
0.019	96.379	-0.644	18.911
0.023	97.805	-0.012	19.350
0.026	98.157	-0.251	19.114
0.030	98.536	-0.489	18.791
0.034	99.907	-0.753	17.629
0.038	100.275	-0.760	16.678
0.042	100.665	-0.993	16.450
0.051	100.807	-1.214	15.170
0.059	100.909	-1.214	14.428
0.067	101.097	-1.439	13.852
0.093	101.462	-1.225	13.119
0.134	102.758	-1.040	12.271
0.218	102.126	-0.793	10.347
0.301	102.199	-0.570	9.298
0.384	101.888	-0.777	8.063
0.468	101.698	-0.993	7.821

TABLE B-19

WINGLET (VORTEX 2)

INBOARD PROFILES FOR Z/C = 20, V_∞ = 103.722 ft/sec

R (ft)	V_z (fps)	V_r (fps)	V_θ (fps)
0.0	85.745	-1.770	0.0
0.002	86.057	-2.029	- 2.819
0.005	86.378	-2.287	- 5.613
0.007	87.926	-2.315	- 9.335
0.010	88.380	-1.842	-12.236
0.012	91.149	-2.377	-15.170
0.016	92.299	-2.399	-16.878
0.019	94.056	-1.749	-17.824
0.023	96.484	-1.146	-19.015
0.026	97.358	-1.391	-19.116
0.030	98.625	-0.771	-18.627
0.034	99.166	-0.132	-17.462
0.038	99.809	-0.152	-16.852
0.042	99.885	0.066	-16.176
0.051	100.105	0.071	-14.213
0.059	100.428	0.062	-13.537
0.067	100.382	-0.142	-11.879
0.093	100.432	-0.352	-10.278
0.134	100.841	-0.576	- 8.371
0.218	101.711	-1.244	- 6.435
0.301	101.378	-1.448	- 5.020
0.384	101.452	-1.664	- 4.295
0.468	101.274	-1.659	- 3.572

TABLE B-20

WINGLET (VORTEX 2)

OUTBOARD PROFILES FOR Z/C = 20, V_∞ = 104.527 ft/sec

R (ft)	V_z (fps)	V_r (fps)	V_θ (fps)
0.0	87.414	-1.804	0.0
0.002	87.793	-2.066	4.995
0.005	89.519	-0.869	6.776
0.007	92.524	-0.259	10.119
0.010	93.499	0.872	11.509
0.013	95.618	0.759	12.974
0.016	97.790	0.873	13.851
0.019	99.355	0.797	13.860
0.023	100.159	0.761	13.535
0.026	100.440	0.752	13.023
0.030	101.196	0.506	12.002
0.034	101.715	0.489	10.992
0.038	101.629	0.281	10.044
0.043	101.286	0.302	9.051
0.051	100.995	0.539	7.850
0.059	101.033	0.322	6.883
0.067	100.820	0.333	6.183
0.093	100.826	0.339	4.536
0.134	101.613	0.965	2.378
0.218	101.460	2.072	- 0.727
0.301	101.376	3.614	0.243
0.384	100.569	5.652	3.137
0.468	100.890	5.822	7.431

TABLE B-21

UPPER WINGLET (VORTEX 1)

INBOARD PROFILES FOR Z/C = 5, V_∞ = 104.006 ft/sec

R (ft)	V_z (fps)	V_r (fps)	V_θ (fps)
0.0	85.791	-1.771	0.0
0.002	86.398	-2.038	- 1.424
0.005	87.077	-2.050	- 2.551
0.007	87.664	-2.562	- 3.949
0.010	88.316	-2.571	- 5.055
0.012	89.357	-2.585	- 6.386
0.016	90.074	-2.595	- 7.707
0.019	90.761	-2.605	- 8.455
0.022	91.763	-2.618	- 8.851
0.026	92.818	-2.868	- 9.318
0.030	93.572	-2.876	- 9.723
0.034	94.485	-2.887	- 9.875
0.038	95.089	-3.124	- 9.550
0.042	95.621	-2.900	- 9.530
0.051	96.961	-2.915	- 9.166
0.059	97.756	-3.148	- 8.322
0.067	98.256	-3.153	- 7.818
0.092	96.872	-3.368	- 6.638
0.134	98.506	-3.826	- 8.285
0.217	99.434	-3.606	- 6.443
0.301	99.143	-2.716	- 5.460
0.384	99.323	-2.275	- 4.948
0.467	99.305	-2.274	- 4.947

TABLE B-22

UPPER WINGLET (VORTEX 1)

OUTBOARD PROFILES FOR Z/C = 5, V_∞ = 104.282 ft/sec

R (ft)	V_z (fps)	V_r (fps)	V_θ (fps)
0.0	85.879	-1.773	0.0
0.002	86.199	-1.780	1.710
0.005	85.435	-1.765	3.391
0.007	85.669	-1.771	4.819
0.010	86.130	-1.527	6.783
0.012	87.002	-1.550	8.136
0.016	88.061	-1.829	9.742
0.019	88.533	-1.595	11.600
0.022	89.495	-1.622	13.037
0.026	90.951	-1.660	14.239
0.030	91.805	-1.920	15.094
0.034	92.950	-1.946	15.670
0.038	93.705	-1.730	16.033
0.042	94.676	-1.983	16.429
0.051	95.943	-2.008	15.971
0.059	96.825	-2.251	15.660
0.067	97.217	-2.256	15.133
0.093	98.467	-2.276	14.131
0.134	99.107	-2.505	12.118
0.218	98.822	-2.496	9.397
0.301	98.042	-2.256	7.900
0.384	97.808	-2.024	6.942
0.468	97.144	-1.781	6.229

TABLE B-23

UPPER WINGLET (VORTEX 2)

INBOARD PROFILES FOR Z/C = 5, V_∞ = 102.198 ft/sec

R (ft)	V_z (fps)	V_r (fps)	V_θ (fps)
0.0	73.414	-1.802	0.0
0.002	75.177	-1.836	- 6.154
0.005	78.626	-2.433	-10.930
0.007	82.639	-2.736	-15.183
0.010	85.499	-2.765	-16.818
0.012	88.666	-2.799	-18.110
0.016	90.813	-2.139	-17.982
0.019	92.069	-1.484	-17.403
0.023	93.471	-1.073	-17.066
0.026	94.186	-0.423	-15.749
0.030	95.038	-0.009	-15.071
0.034	95.715	0.191	-13.769
0.038	95.566	0.861	-13.109
0.042	96.086	0.843	-12.321
0.051	95.803	0.864	-11.421
0.059	96.038	0.857	-10.957
0.067	96.556	1.055	-10.154
0.093	97.198	1.251	- 8.206
0.134	97.439	0.813	- 6.042
0.218	97.346	0.606	- 4.596
0.301	97.190	0.179	- 3.881
0.384	97.156	-0.255	- 3.395
0.468	97.041	-0.688	- 3.148

TABLE B-24

UPPER WINGLET (VORTEX 2)

OUTBOARD PROFILES FOR Z/C = 5, V_∞ = 102.990 ft/sec

R (ft)	V_z (fps)	V_r (fps)	V_θ (fps)
0.0	73.606	-1.519	- 0.322
0.003	74.190	-0.962	6.075
0.005	78.515	-0.294	12.176
0.008	81.575	0.090	15.563
0.010	85.560	0.641	18.319
0.013	88.664	1.430	19.366
0.016	91.375	1.739	19.572
0.019	93.174	1.648	18.726
0.023	94.064	1.608	17.855
0.026	95.194	1.559	16.790
0.030	96.054	1.521	15.771
0.034	96.394	1.511	14.749
0.038	96.561	1.512	13.958
0.043	97.153	1.488	12.921
0.051	98.057	1.667	11.605
0.059	98.140	1.670	10.639
0.068	97.626	1.927	9.973
0.093	95.713	2.048	9.663
0.134	97.915	2.355	9.137
0.218	97.162	1.757	6.959
0.301	96.946	1.329	6.282
0.384	96.845	1.116	6.048
0.468	96.796	0.897	6.302

TABLE B-25

UPPER WINGLET (VORTEX 1)

INBOARD PROFILES FOR Z/C = 20, V_∞ = 104.683 ft/sec

R (ft)	V_z (fps)	V_r (fps)	V_θ (fps)
0.0	91.905	-1.897	0.0
0.003	92.636	-2.873	- 1.331
0.005	92.849	-2.396	- 2.124
0.008	92.851	-1.918	- 2.921
0.010	93.576	-1.696	- 4.515
0.013	93.723	-1.700	- 4.763
0.016	94.690	-2.428	- 6.497
0.019	95.616	-3.140	- 7.220
0.023	96.237	-2.915	- 7.907
0.026	96.675	-2.692	- 8.650
0.030	97.308	-2.473	- 8.854
0.034	98.397	-2.040	- 8.989
0.038	98.696	-1.821	- 8.995
0.043	99.296	-1.610	- 8.692
0.051	100.226	-1.188	- 8.116
0.059	100.317	-0.525	- 7.858
0.068	101.033	-0.548	- 7.349
0.093	101.476	-0.121	- 5.604
0.134	101.659	0.315	- 3.886
0.218	102.025	2.709	- 2.178
0.301	102.196	5.306	- 3.395
0.384	102.595	3.954	- 6.793
0.468	102.250	2.025	- 7.304

TABLE B-26

UPPER WINGLET (VORTEX 1)

OUTBOARD PROFILES FOR Z/C = 20, V_∞ = 105.015 ft/sec

R (ft)	V_z (fps)	V_r (fps)	V_θ (fps)
0.0	91.902	-1.897	0.0
0.002	92.099	-1.415	1.077
0.005	91.603	-1.159	2.937
0.007	91.529	-0.670	4.805
0.010	91.968	-0.931	6.389
0.012	92.280	-0.942	7.176
0.016	93.047	-0.732	9.048
0.019	94.033	-0.769	10.542
0.023	94.919	-0.569	11.966
0.026	95.291	-0.816	12.182
0.030	95.949	-0.610	13.278
0.034	97.071	-0.425	14.158
0.038	97.730	-0.449	14.299
0.042	98.149	-0.239	14.510
0.051	99.277	-0.505	14.363
0.059	99.993	-0.304	13.485
0.067	100.484	-0.541	13.022
0.093	101.471	-0.351	11.954
0.134	102.175	-0.373	10.946
0.218	102.099	0.075	9.428
0.301	101.745	0.093	8.465
0.384	101.315	0.116	7.221
0.468	101.230	-0.098	6.264

TABLE B-27

UPPER WINGLET (VORTEX 2)

INBOARD PROFILES FOR Z/C = 20, V_∞ = 103.386 ft/sec

R (ft)	V_z (fps)	V_r (fps)	V_θ (fps)
0.0	86.679	-1.789	0.0
0.002	86.827	-1.793	- 2.461
0.005	87.294	-1.805	- 5.439
0.007	87.830	-2.307	- 7.807
0.010	88.309	-3.043	- 9.618
0.012	90.728	-2.599	-14.610
0.016	91.212	-3.072	-14.895
0.019	92.755	-3.544	-16.395
0.022	94.837	-3.331	-17.482
0.026	95.422	-3.114	-17.538
0.030	96.863	-2.471	-17.668
0.034	97.847	-2.049	-16.779
0.038	98.386	-1.624	-15.985
0.042	98.670	-1.844	-15.197
0.051	99.311	-1.855	-14.261
0.059	99.419	-1.420	-12.832
0.067	99.821	-1.427	-11.866
0.093	100.331	-1.651	-10.221
0.134	100.530	-1.867	- 8.383
0.218	101.058	-2.091	- 7.107
0.301	101.222	-1.878	- 5.704
0.384	100.925	-1.870	- 4.759
0.468	100.997	-2.086	- 4.038

TABLE B-28

UPPER WINGLET (VORTEX 2)

OUTBOARD PROFILES FOR Z/C = 20, V_∞ = 104.132 ft/sec

R (ft)	V_z (fps)	V_r (fps)	V_θ (fps)
0.0	88.257	-2.069	0.0
0.002	88.026	-2.066	2.430
0.005	89.297	-1.846	4.514
0.007	90.525	-1.392	6.815
0.010	93.148	-0.994	8.446
0.012	94.862	-2.198	9.943
0.016	96.597	-2.006	10.508
0.019	97.115	-2.018	11.215
0.023	98.310	-2.042	11.031
0.026	99.047	-2.497	10.712
0.030	99.614	-2.066	9.850
0.034	99.860	-2.070	9.347
0.038	99.946	-2.509	8.593
0.042	99.855	-2.726	7.884
0.051	100.167	-2.949	6.662
0.059	99.986	-3.386	5.962
0.067	100.145	-3.168	5.003
0.093	100.562	-3.610	2.856
0.134	101.107	-4.269	1.432
0.218	101.536	-6.002	- 0.239
0.301	100.653	-8.418	1.449
0.384	100.212	-8.213	6.998
0.468	100.474	-4.711	7.880

TABLE B-29

LOWER WINGLET

INBOARD PROFILES FOR Z/C = 5, V_∞ = 102.921 ft/sec

R (ft)	V_z (fps)	V_r (fps)	V_θ (fps)
0.0	74.187	-1.531	- 0.694
0.002	74.209	-2.113	- 9.781
0.005	77.243	-1.910	-19.291
0.007	82.183	-2.765	-25.947
0.010	87.638	-3.290	-30.662
0.012	92.410	-3.545	-33.601
0.016	95.653	-3.563	-33.327
0.019	96.531	-3.566	-31.730
0.022	97.113	-2.726	-29.572
0.026	97.476	-2.091	-27.535
0.030	97.481	-1.653	-25.131
0.034	97.080	-0.988	-22.943
0.038	97.086	-0.764	-21.852
0.042	97.217	-0.544	-20.580
0.051	97.291	-0.532	-18.766
0.059	97.853	-0.325	-17.269
0.067	98.483	-0.336	-15.516
0.093	98.112	-0.086	-12.230
0.134	98.075	-0.072	- 9.659
0.218	97.905	-0.273	- 7.062
0.301	97.757	-0.262	- 5.860
0.384	98.001	-0.488	- 5.371
0.468	98.103	-0.489	- 5.377

TABLE B-30

LOWER WINGLET

OUTBOARD PROFILES FOR Z/C = 5, V_∞ = 103.250 ft/sec

R (ft)	V_z (fps)	V_r (fps)	V_θ (fps)
0.0	75.145	-1.551	0.0
0.002	77.352	-0.769	7.901
0.005	81.618	0.636	15.019
0.007	85.162	1.435	18.229
0.010	89.690	2.342	20.325
0.012	92.785	2.822	20.572
0.016	95.682	2.861	19.716
0.019	97.919	2.737	17.528
0.023	98.845	2.916	15.229
0.026	99.047	2.704	13.420
0.030	99.421	2.477	11.767
0.034	99.546	2.911	10.250
0.038	99.170	2.943	9.276
0.042	98.604	3.427	8.041
0.051	97.938	4.364	6.869
0.059	97.580	5.276	6.414
0.067	97.518	6.381	6.425
0.093	98.445	8.642	9.383
0.134	98.306	7.484	16.197
0.218	98.478	1.664	13.006
0.301	98.232	-0.278	9.941
0.384	97.495	-0.909	8.270
0.468	97.216	-0.897	7.307

TABLE B-31

LOWER WINGLET

INBOARD PROFILES FOR Z/C = 20, V_∞ = 104.004 ft/sec

R (ft)	V_z (fps)	V_r (fps)	V_θ (fps)
0.0	93.132	-1.922	- 0.263
0.002	93.337	-1.453	- 2.389
0.005	94.052	-1.474	- 5.269
0.007	94.690	-1.494	- 7.318
0.010	95.084	-1.505	- 8.055
0.012	94.994	-1.506	- 9.305
0.016	95.831	-1.533	-11.201
0.019	96.598	-1.557	-12.847
0.023	97.629	-2.035	-13.676
0.026	98.366	-3.831	-14.514
0.030	99.158	-3.834	-15.346
0.034	99.760	-3.398	-15.471
0.038	100.512	-3.404	-15.863
0.042	101.258	-2.978	-15.453
0.051	102.030	-2.558	-15.125
0.059	102.128	-2.345	-14.932
0.067	102.131	-2.128	-14.181
0.093	102.067	-1.478	-12.584
0.134	102.795	-1.278	-10.629
0.218	102.456	-1.263	- 8.337
0.301	102.615	-1.262	- 5.719
0.384	102.213	-1.249	- 4.289
0.468	102.096	-1.461	- 3.339

TABLE B-32

LOWER WINGLET

OUTBOARD PROFILES FOR Z/C = 20, V_∞ = 103.745 ft/sec

R (ft)	V_z (fps)	V_r (fps)	V_θ (fps)
0.0	92.456	-1.908	0.0
0.002	92.115	-1.424	2.867
0.005	92.008	-1.184	4.676
0.008	92.384	-1.438	7.253
0.010	93.312	-1.702	9.881
0.013	93.702	-1.483	11.614
0.016	93.982	-1.266	13.828
0.019	94.909	-1.072	15.960
0.023	95.663	-1.554	17.380
0.026	95.743	-1.562	18.483
0.030	96.395	-1.585	19.903
0.034	97.591	-1.400	21.108
0.038	98.190	-1.420	21.677
0.043	99.027	-1.442	21.706
0.051	99.874	-1.465	21.739
0.059	100.927	-1.488	20.864
0.068	101.230	-1.707	20.642
0.093	101.456	-1.704	18.867
0.134	101.902	-1.706	16.639
0.218	102.162	-1.485	12.668
0.301	100.901	-1.447	11.408
0.384	101.681	-1.466	10.583
0.468	101.536	-1.460	9.622

APPENDIX C

WIND TUNNEL DESCRIPTION

6 Foot Subsonic, Stability Wind Tunnel

This facility may be classified as a continuous, closed jet, single return, subsonic wind tunnel with interchangeable round and square test sections. General design features are illustrated in the drawing in Figure 2. The tunnel is powered by a 600 hp. d. c. motor driving a 14 foot propeller providing a maximum speed of 220 feet/second and a Reynolds' number per foot up to 1.33×10^6.

The instrumentation available is of a class and variety to permit efficient and accurate detailed studies in nearly all phases of work commonly encountered in wind tunnel practice. The tunnel is equipped with two balance systems. A six-component automatic null balancing mechanical system is provided for measuring forces and moments on models mounted through the floor or sidewall of the tunnel during static model tests. A six-component electric strain gage balance system is available for use with either static tests or tests during which the model is undergoing steady or oscillatory motion. Both systems feed their output into a readout printing system which allows the operator to read six outputs either from indicator dials or as printed tabulations. Conventional pressure measuring equipment consisting of manometer banks, survey rakes and boundary layer mice enable detailed pressure and velocity distribution studies to be made.

Table 1. Lift and Drag Data.

Configuration	α (degrees)	C_L	C_D	L/D
Square Tip	2	.189	.018	10.32
	6	.489	.042	11.69
	10	.718	.070	10.23
Round/Base	2	.193	.018	10.53
	6	.484	.042	11.46
	10	.718	.071	10.13
Pointed Tip	2	.206	.019	10.59
	6	.527	.044	12.08
	10	.785	.073	10.78
Winglet	2	.227	.022	10.08
	6	.578	.045	12.81
	10	.840	.072	11.61
Upper Winglet	2	.214	.022	9.91
	6	.554	.044	12.68
	10	.806	.069	11.63
Lower Winglet	2	.208	.019	10.71
	6	.517	.043	11.94
	10	.748	.071	10.54

Table 2. Data for Effects of Wing-Winglet Interaction.

Configuration	C_L	C_D	C_Y	L/D
Square Tip	.4895	.0419	NA	11.687
Wing with attached winglet	.5781	.0451	NA	12.811
Winglet alone	.0040	.0046	-.0115	.8696
Wing with winglet adjacent	.5605	.0431	NA	13.007
Winglet with wing adjacent	.0164	.0006	.0218	26.330

Note: a. $\alpha = 6°$

b. All calculations are based on wing area = 2.222 ft^2.

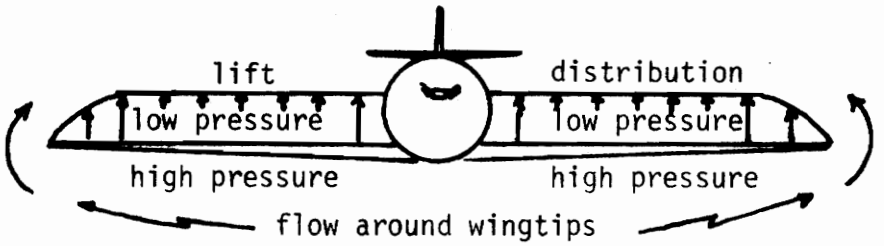

a. Vortex Production by Aircraft Lift

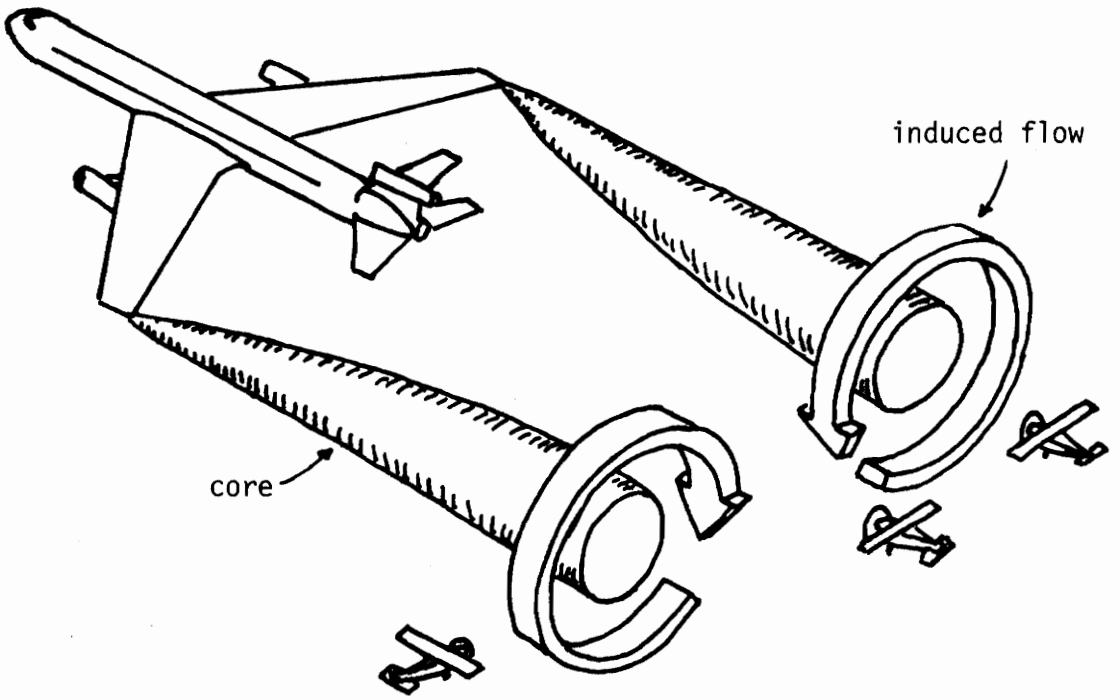

b. Trailing Vortices and Typical Encounters

Fig. 1. Trailing Vortex System.

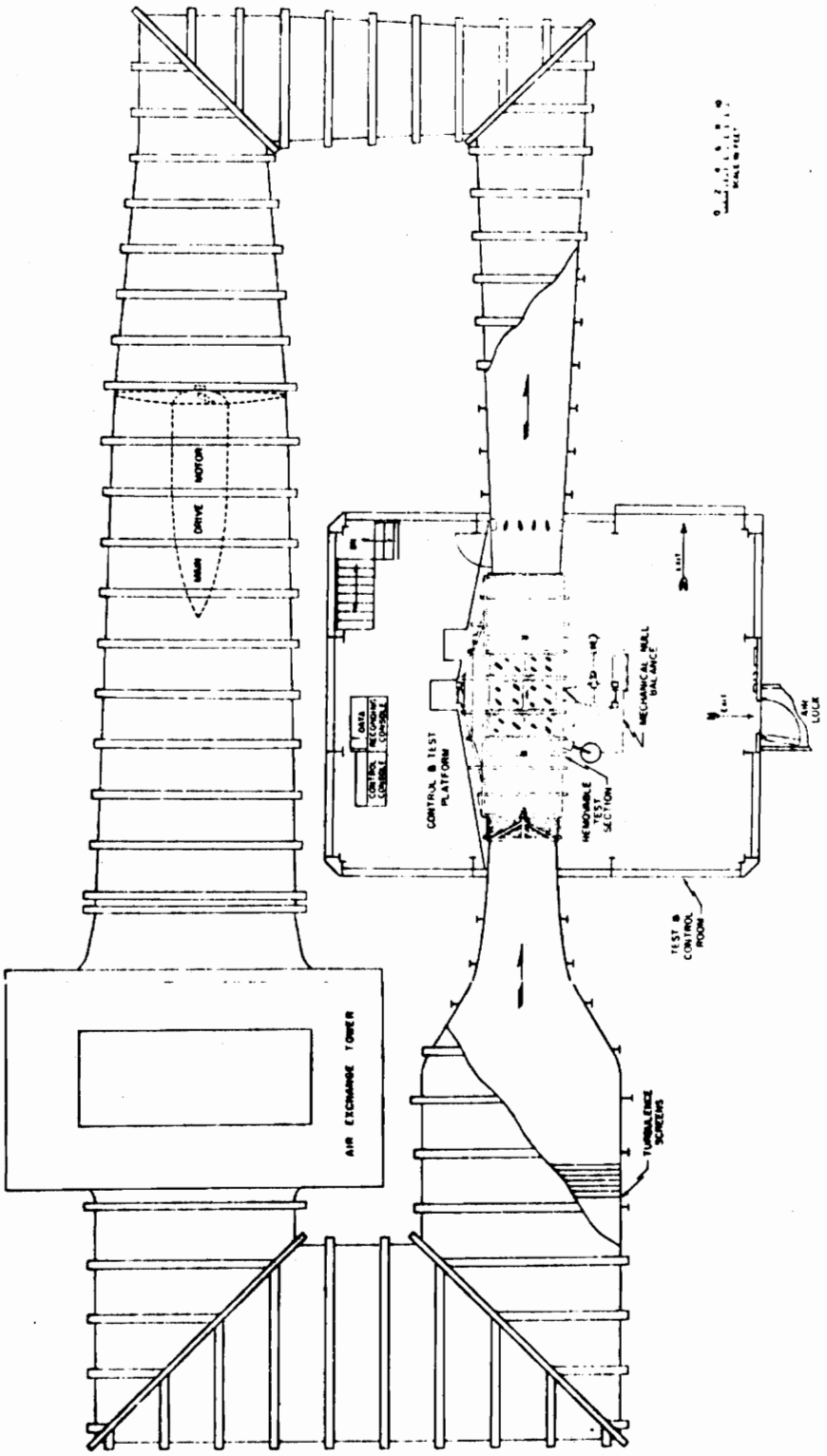

Fig. 2. VPI & SU 6-Foot Subsonic Wind Tunnel.

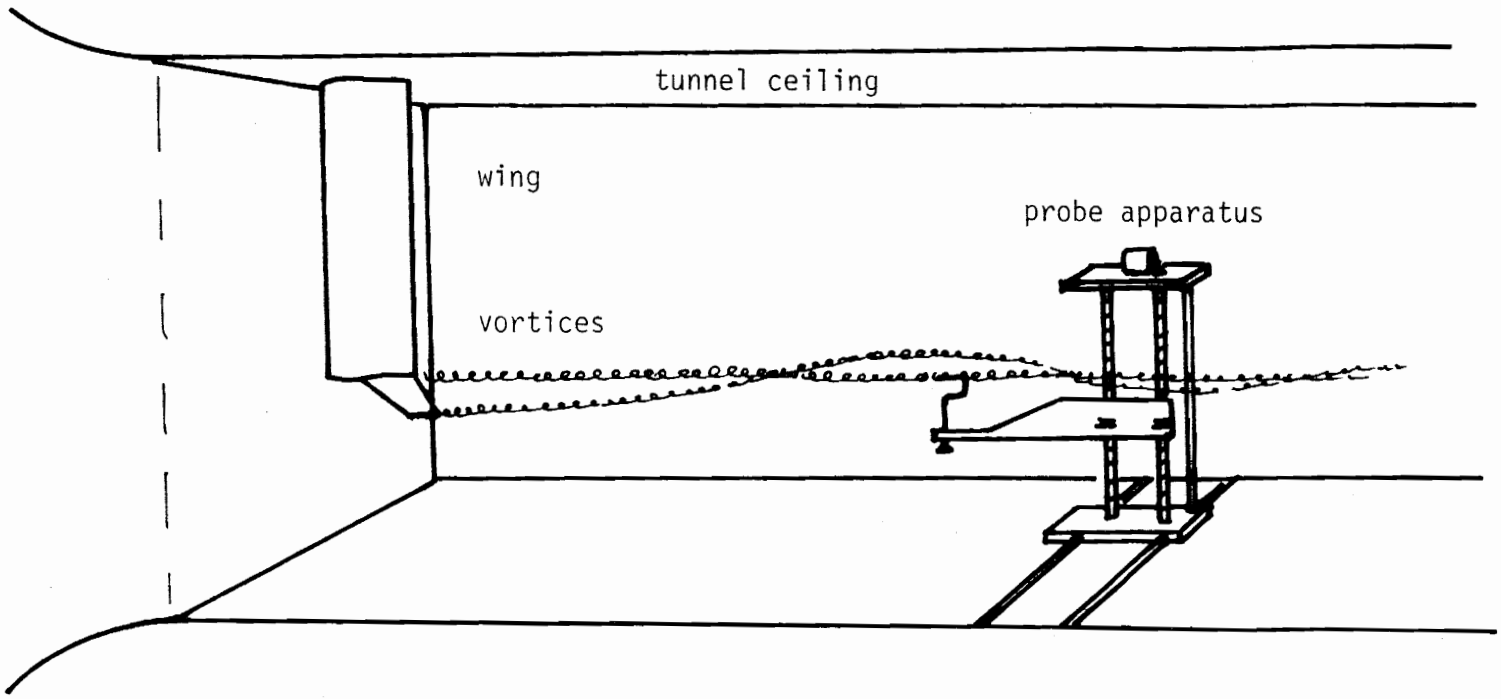

Fig. 3. Schematic of Test Set-Up.

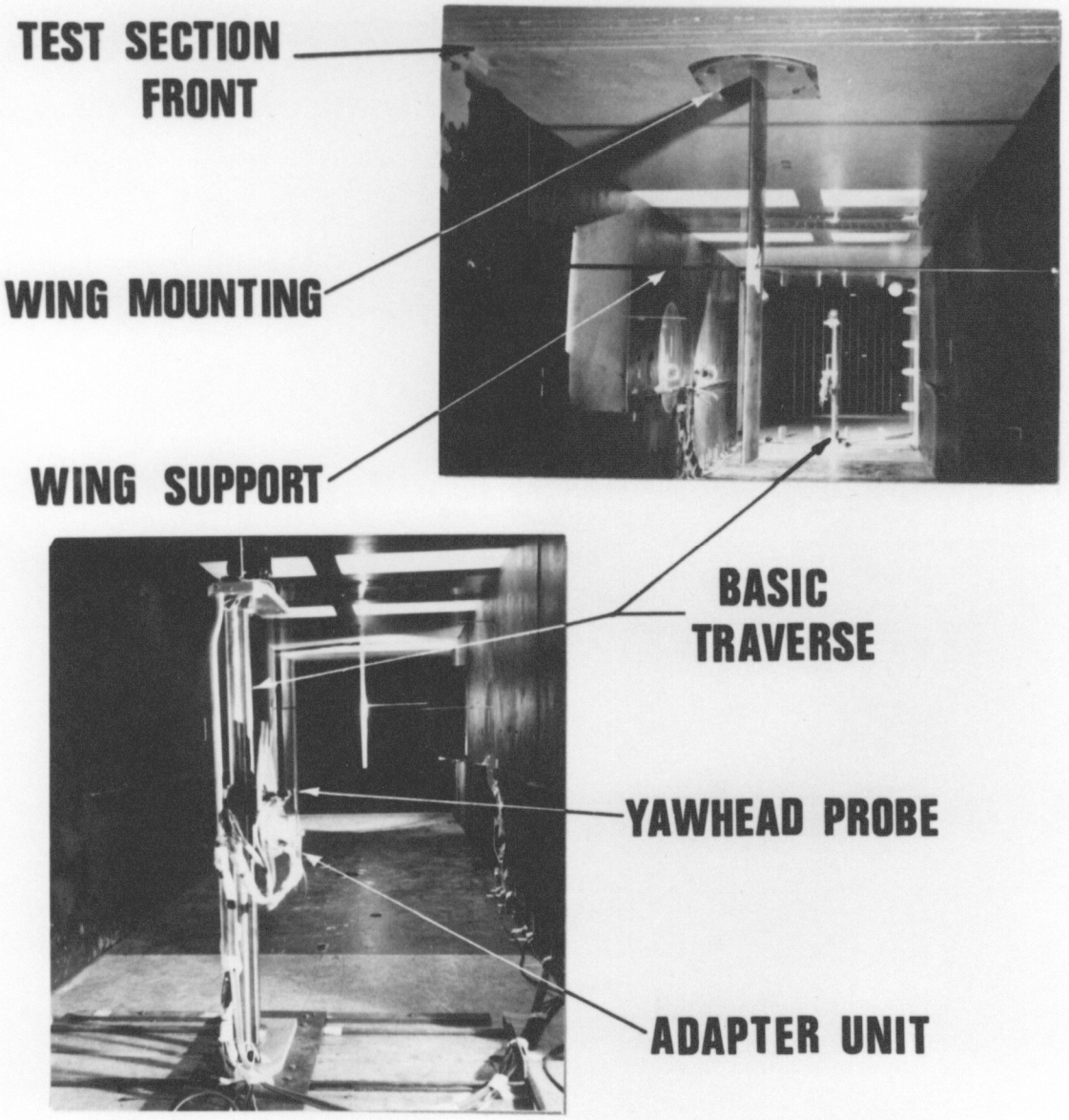

Fig. 4. Wind Tunnel Test Set-Up.

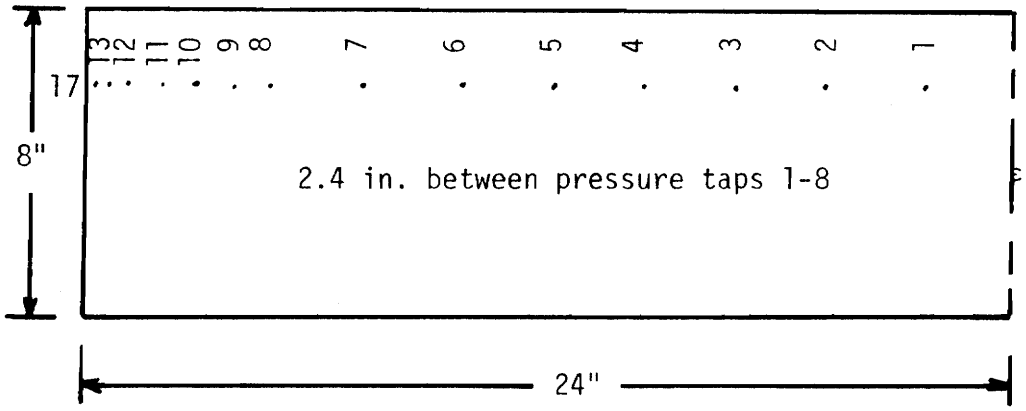

a. Spanwise Taps

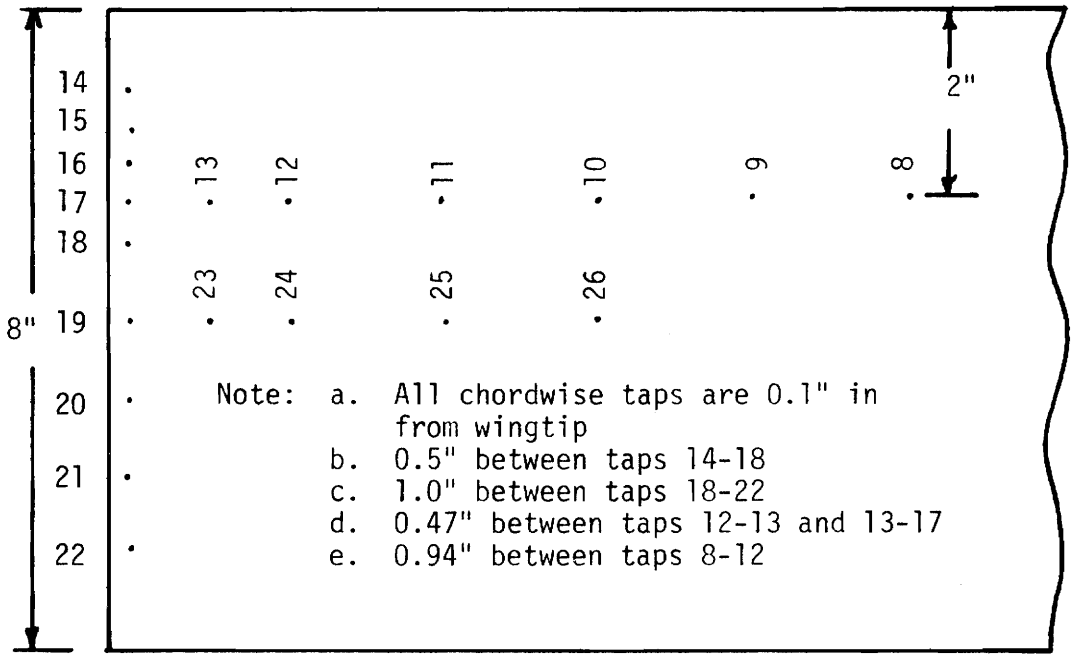

b. Blow-up of Taps on Wingtip

Fig. 5. Pressure Taps (AR = 12).

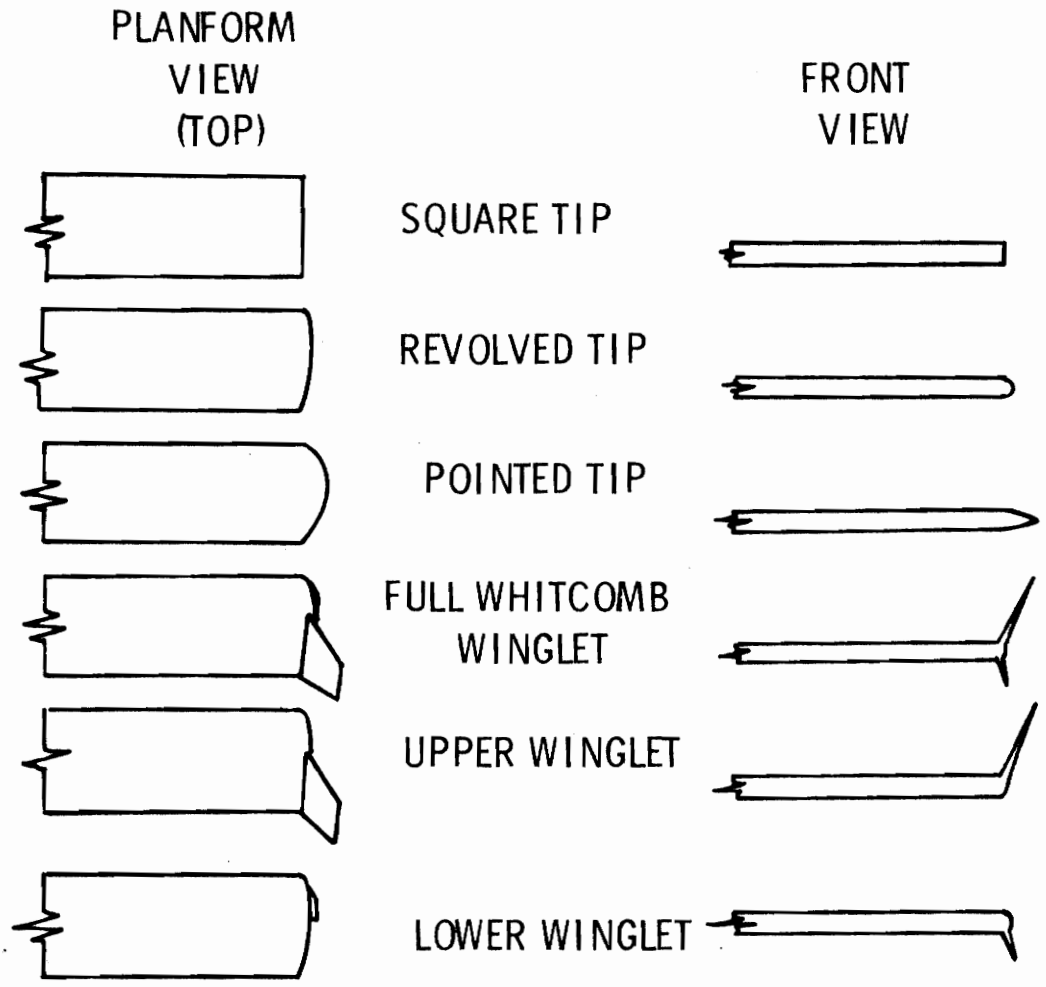

Fig. 6. Wing Tip Test Configurations (Schematic).

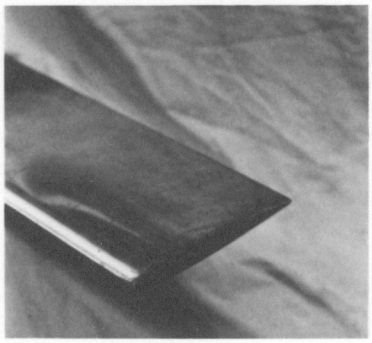

a. Square Tip

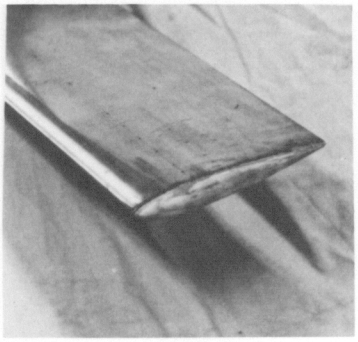

b. Round Tip

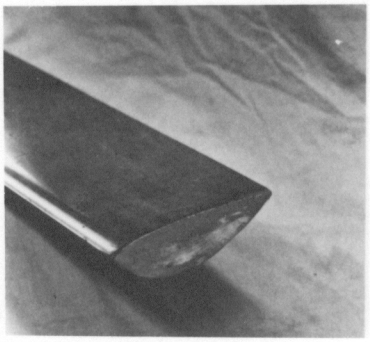

c. Pointed Tip

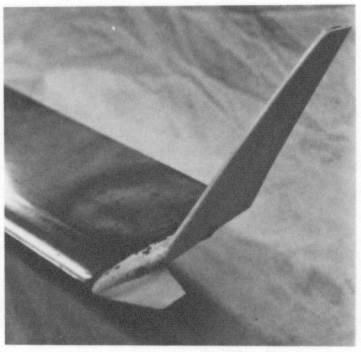

d. Whitcomb Winglet

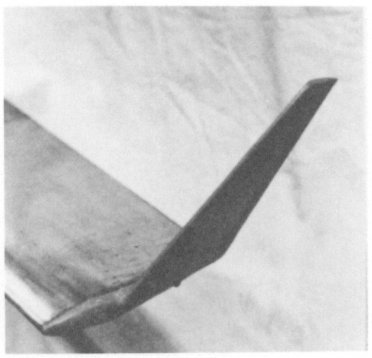

e. Upper Winglet

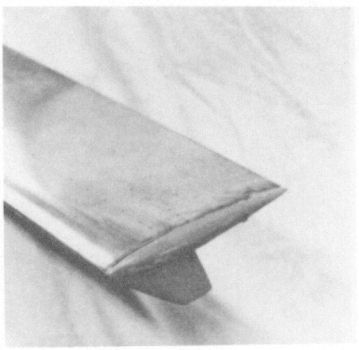

f. Lower Winglet

Fig. 7. Wing Tip Test Configurations.

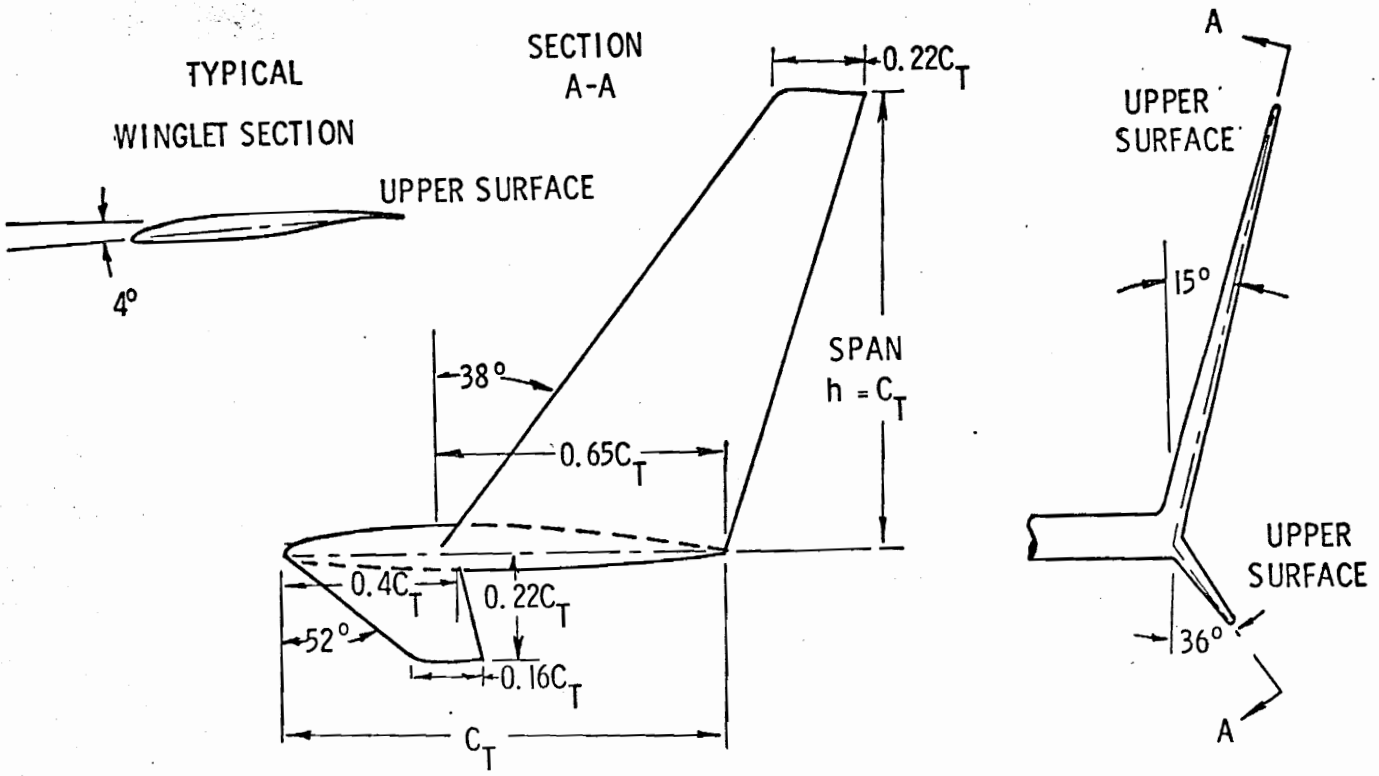

Fig. 8. Whitcomb Winglet.

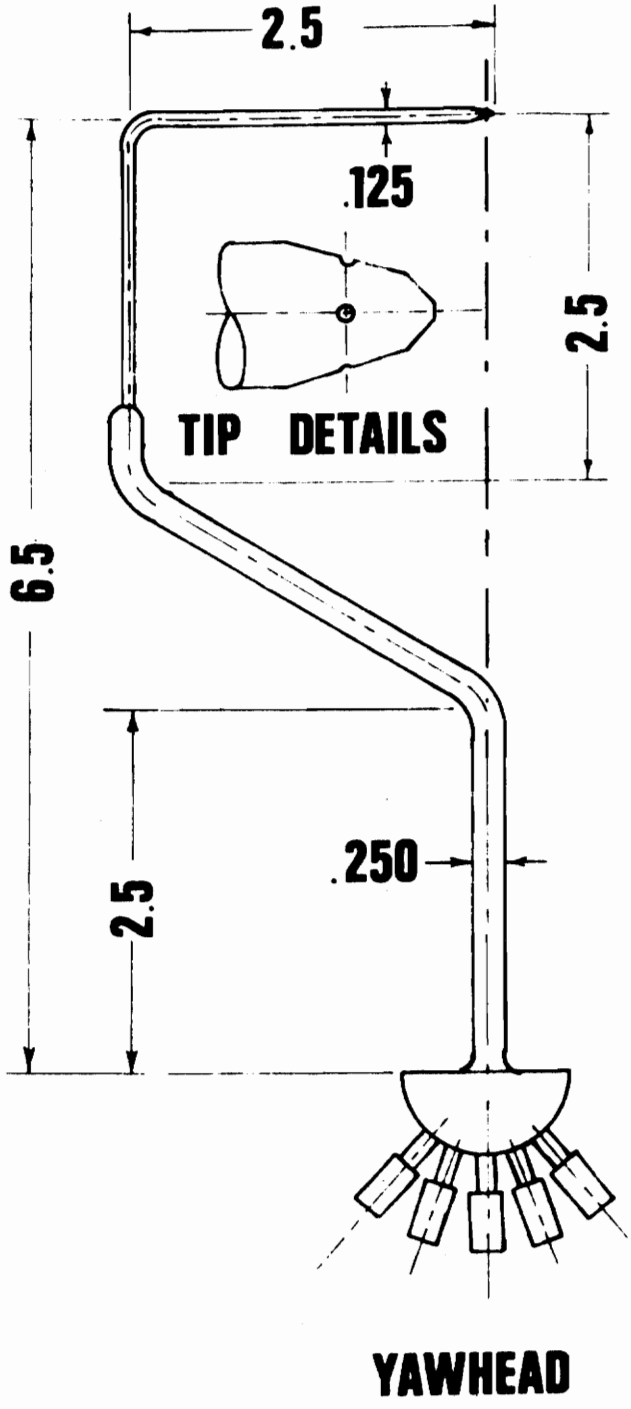

Fig. 9. Yawhead Probe.

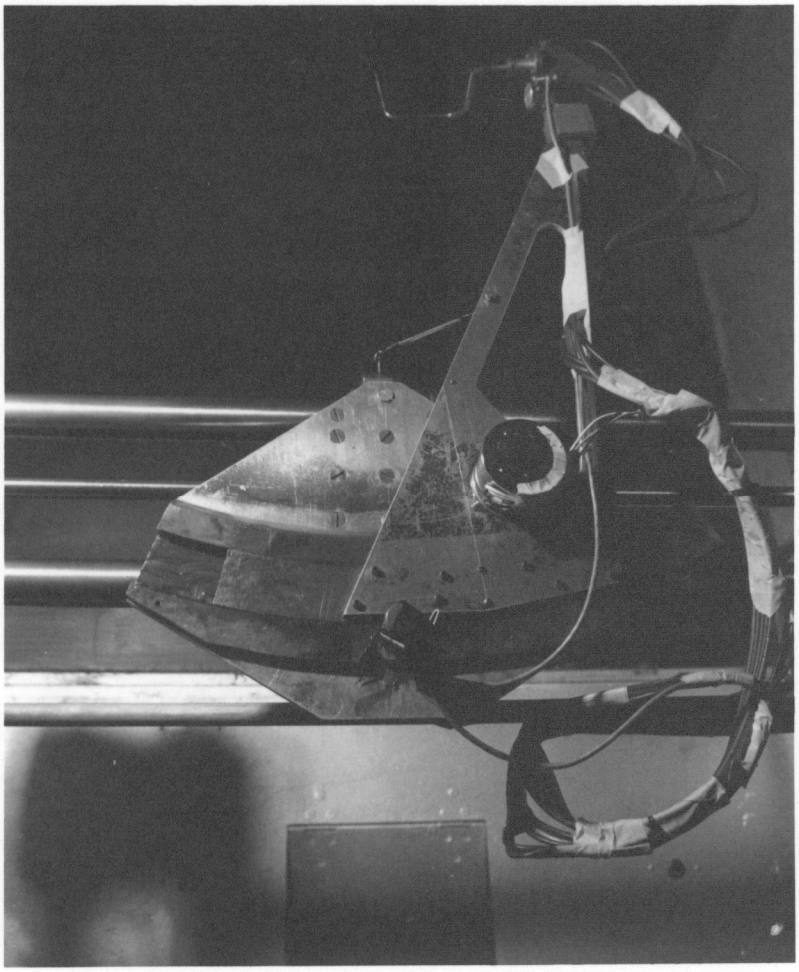

Fig. 10. Adapter Unit.

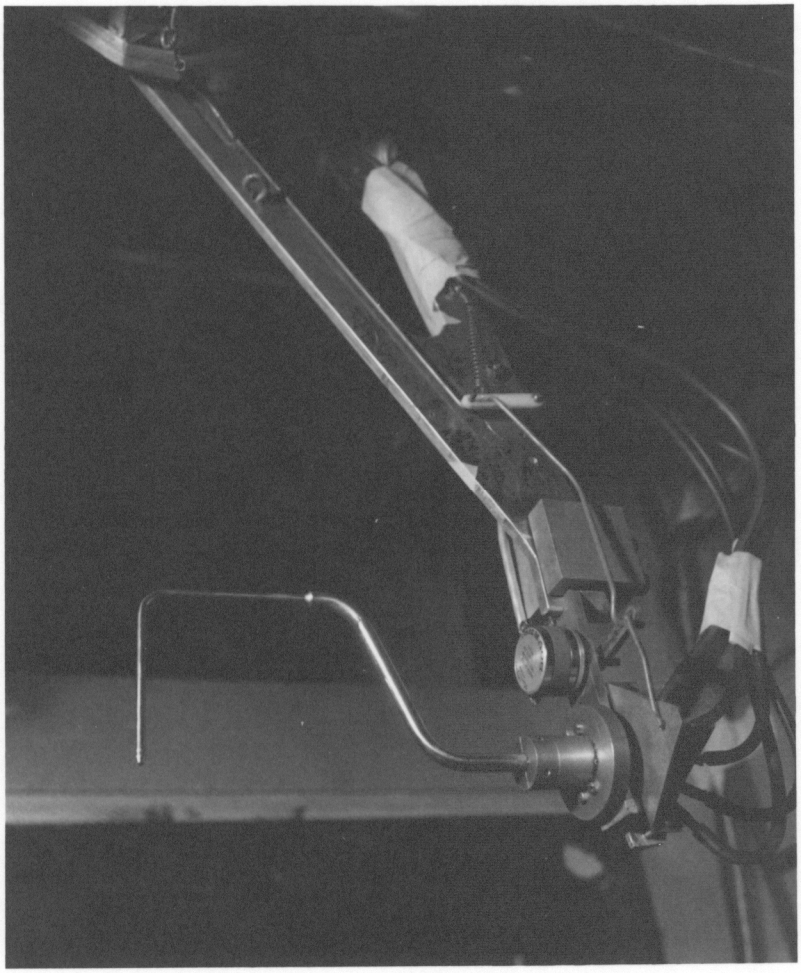

Fig. 11. Details of Probe Mounting.

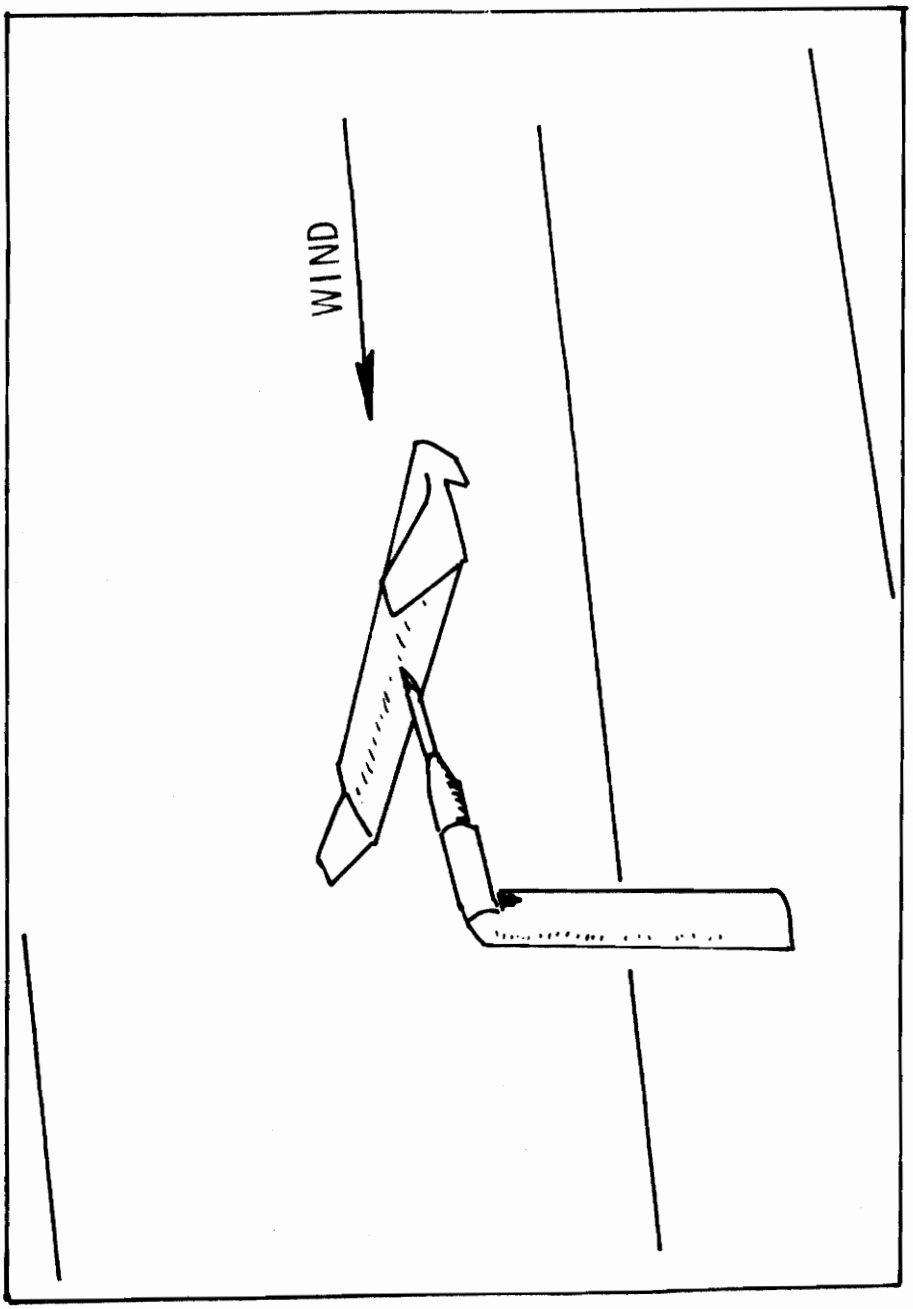

Fig. 12. Wing on Strain Gauge Balance System in Wind Tunnel (Schematic).

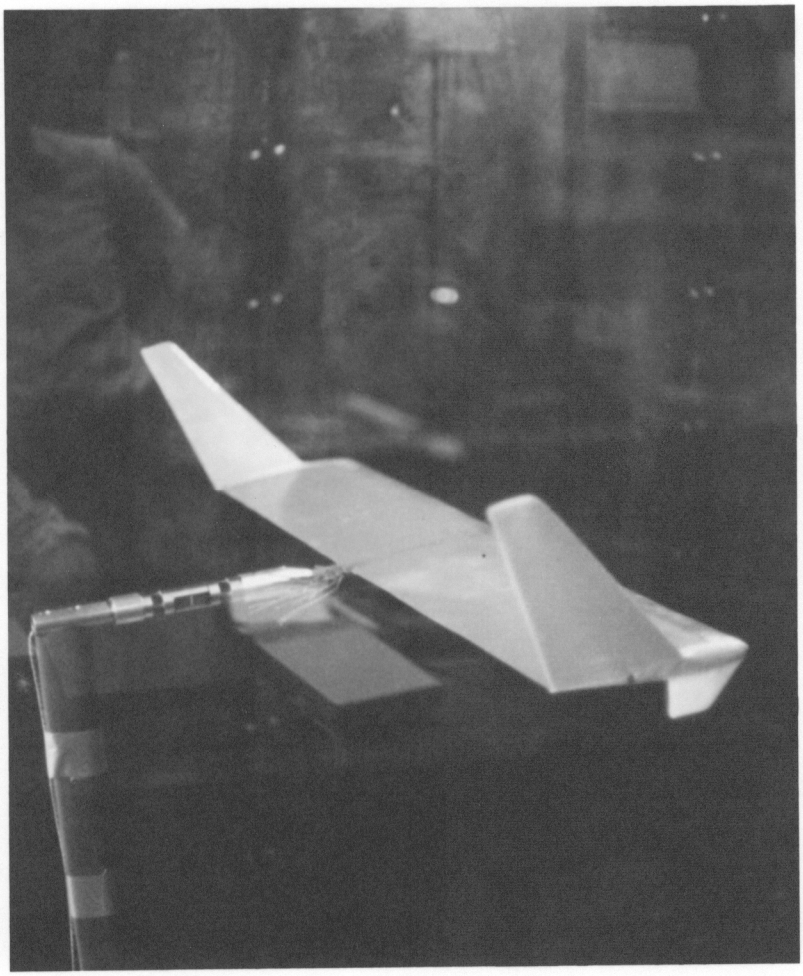

Fig. 13. Wing on Strain Gauge Balance.

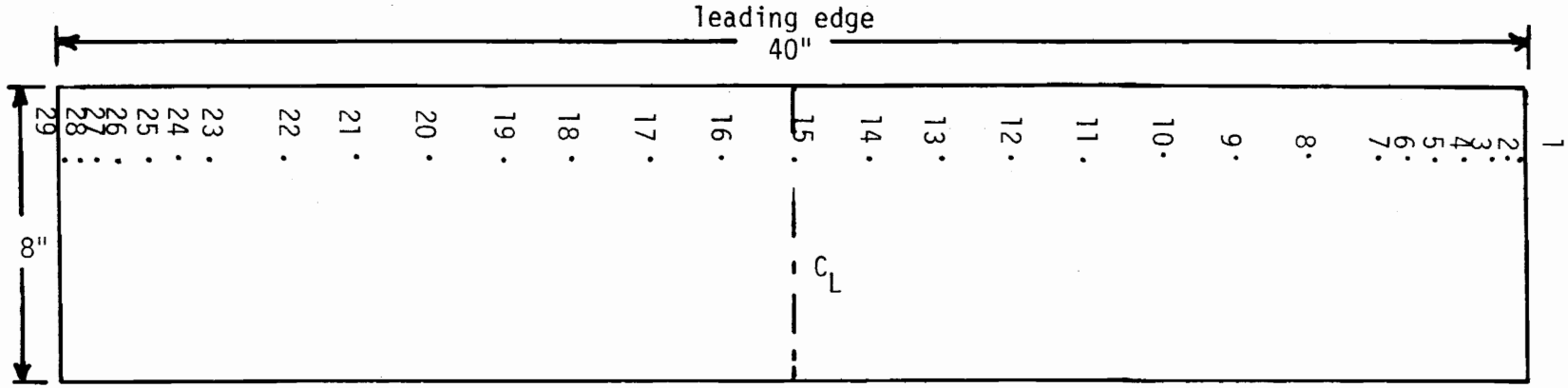

Note: a. 0.39" between taps 1-3 and 27-29
b. 0.78" between taps 3-7 and 23-27
c. 2" between taps 7-23
d. Pressure tap 15 is on wing centerline

Fig. 14. Wing Pressure Taps (AR = 5).

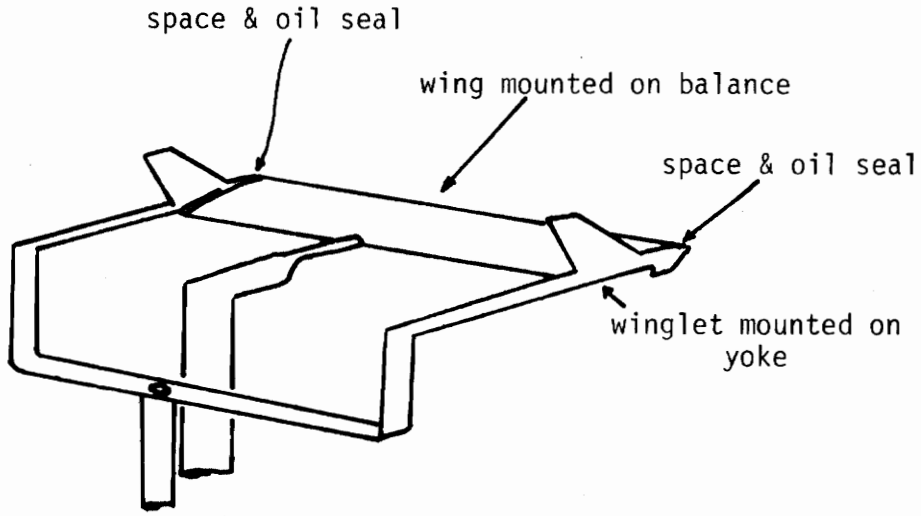

a. Wing on Balance with Winglets Adjacent

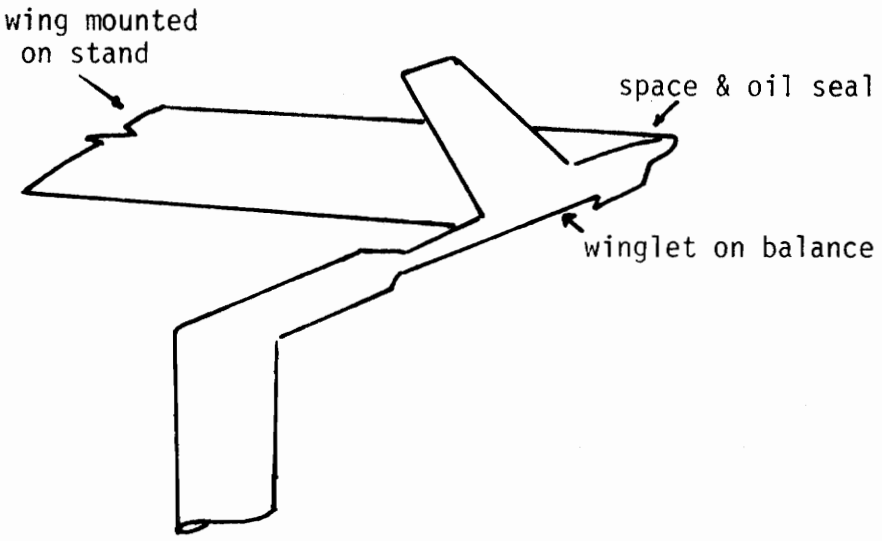

b. Winglet on Balance with Wing Adjacent

Fig. 15. Winglet Yoke Set-Ups.

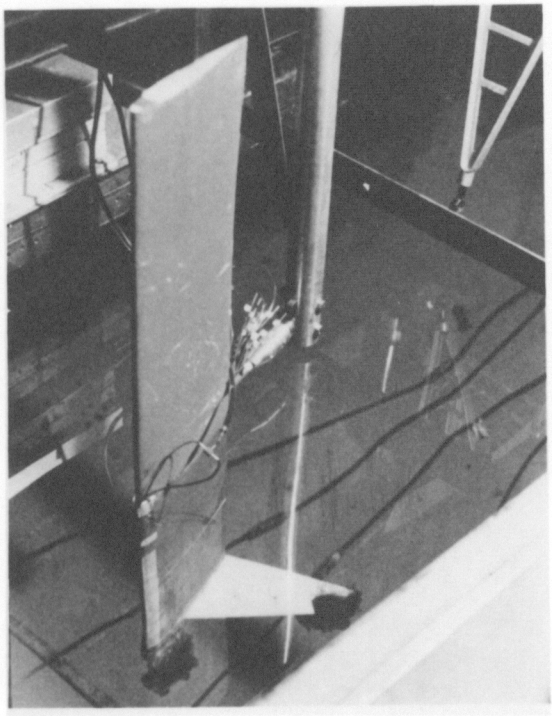

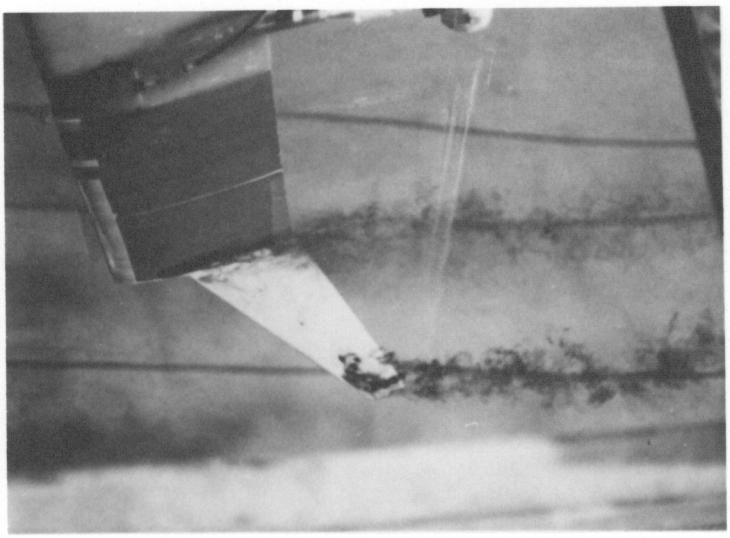

Fig. 16. Wing in Towing Tank.

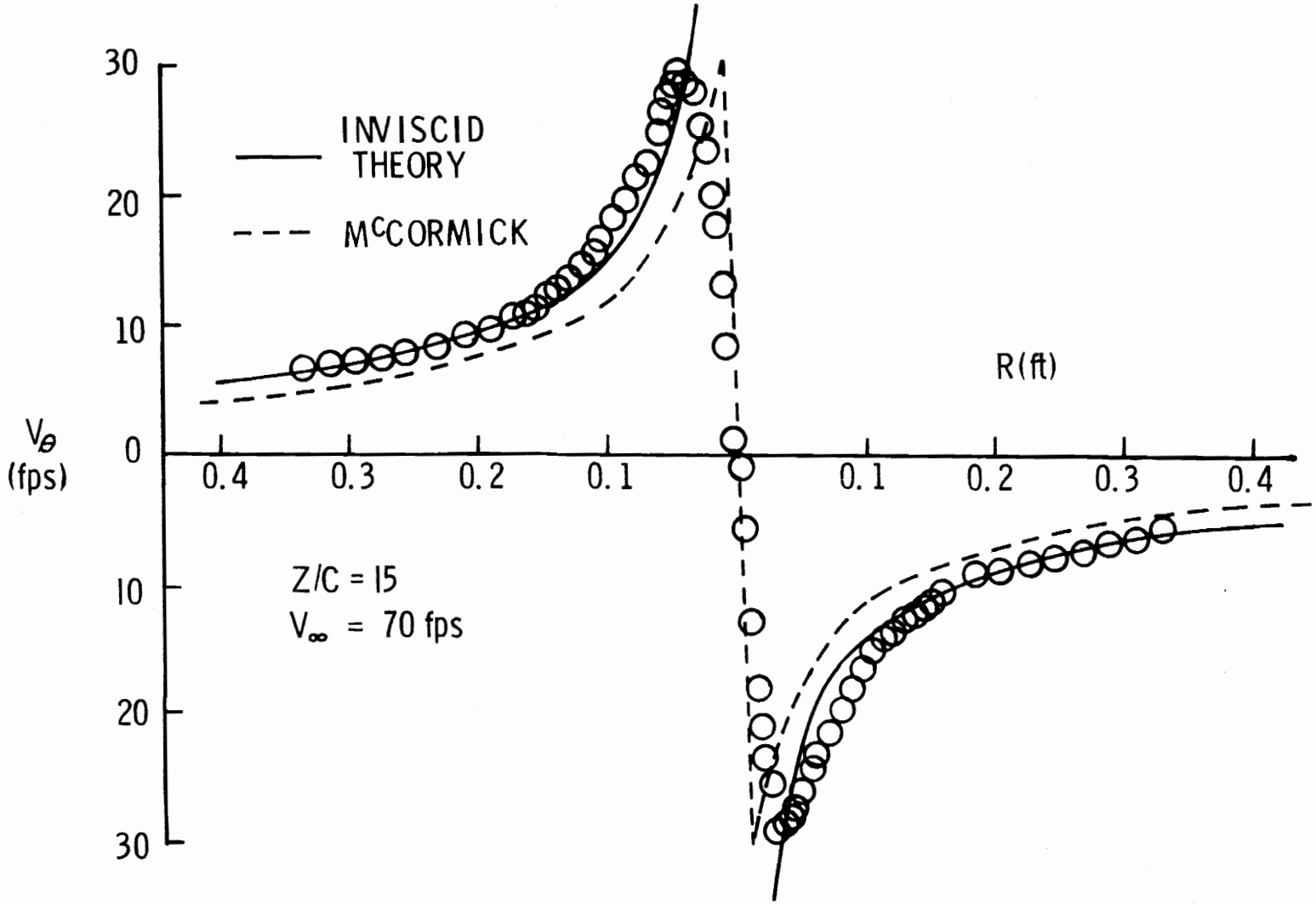

Fig. 17. Experimental Vs. Theoretical Tangential Velocity Profile.

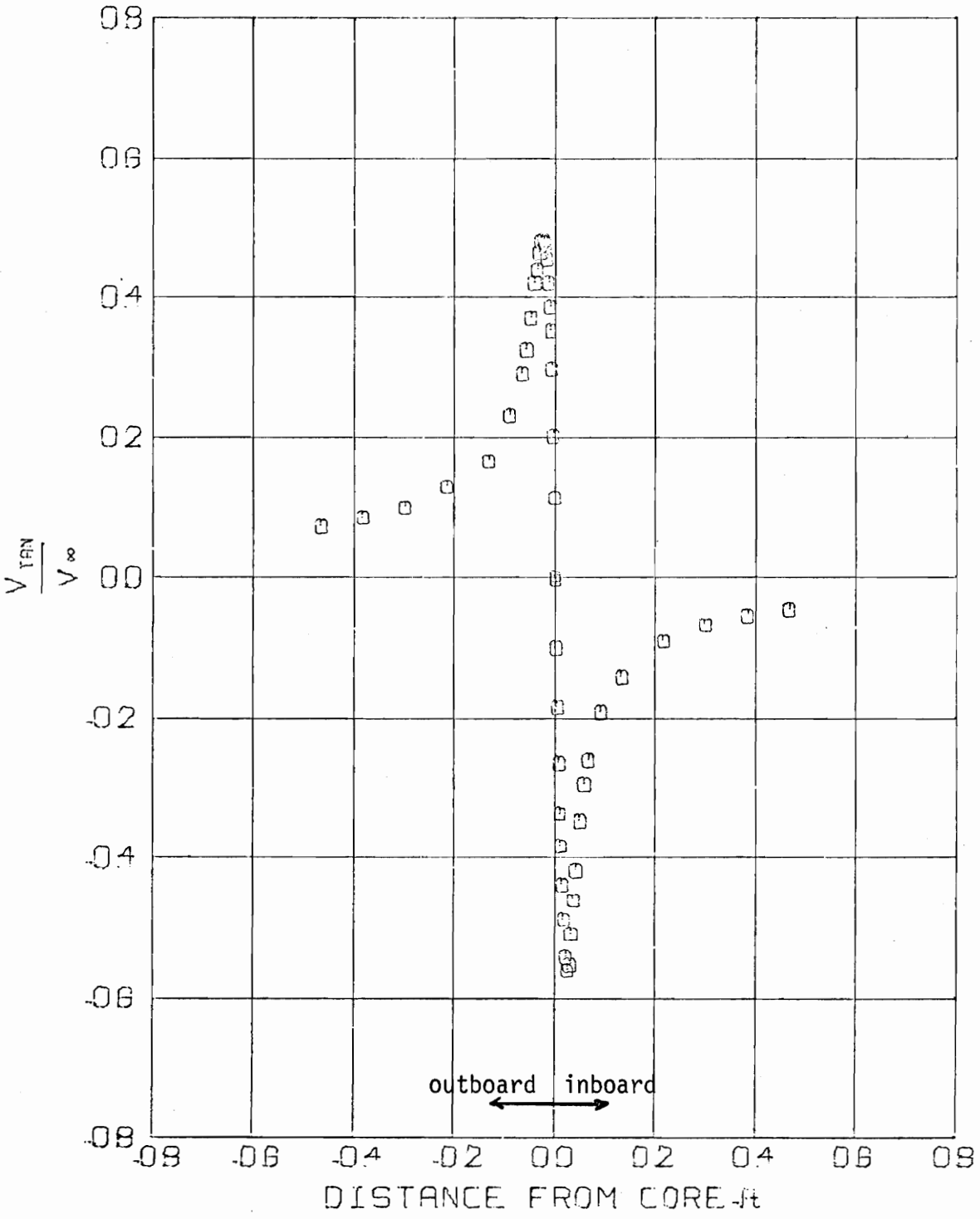

Fig. 18. Tangential Velocity Profile, Square Tip.
V_∞ = 103.4 fps Z/C = 5

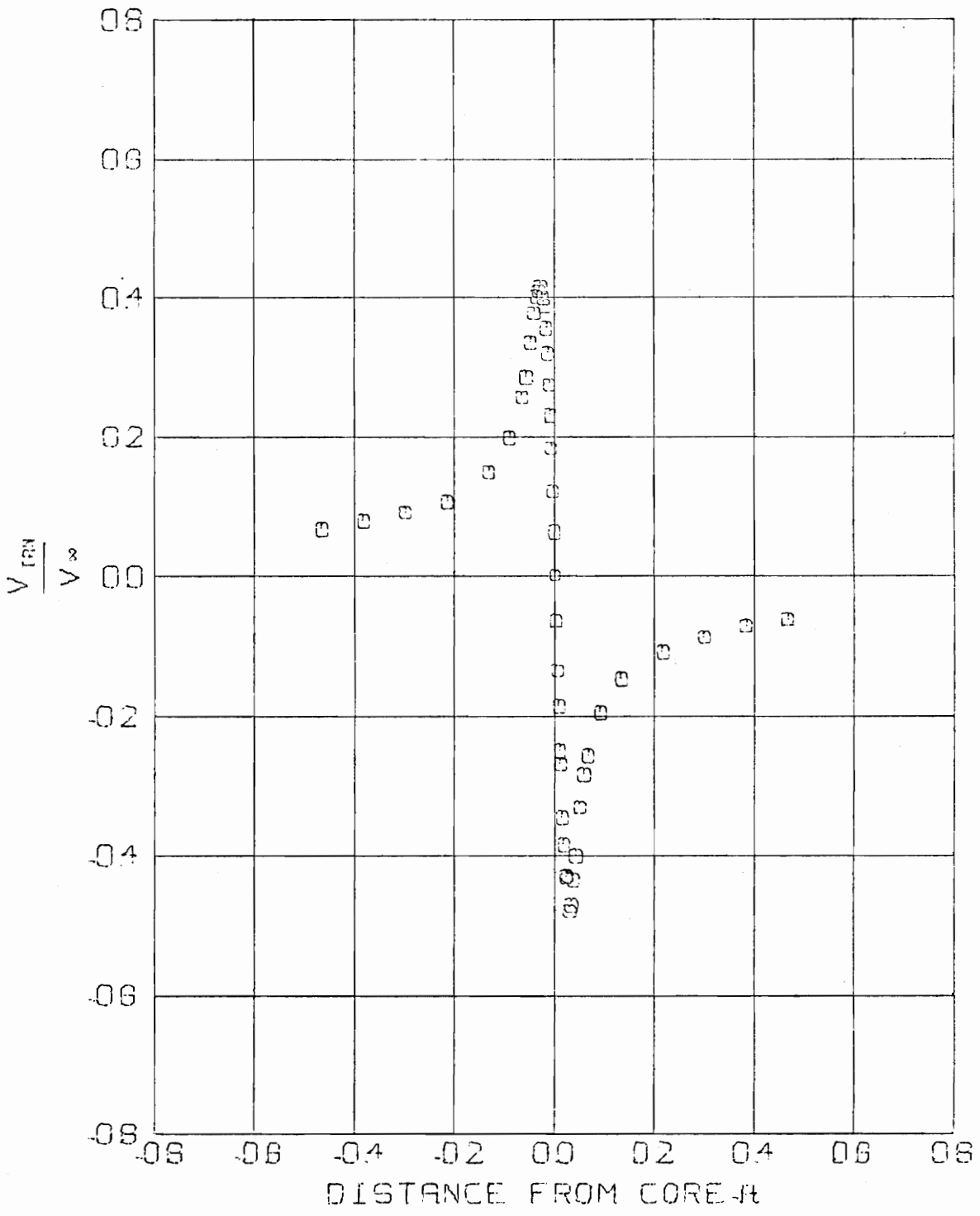

Fig. 19. Tangential Velocity Profile, Square Tip.
V_∞ = 102.9 fps Z/C = 20

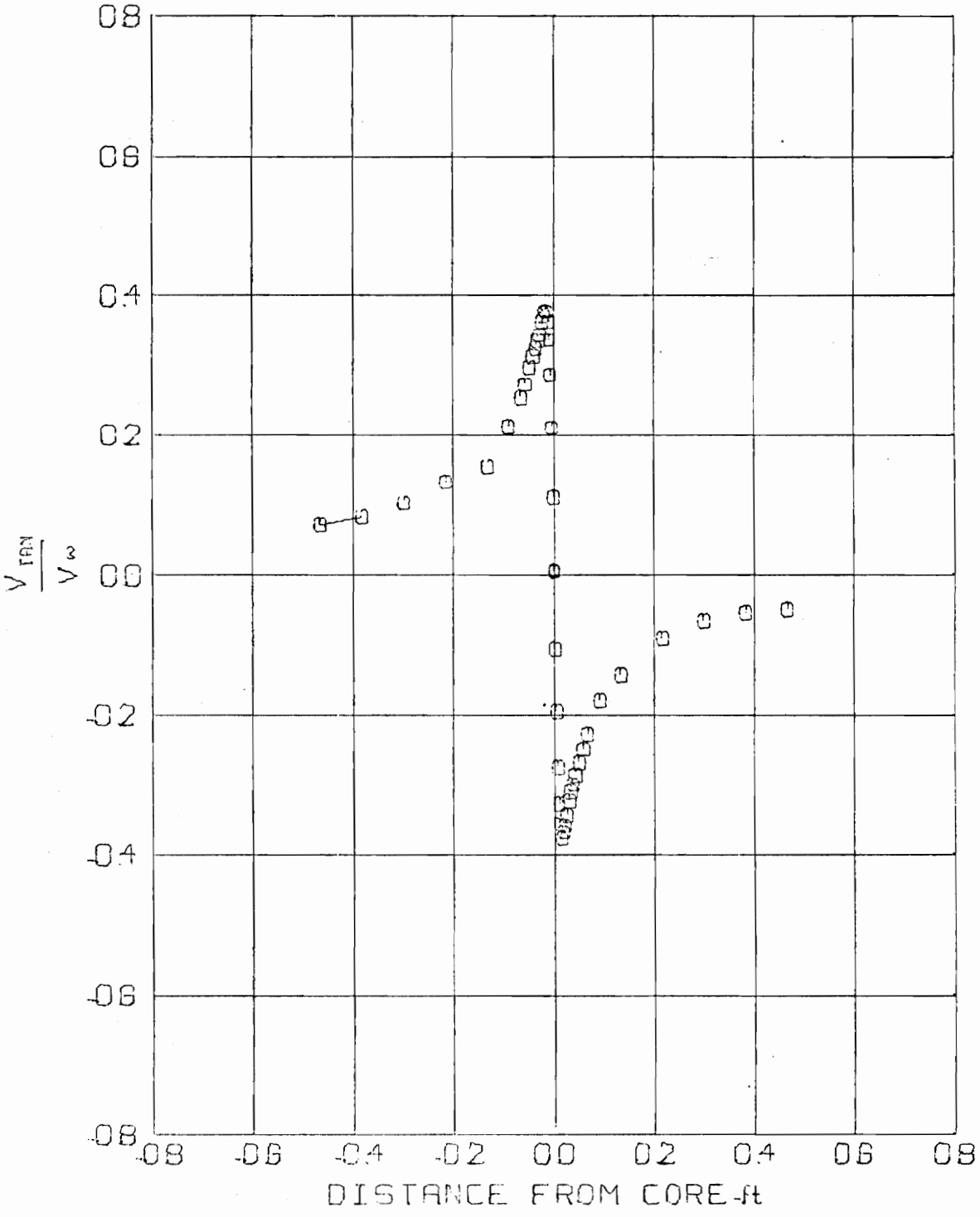

Fig. 20. Tangential Velocity Profile, Pointed Tip
V_∞ = 102.5 fps Z/C = 5

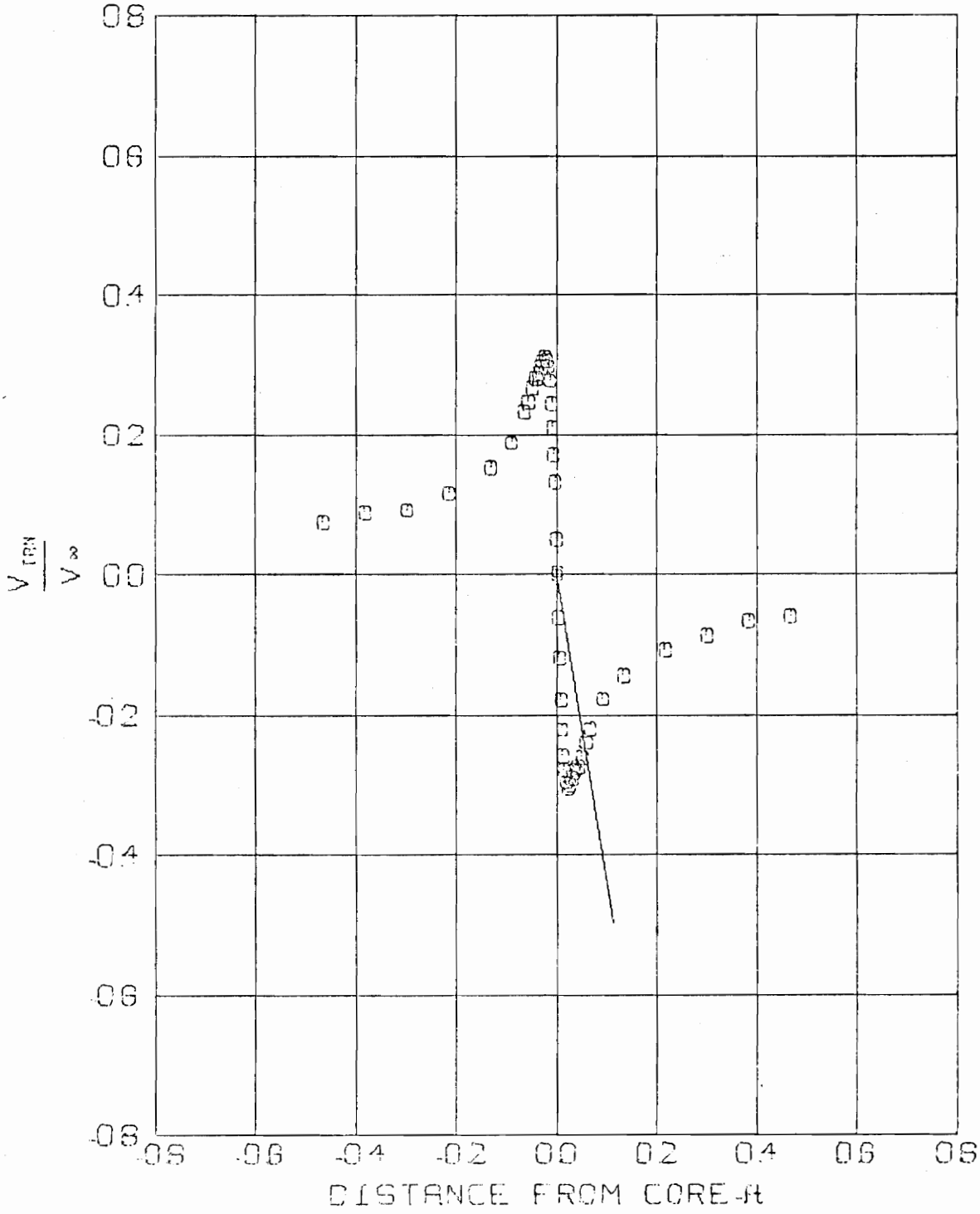

Fig. 21. Tangential Velocity Profile, Pointed Tip.
V_∞ = 104.4 fps Z/C = 20

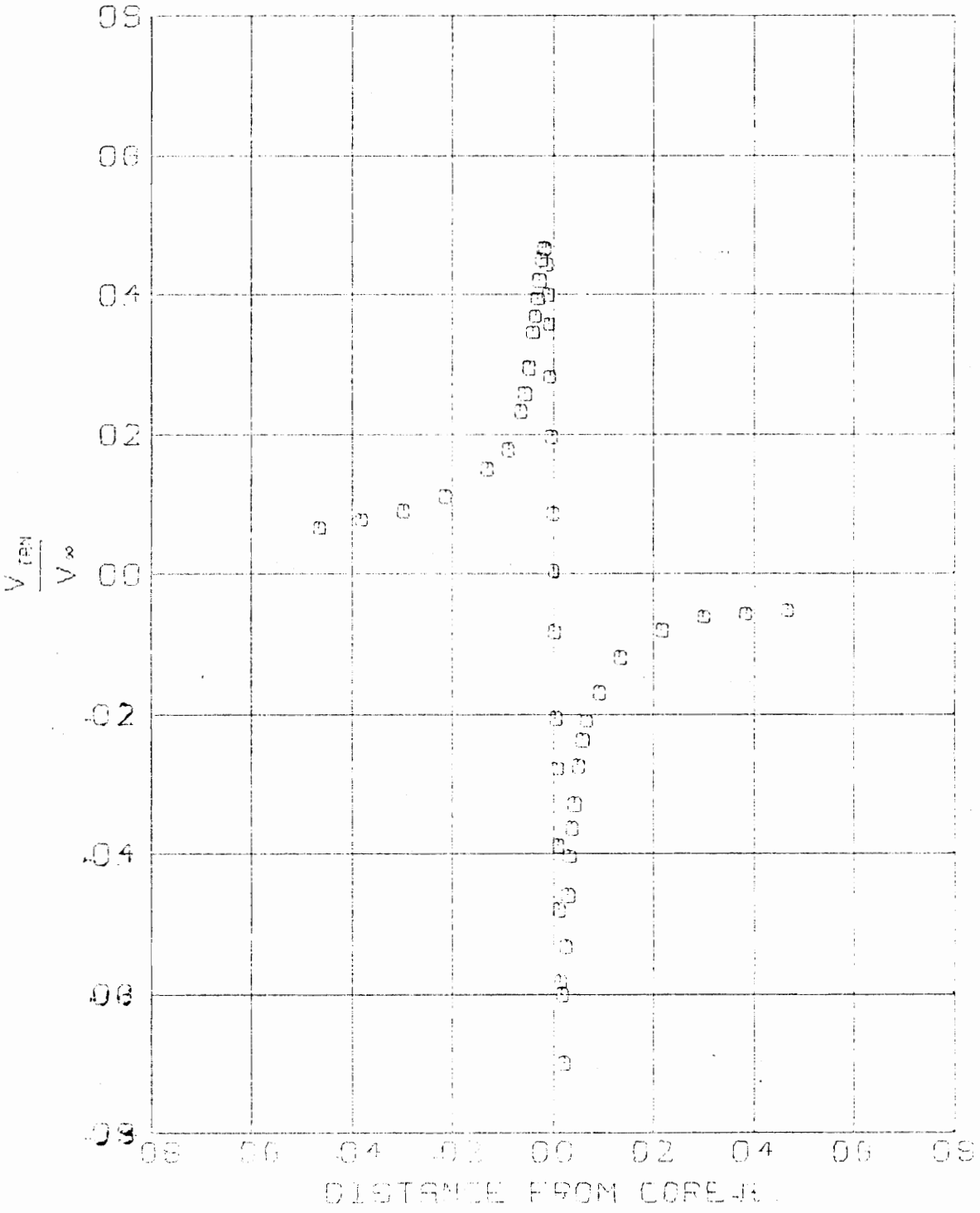

Fig. 22. Tangential Velocity Profile, Round Tip/Winglet Base.
V_∞ = 104.1 fps Z/C = 5

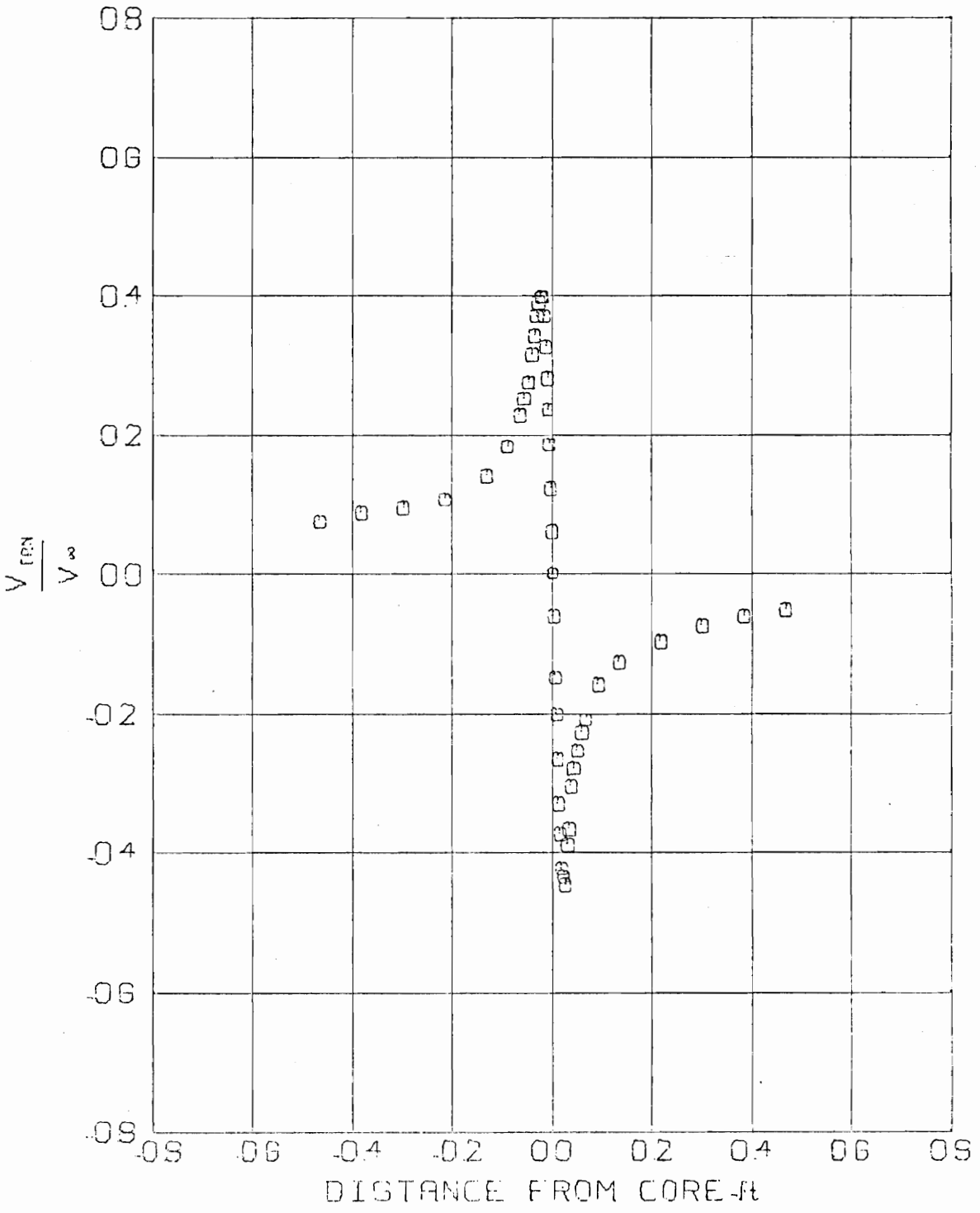

Fig. 23. Tangential Velocity Profile, Round Tip/Winglet Base.
V_∞ = 105.0 fps Z/C = 20

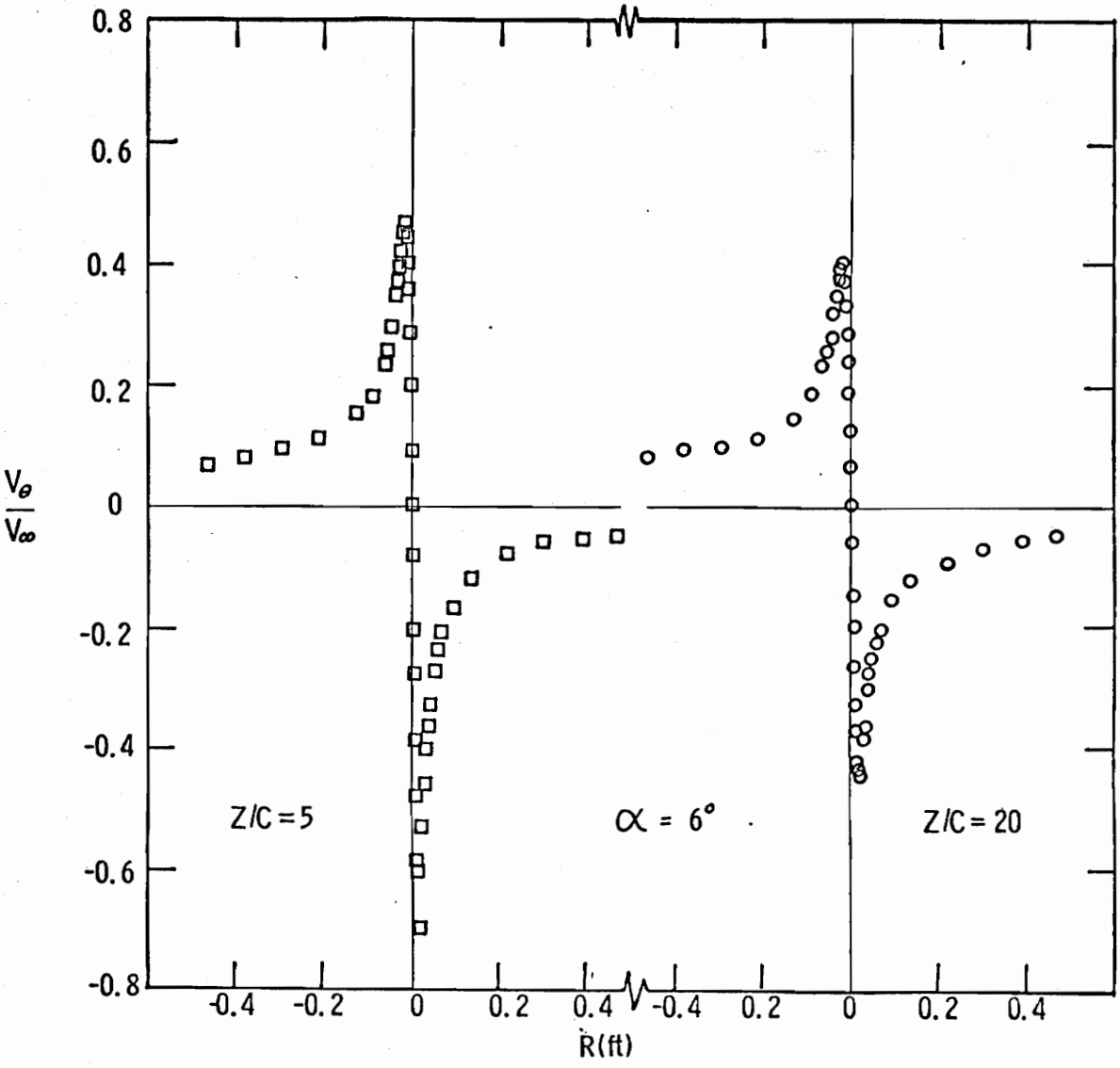

Fig. 24. Vortex Tangential Velocity Decay, Round Tip/Winglet Base.

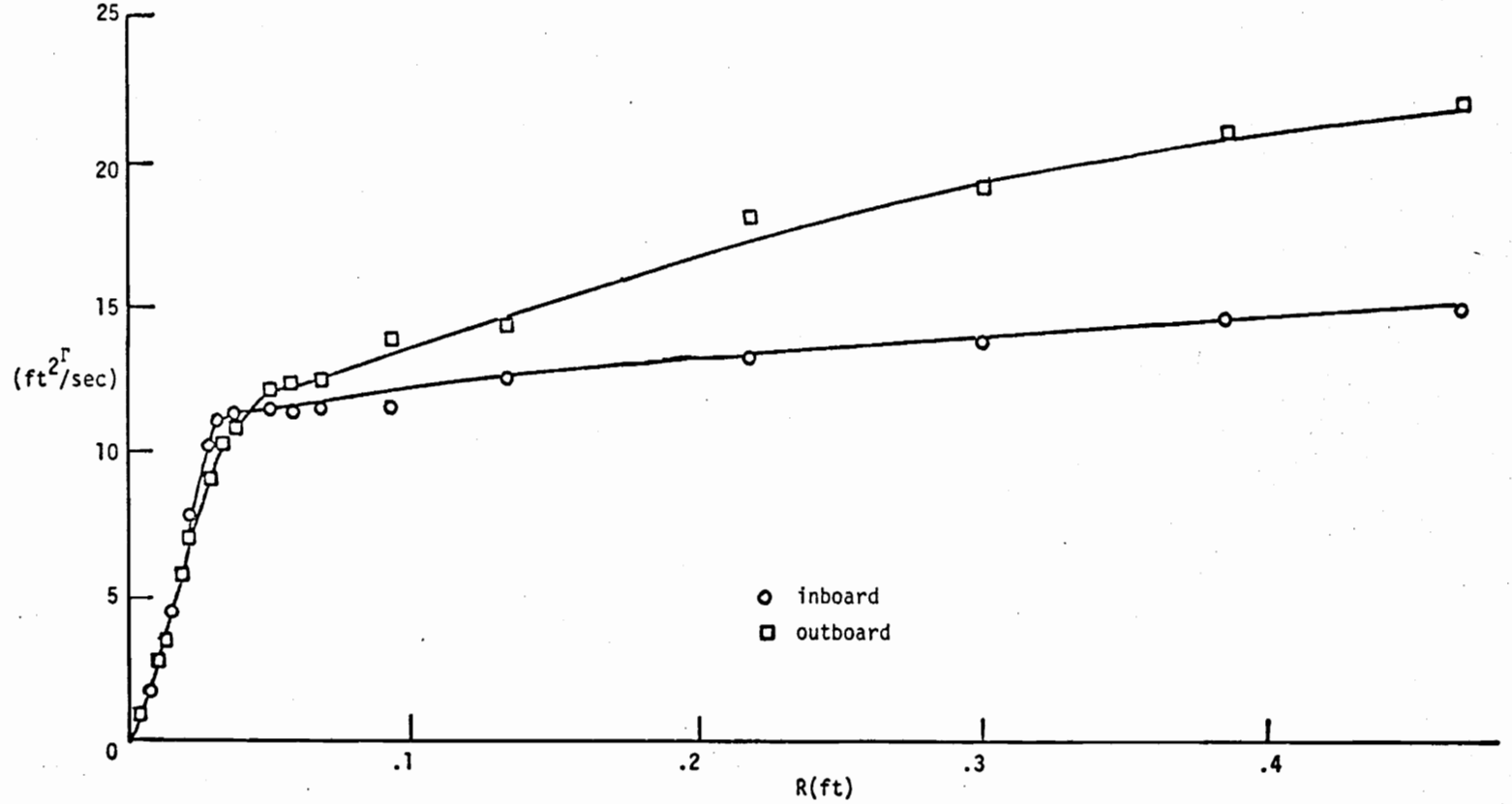

Fig. 25. Radial Circulation Distribution (Z/C = 5).

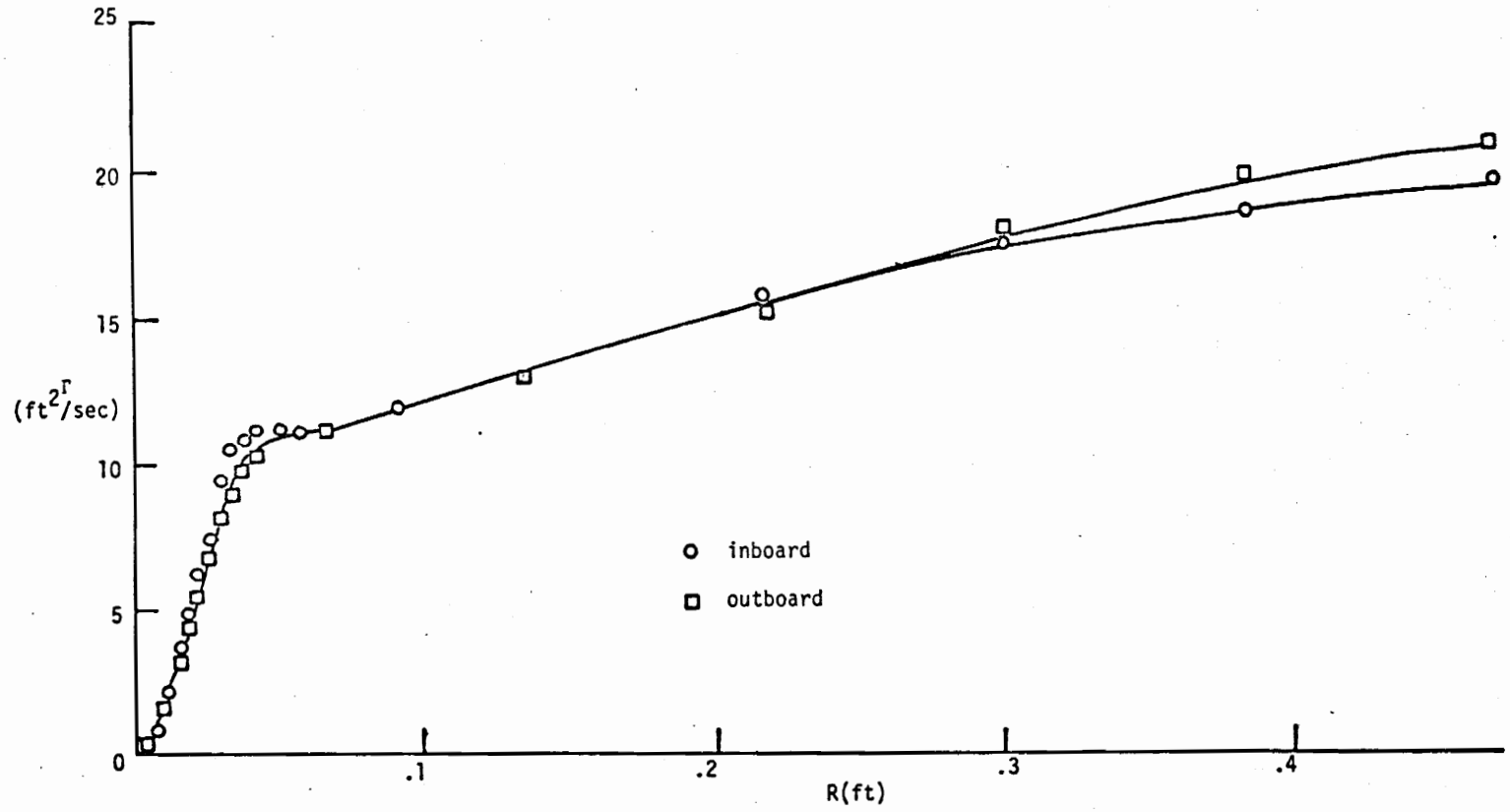

Fig. 26. Radial Circulation Distribution (Z/C = 20).

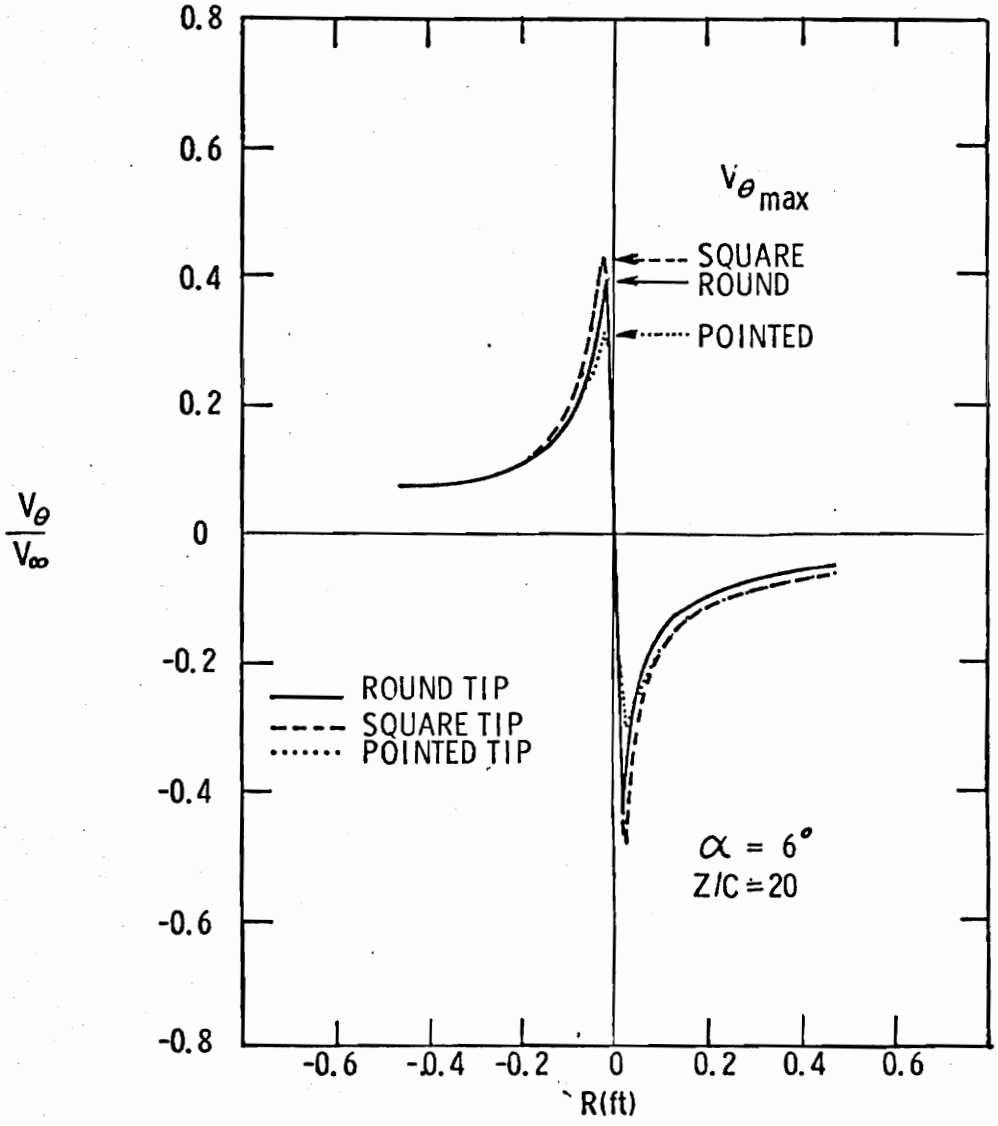

Fig. 27. Tangential Velocity Comparison.

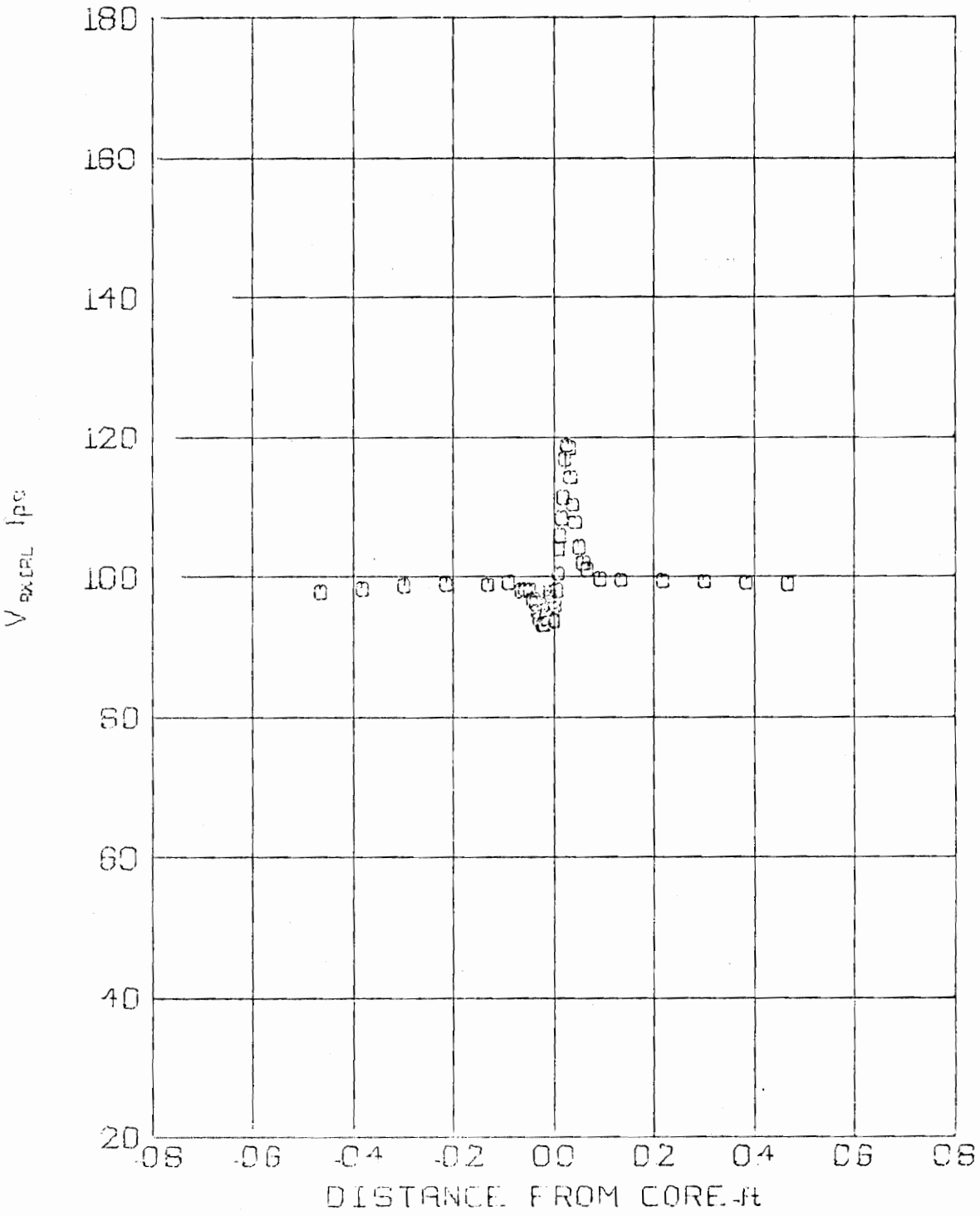

Fig. 28. Axial Velocity Profile, Square Tip.
V_∞ = 103.4 fps Z/C = 5

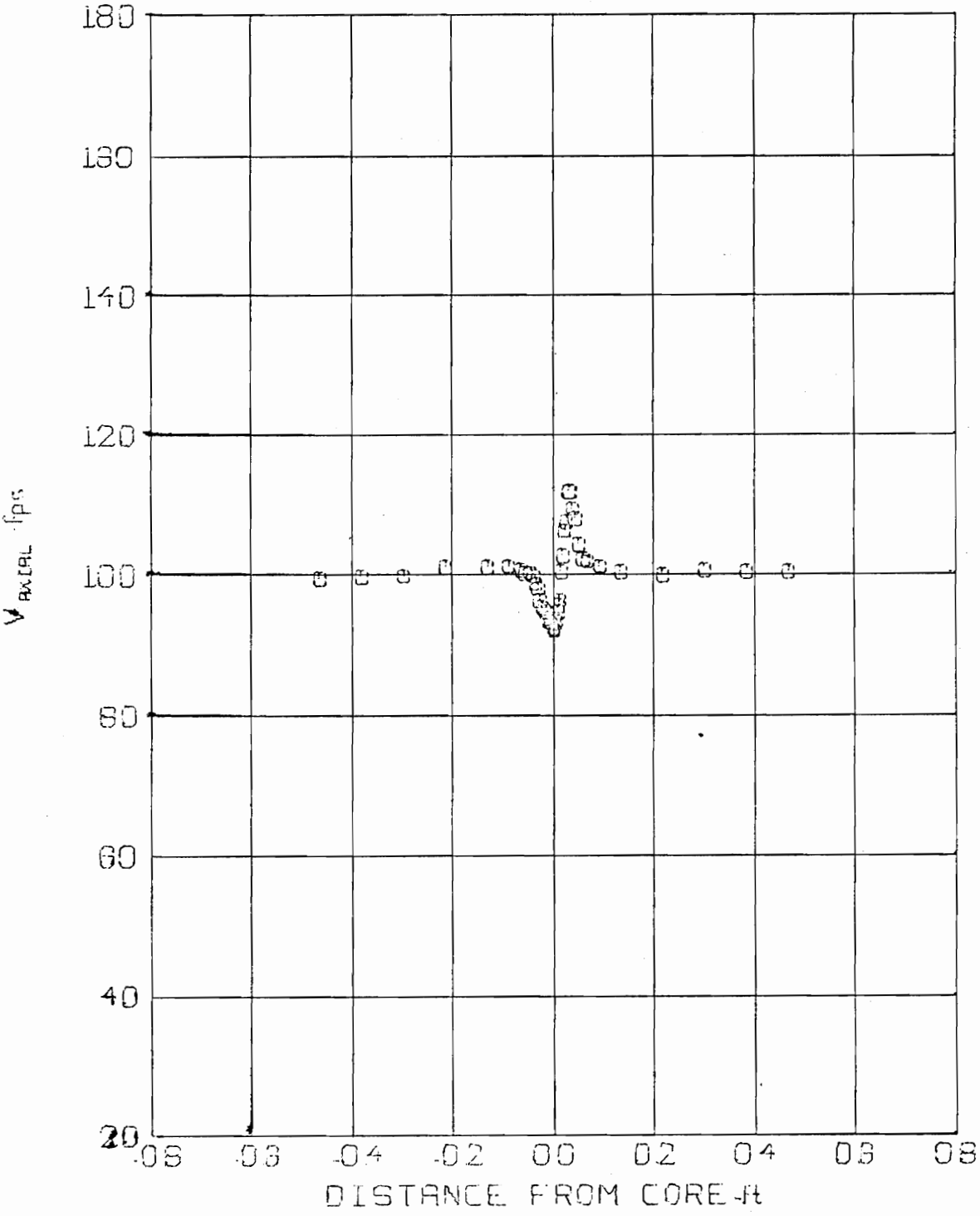

Fig. 29. Axial Velocity Profile, Square Tip.
V_∞ = 102.9 fps Z/C = 20

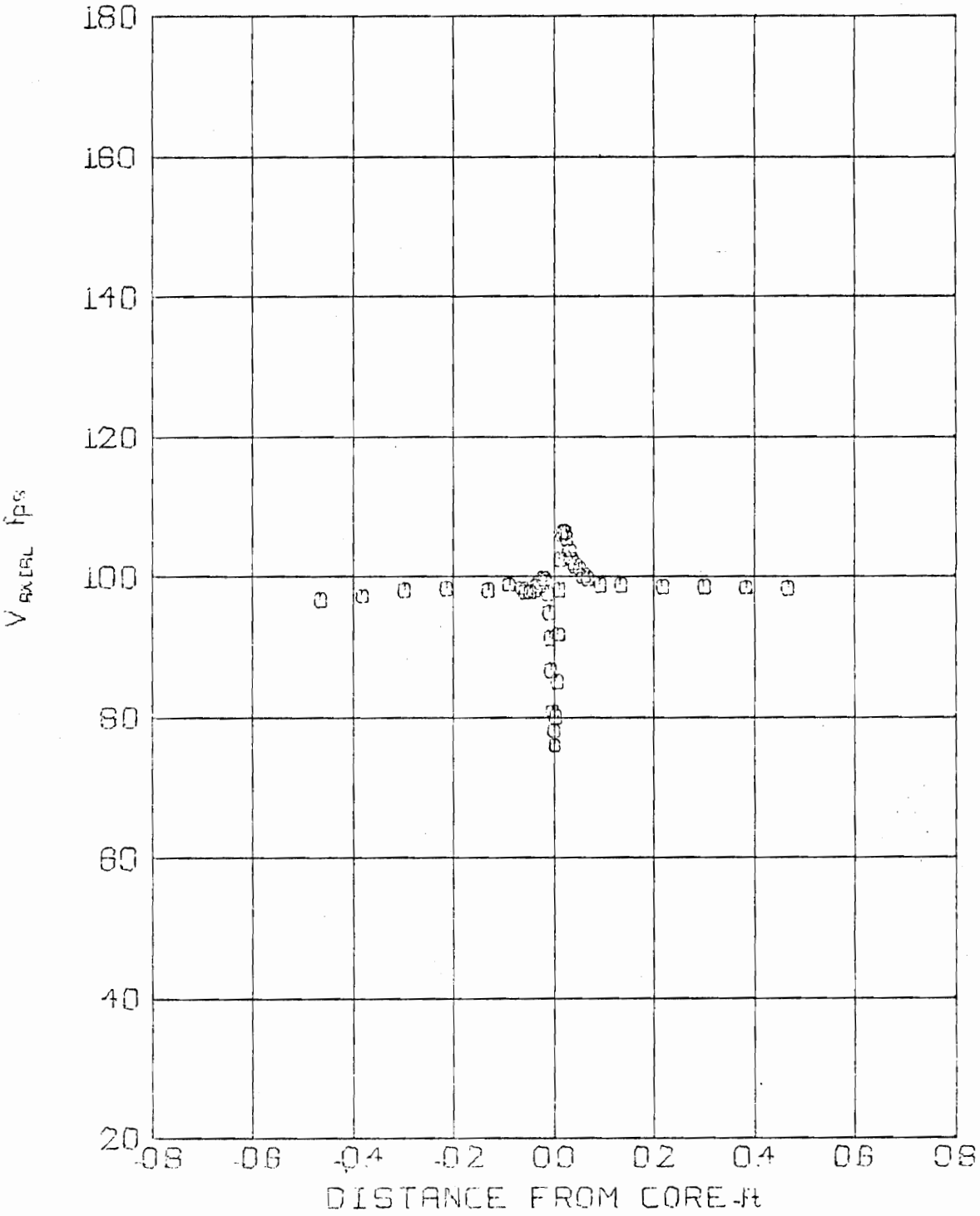

Fig. 30. Axial Velocity Profile, Pointed Tip.
V_∞ = 102.5 fps Z/C = 5

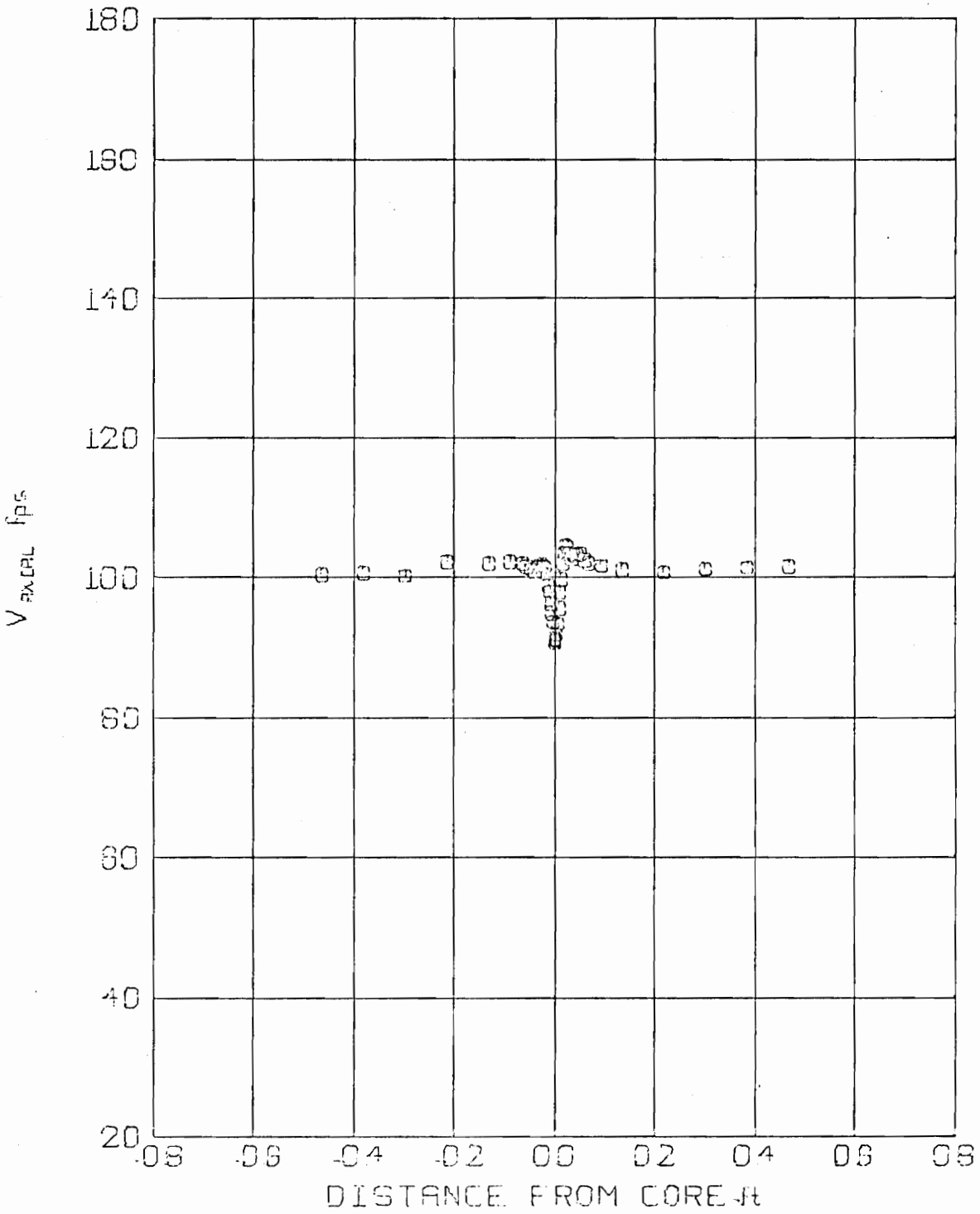

Fig. 31. Axial Velocity Profile, Pointed Tip.
V_∞ = 104.4 fps Z/C = 20

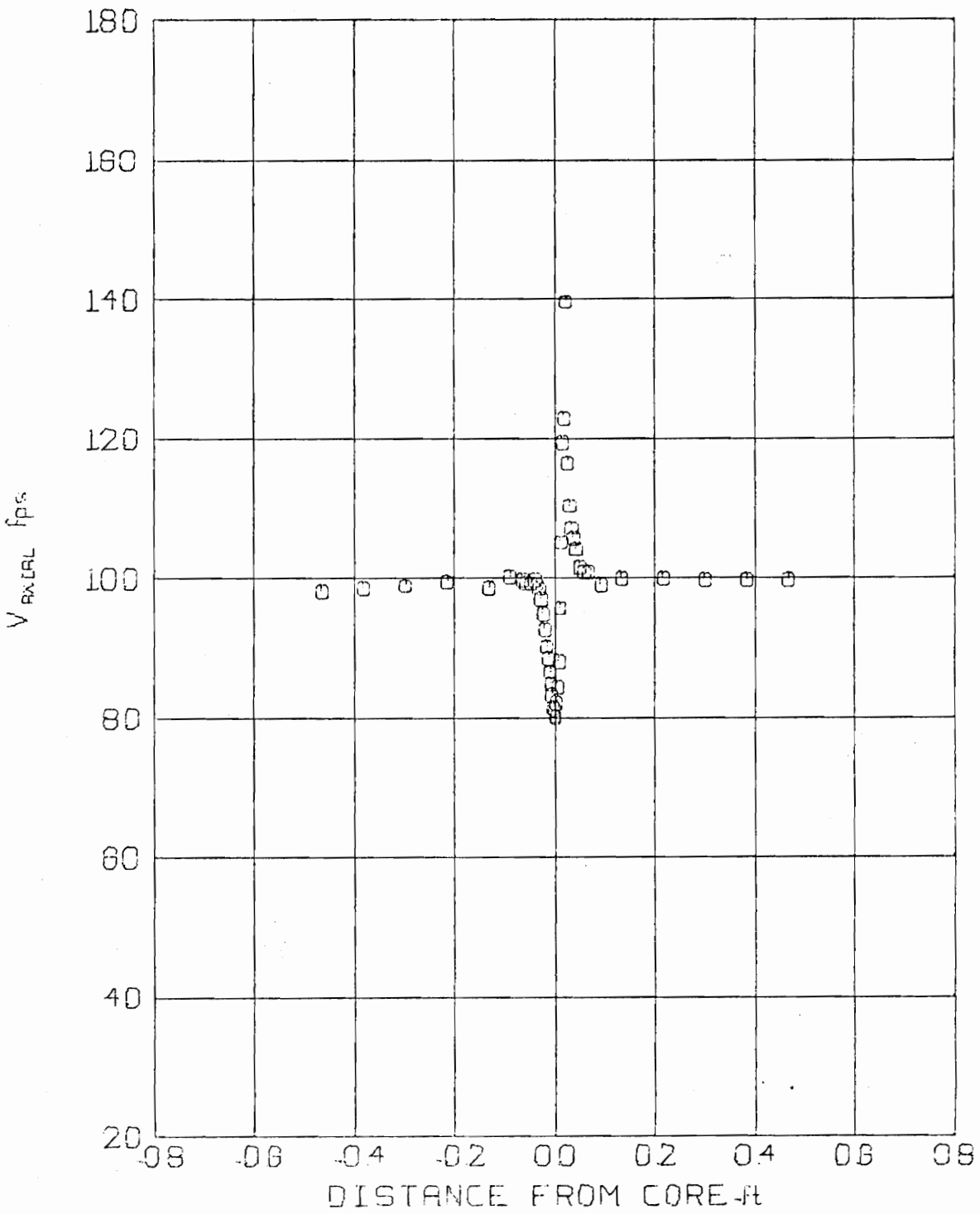

Fig. 32. Axial Velocity Profile, Round Tip/Winglet Base.
V_∞ = 104.1 fps Z/C = 5

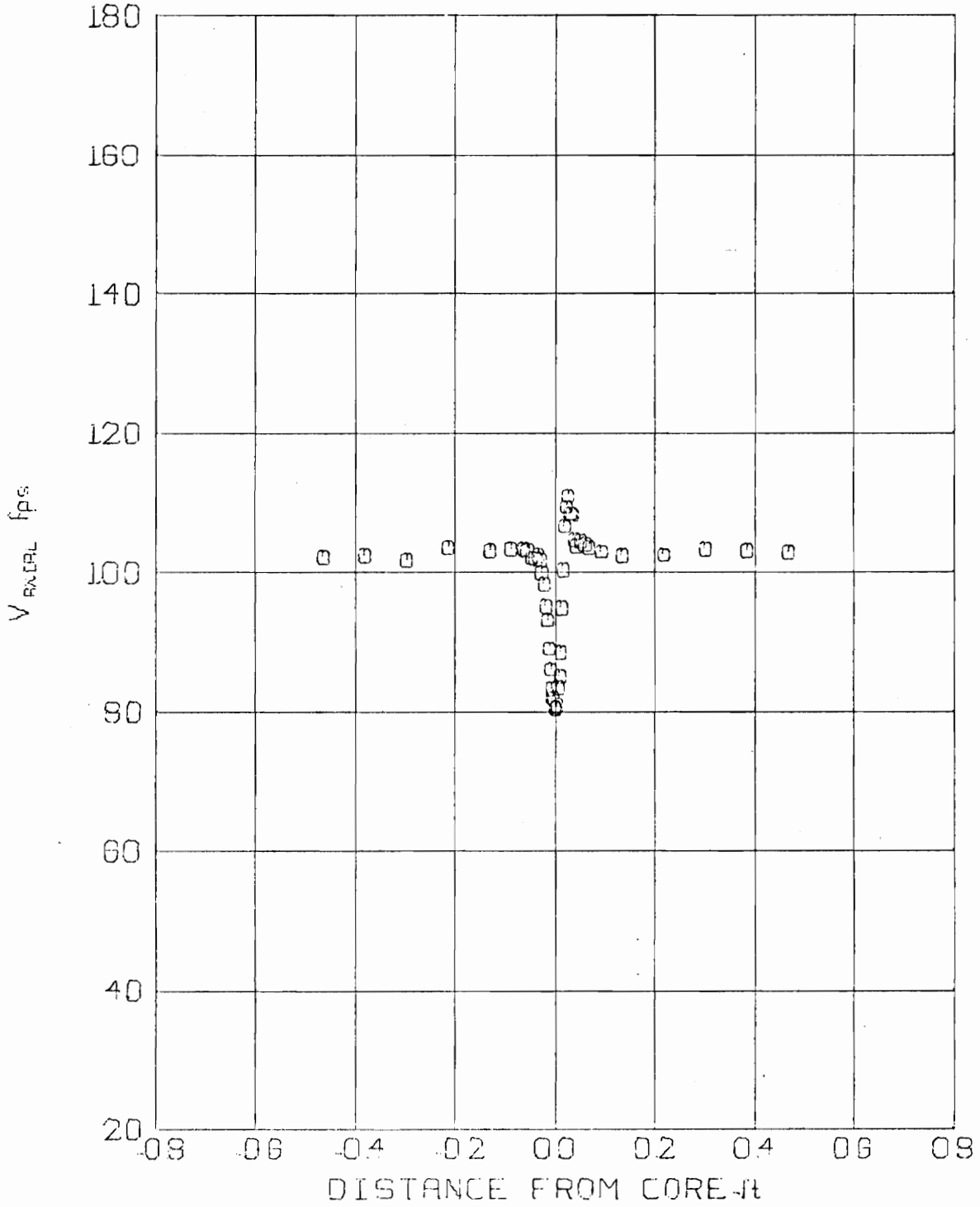

Fig. 33. Axial Velocity Profile, Round Tip/Winglet Base.
V_∞ = 105.0 fps Z/C = 20

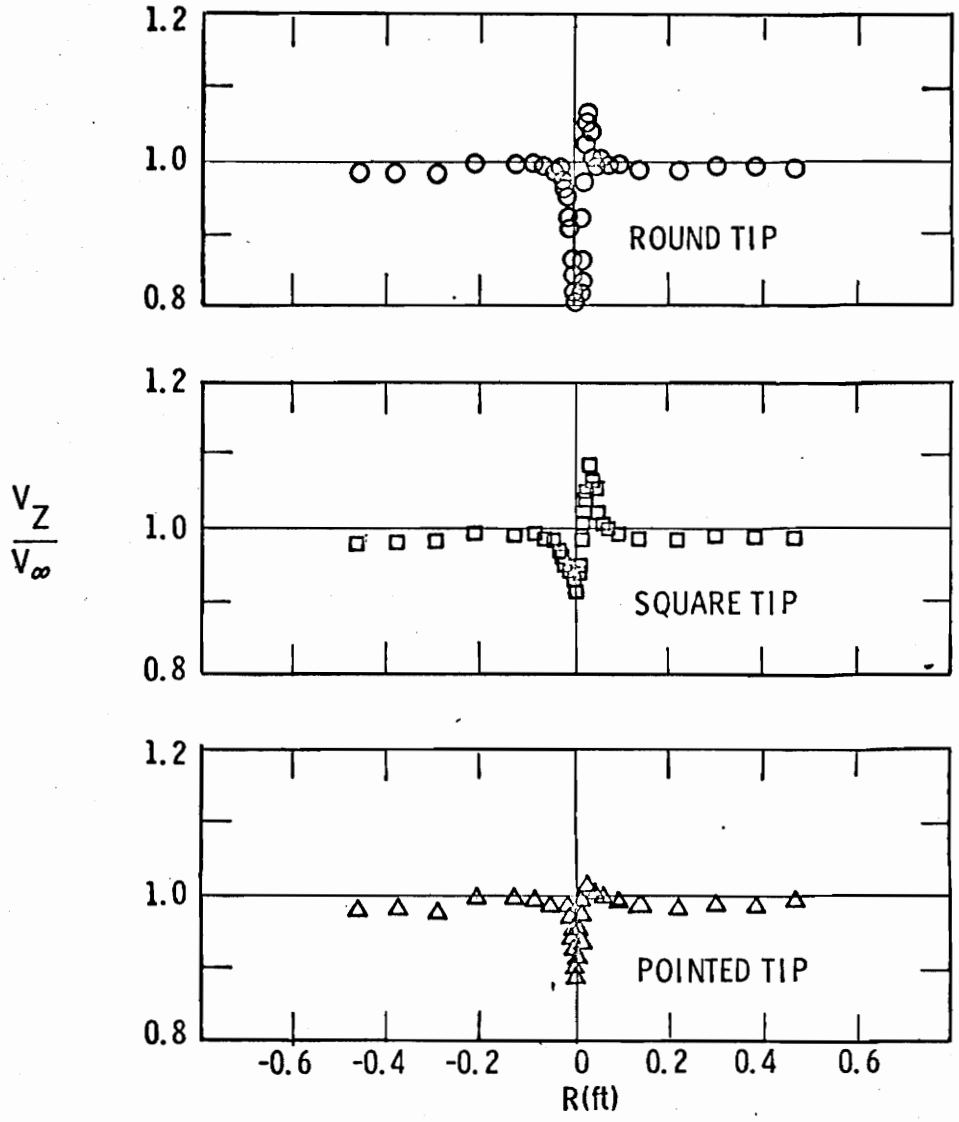

Fig. 34. Comparison of Axial Velocity Profiles (Z/C = 20).

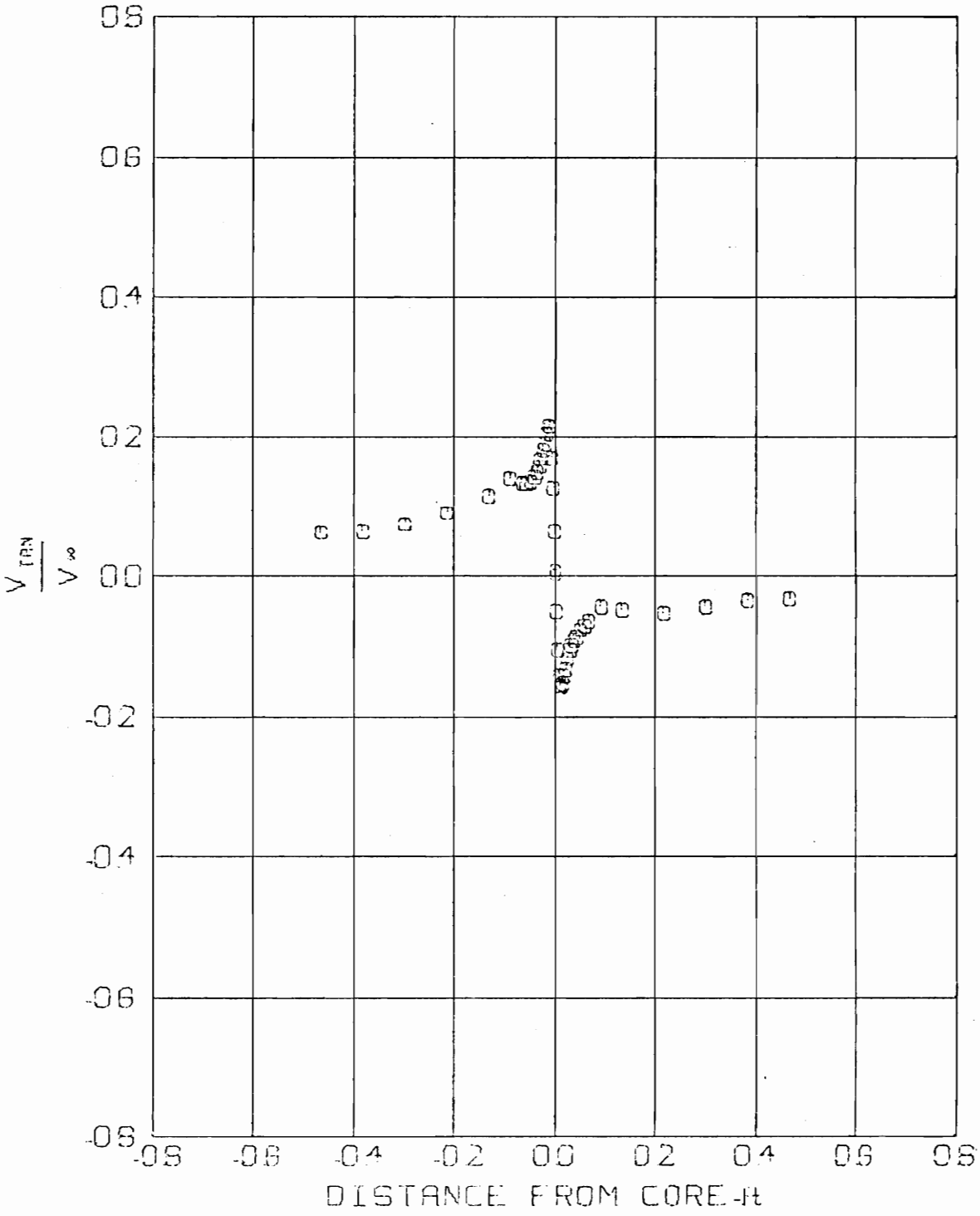

Fig. 35. Tangential Velocity Profile, Winglet Vortex 1.
V_∞ = 103.7 fps Z/C = 5

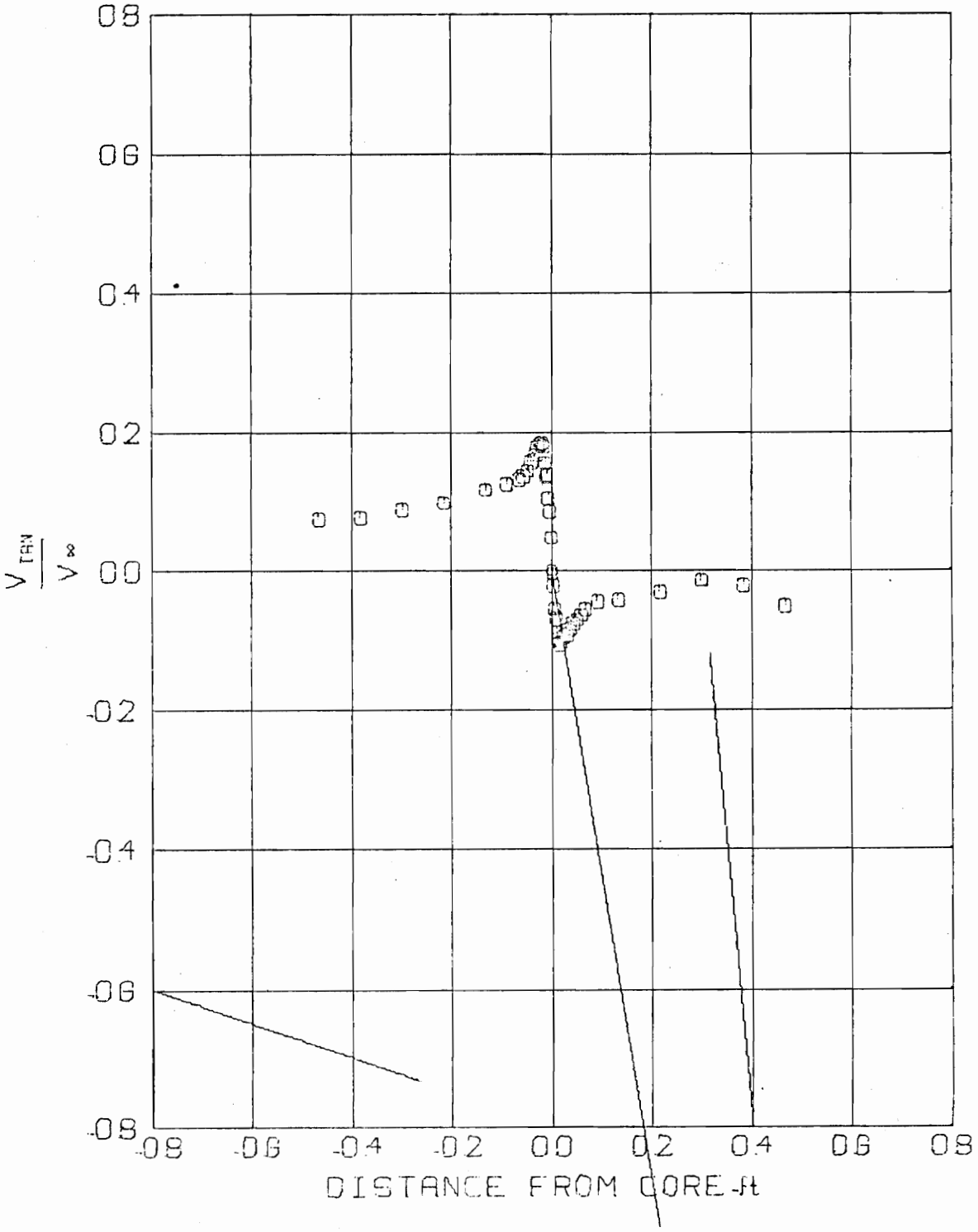

Fig. 36. Tangential Velocity Profile, Winglet Vortex 1.
V_∞ = 105.1 fps Z/C = 20

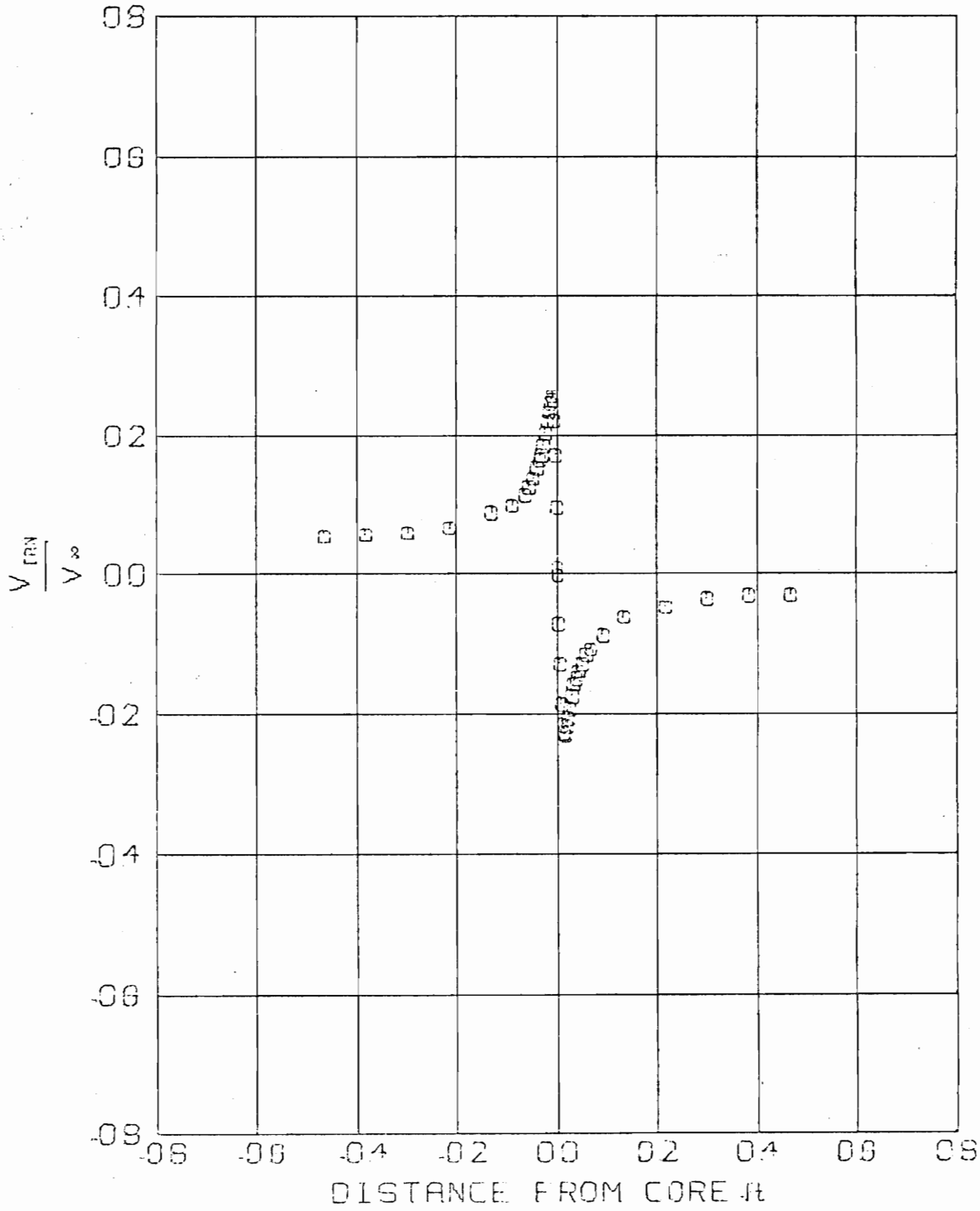

Fig. 37. Tangential Velocity Profile, Winglet Vortex 2.
V_∞ = 105.0 fps Z/C = 5

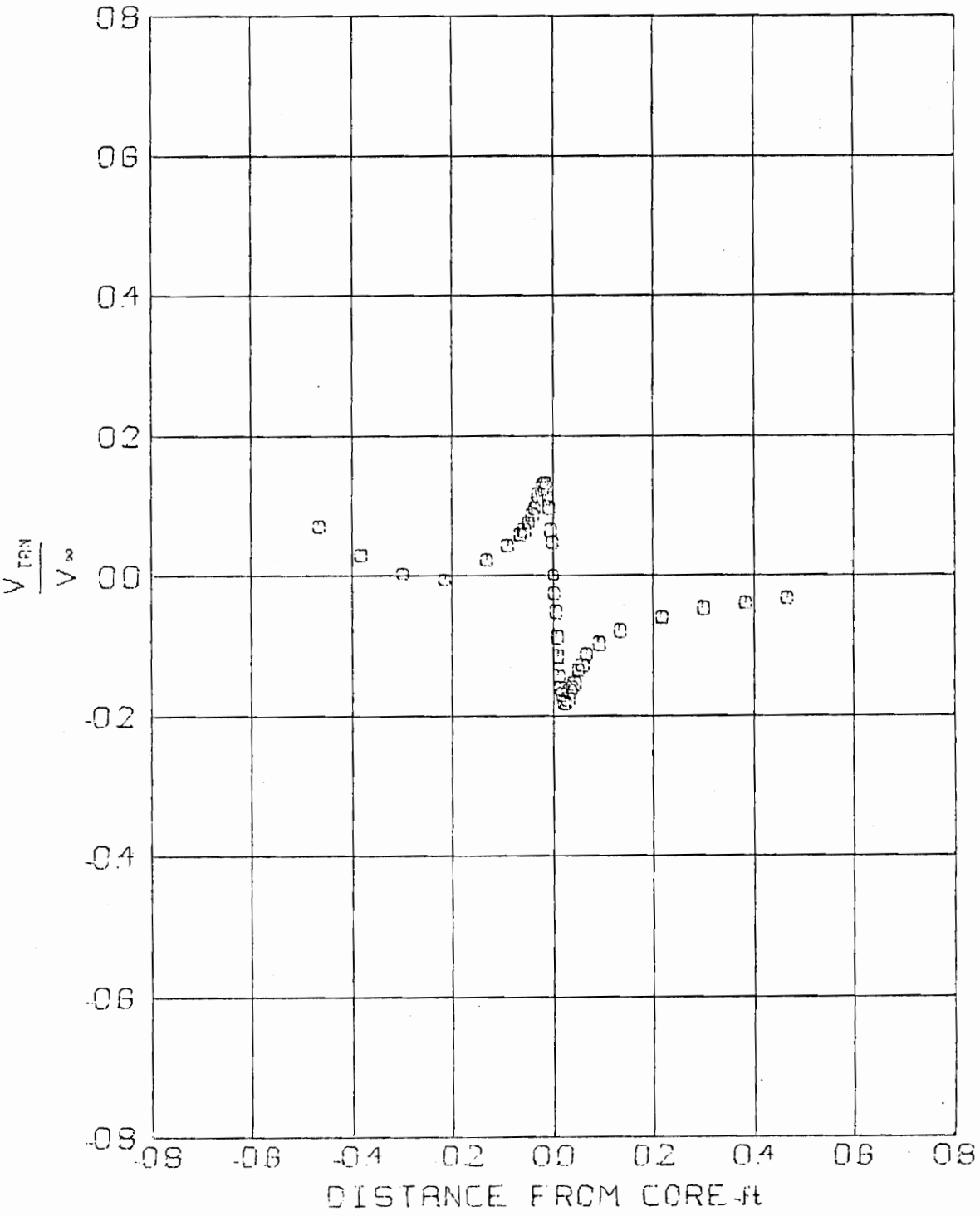

Fig. 38. Tangential Velocity Profile, Winglet Vortex 2.
V_∞ = 103.7 fps Z/C = 20

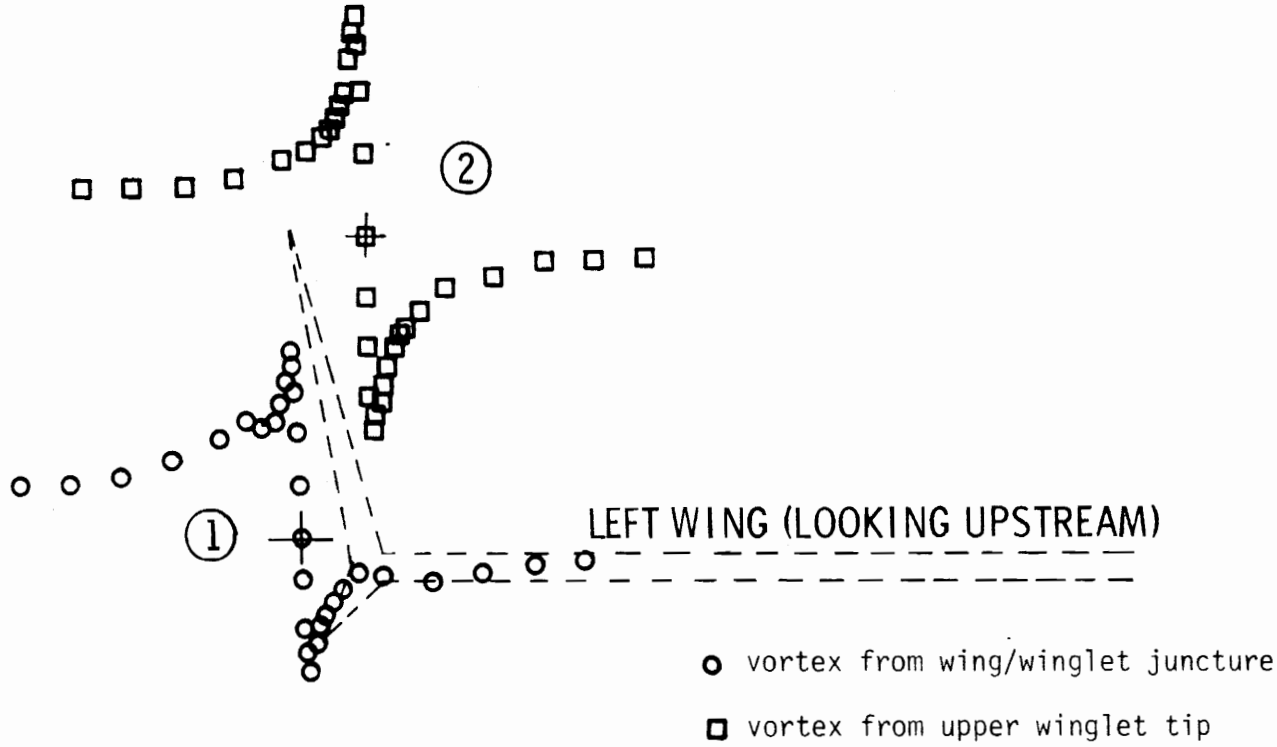

Fig. 39. Winglet Vortices (Z/C = 5).

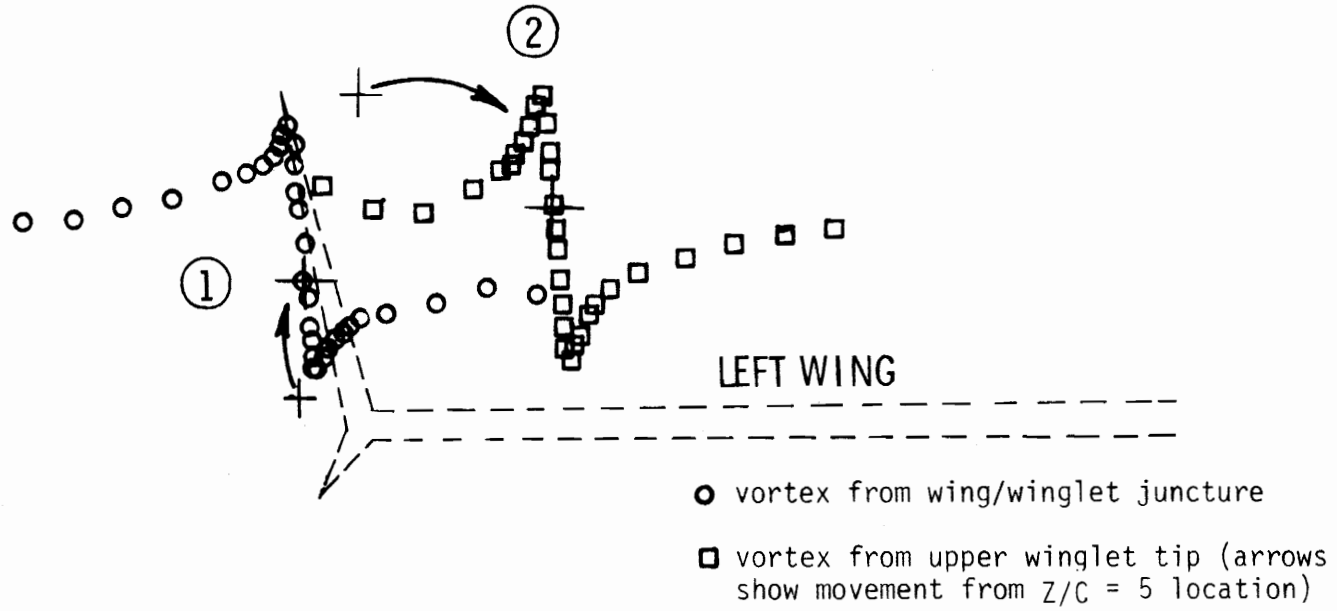

Fig. 40. Winglet Vortices (Z/C = 20).

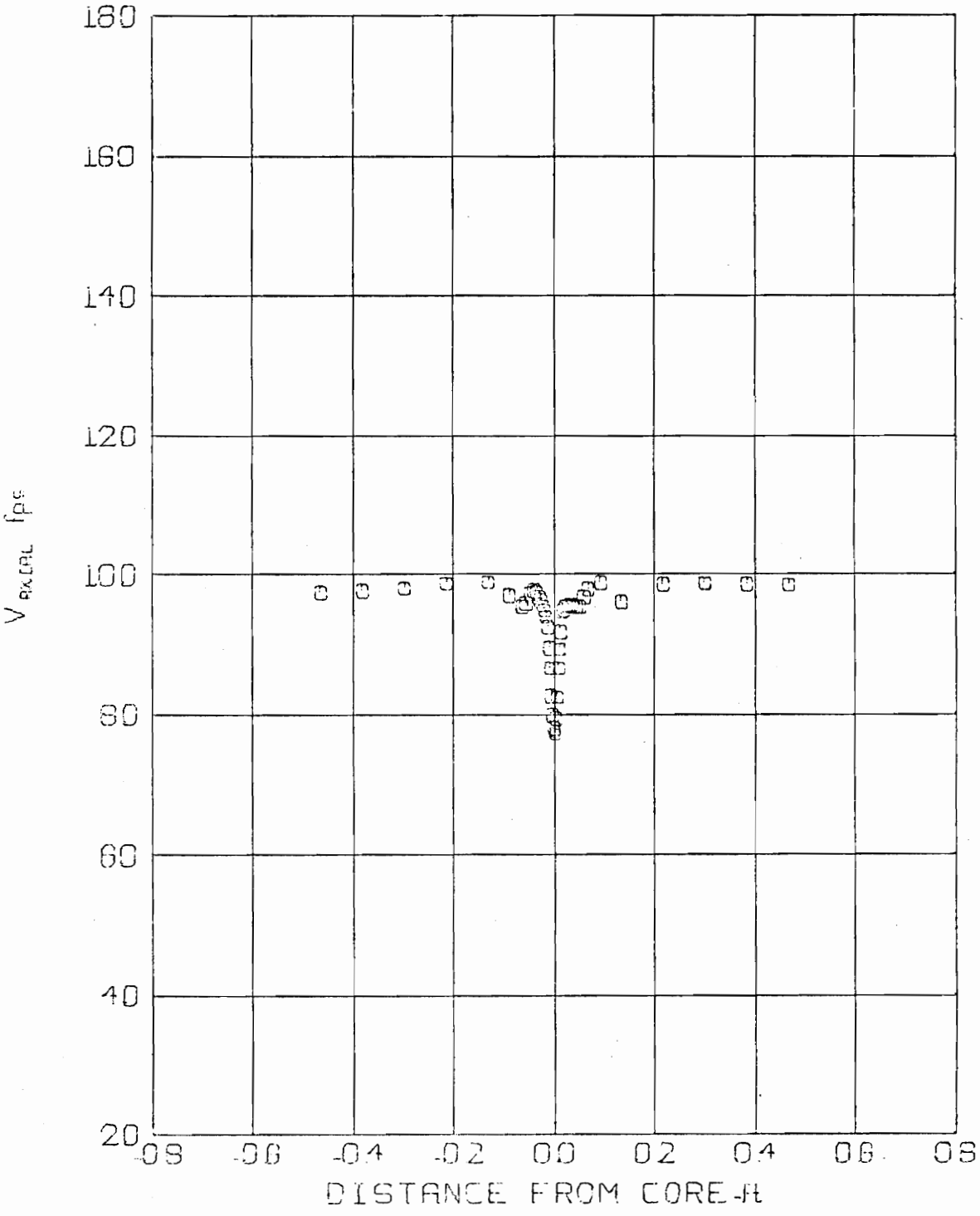

Fig. 41. Axial Velocity Profile, Winglet Vortex 1.
V_∞ = 103.7 fps Z/C = 5

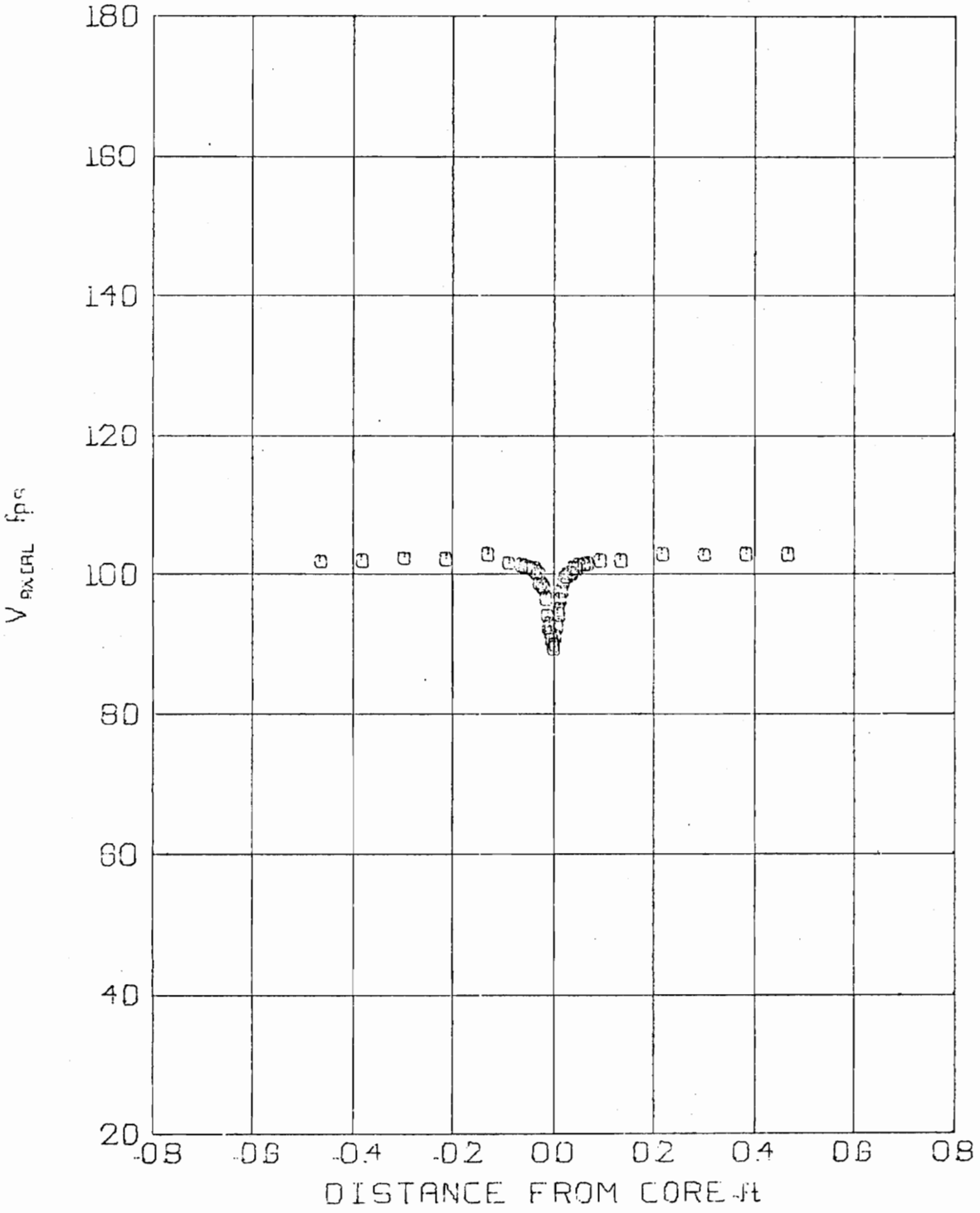

Fig. 42. Axial Velocity Profile, Winglet Vortex 1.
V_∞ = 105.1 fps Z/C = 20

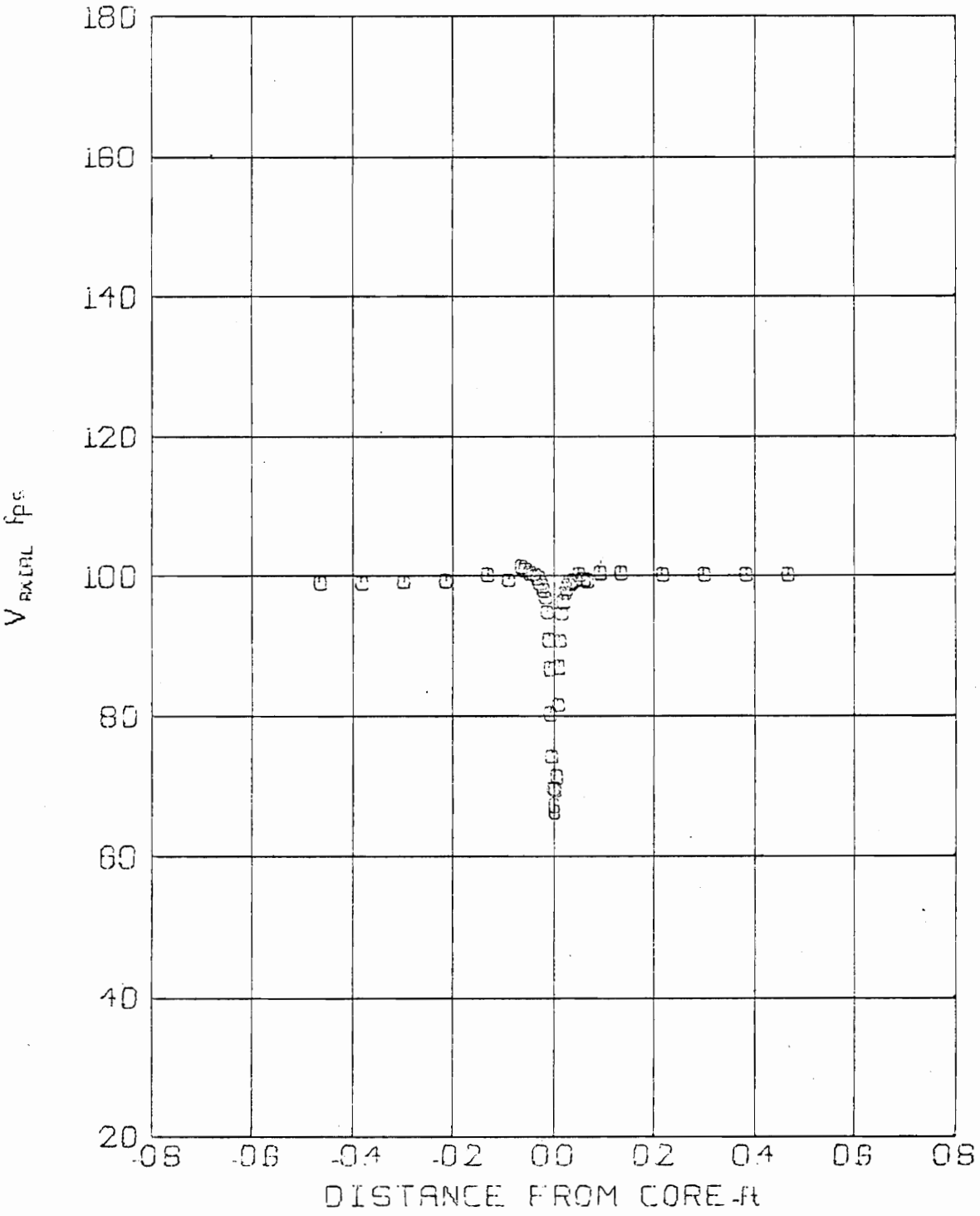

Fig. 43. Axial Velocity Profile, Winglet Vortex 2.
V_∞ = 105.0 fps Z/C = 5

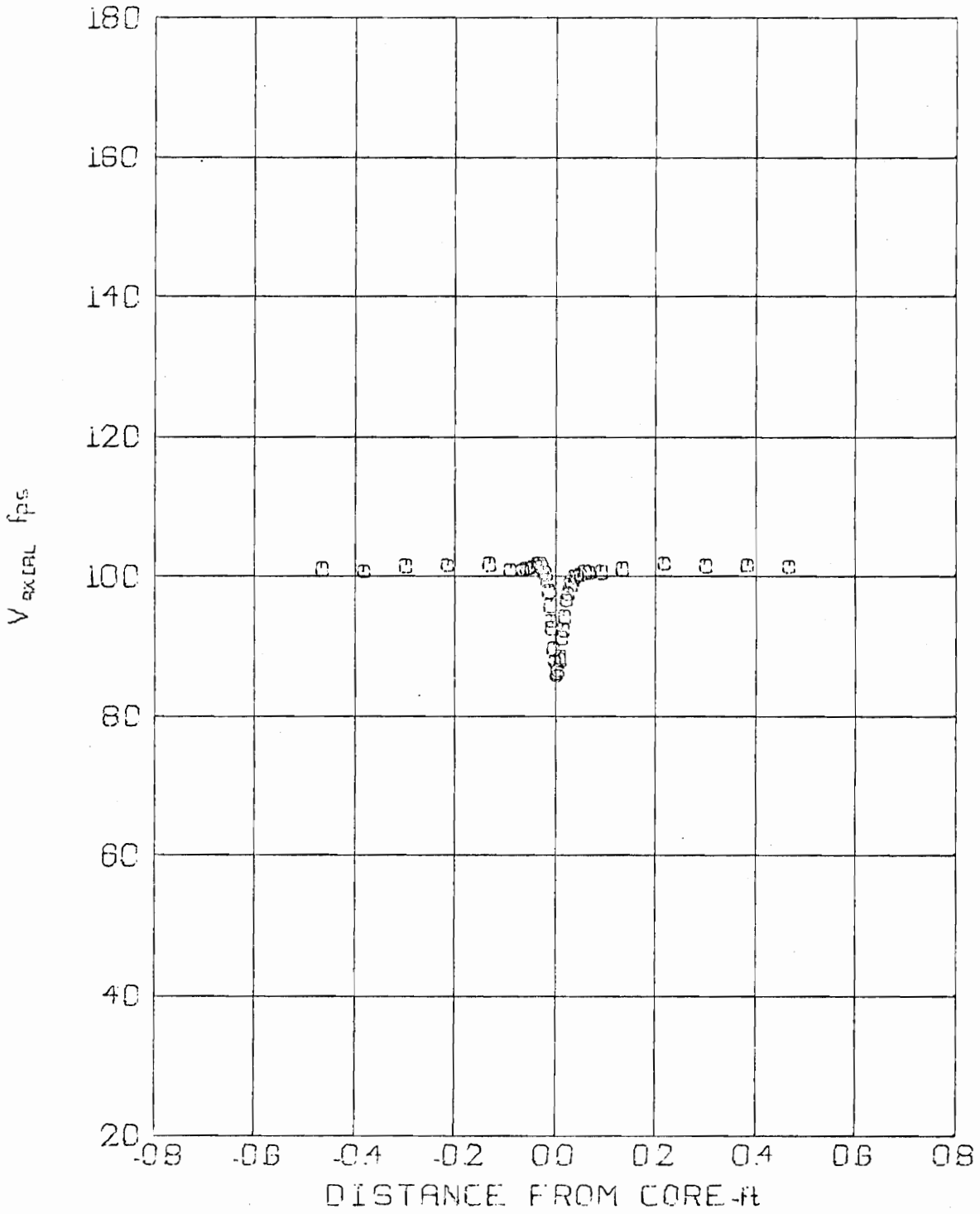

Fig. 44. Axial Velocity Profile, Winglet Vortex 2.
V_∞ = 103.7 fps Z/C = 20

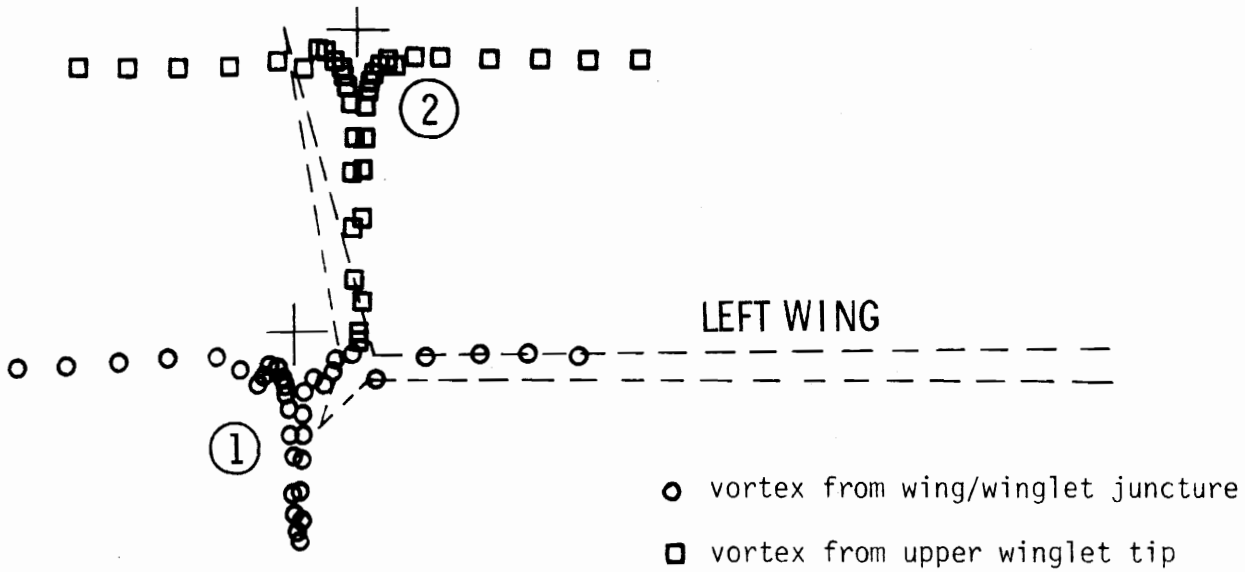

Fig. 45. Winglet Axial Velocity Profiles (Z/C = 5).

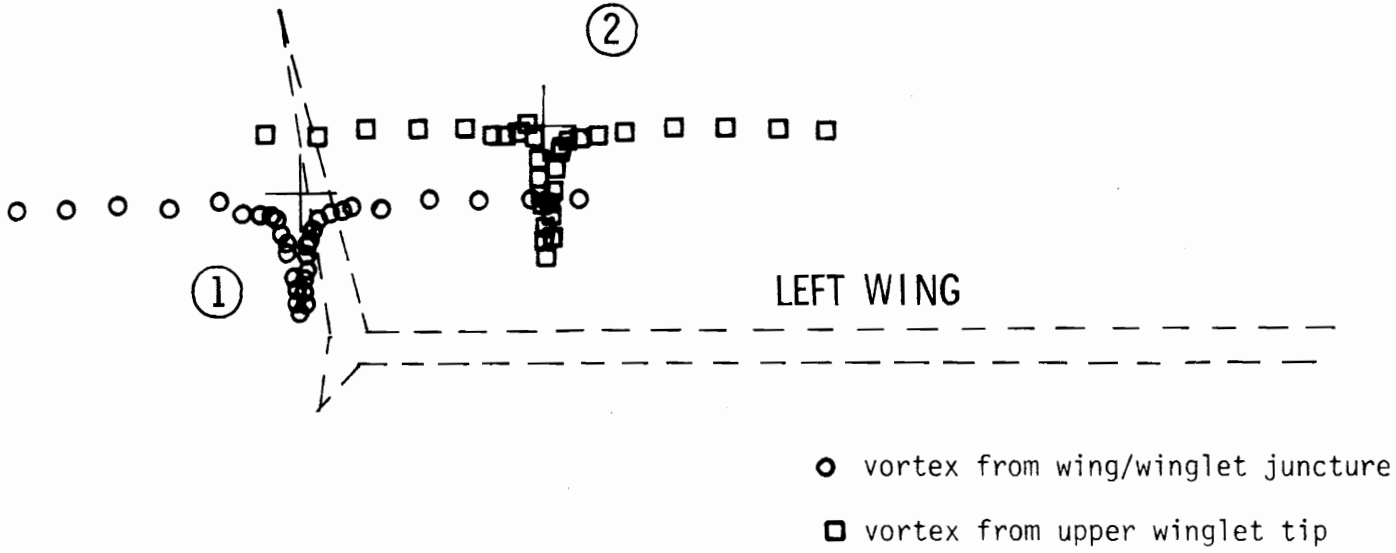

Fig. 46. Winglet Axial Velocity Profiles (Z/C = 20).

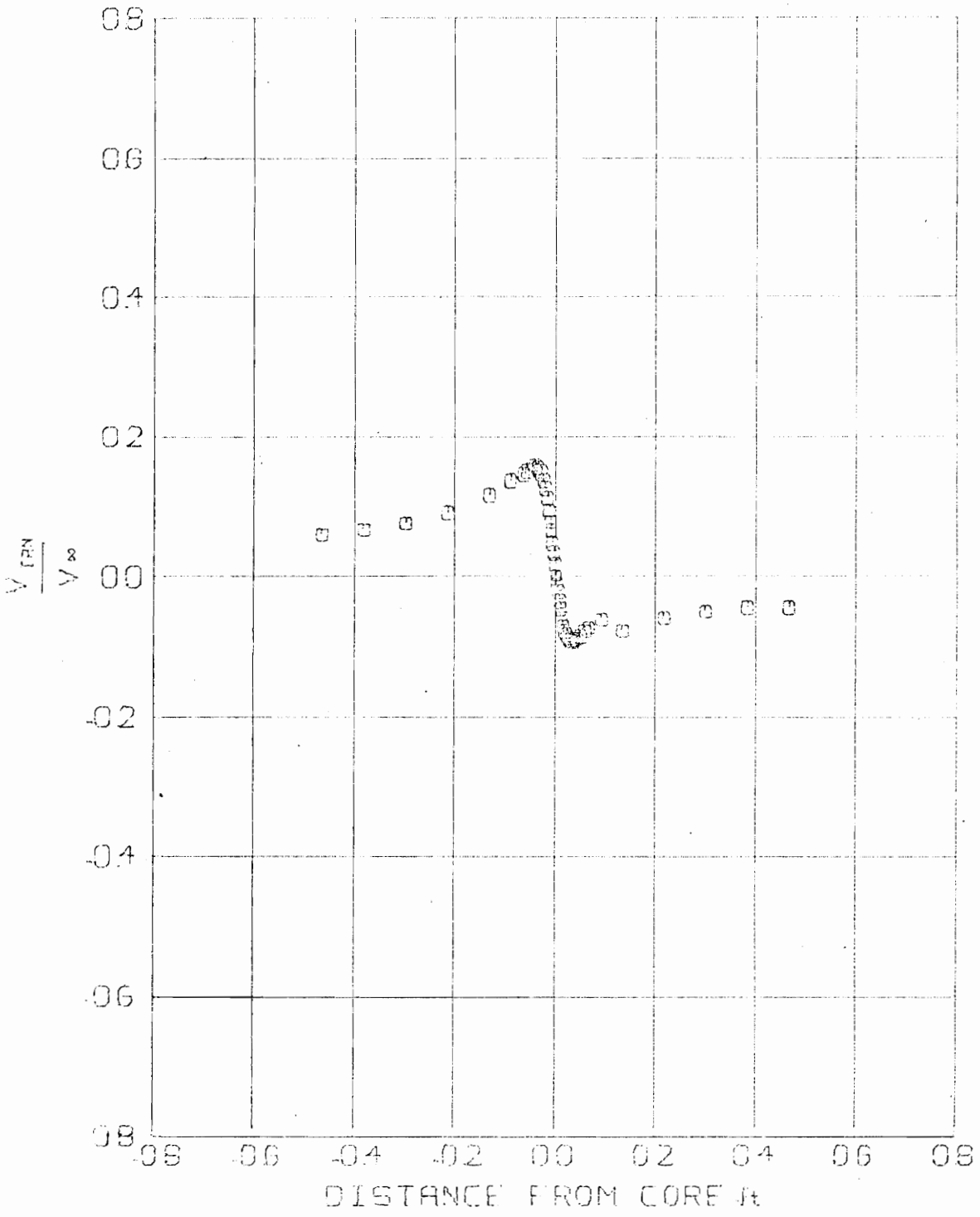

Fig. 47. Tangential Velocity Profile, Upper Winglet Vortex 1.
V_∞ = 104.0 fps Z/C = 5

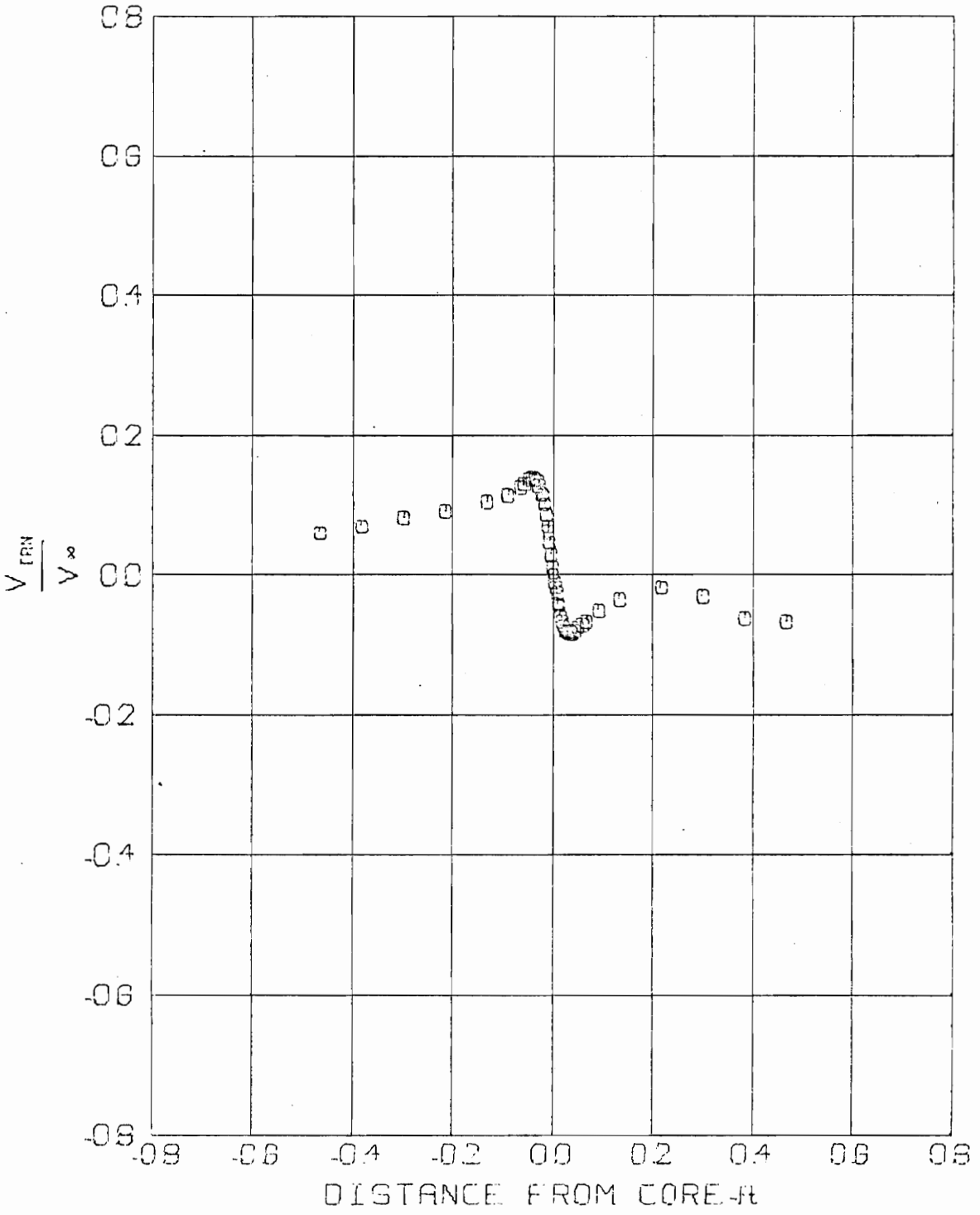

Fig. 48. Tangential Velocity Profile, Upper Winglet Vortex 1.
V_∞ = 104.6 fps Z/C = 20

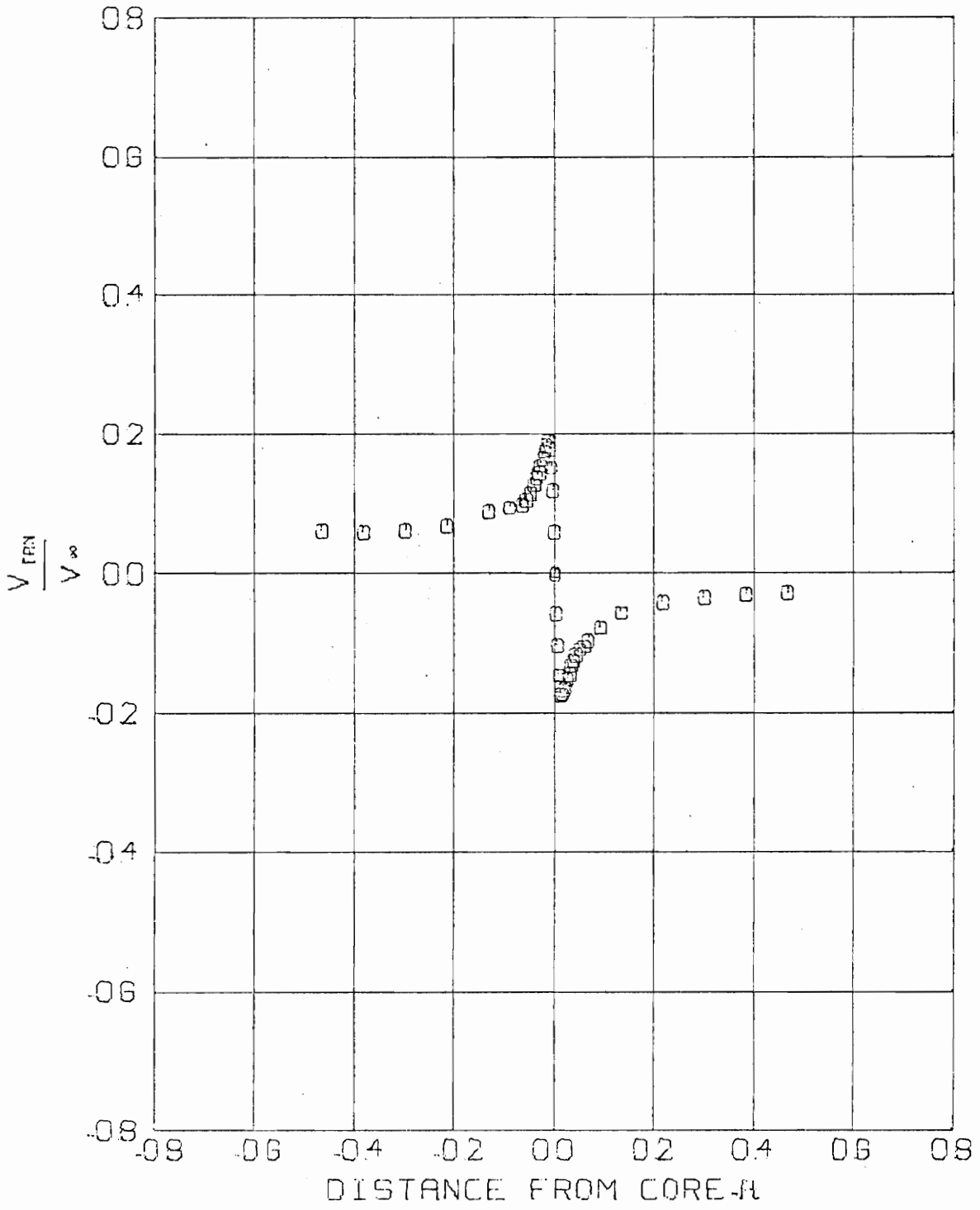

Fig. 49. Tangential Velocity Profile, Upper Winglet Vortex 2.
V_∞ = 102.1 fps Z/C = 5

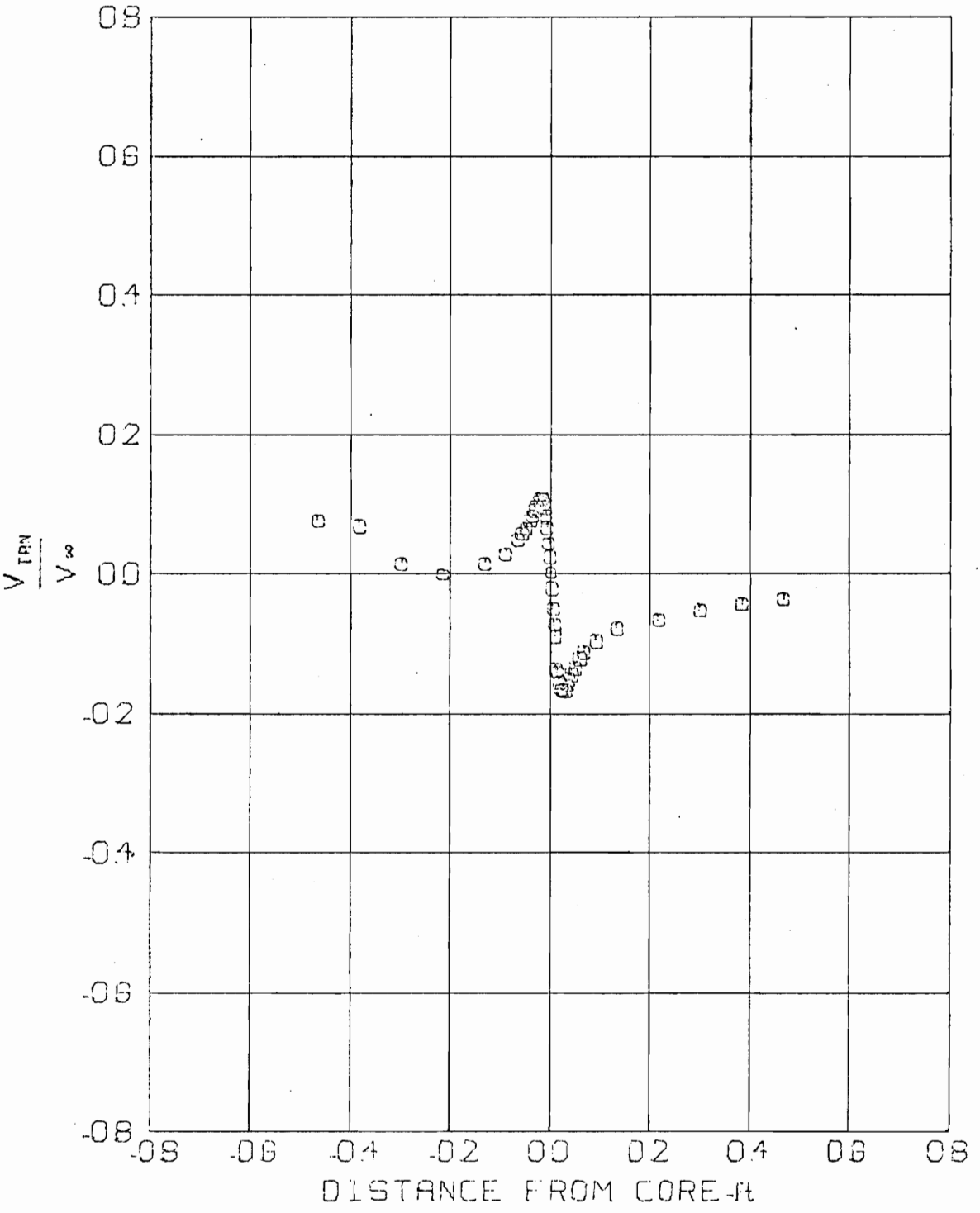

Fig. 50. Tangential Velocity Profile, Upper Winglet Vortex 2.
V_∞ = 103.3 fps Z/C = 20

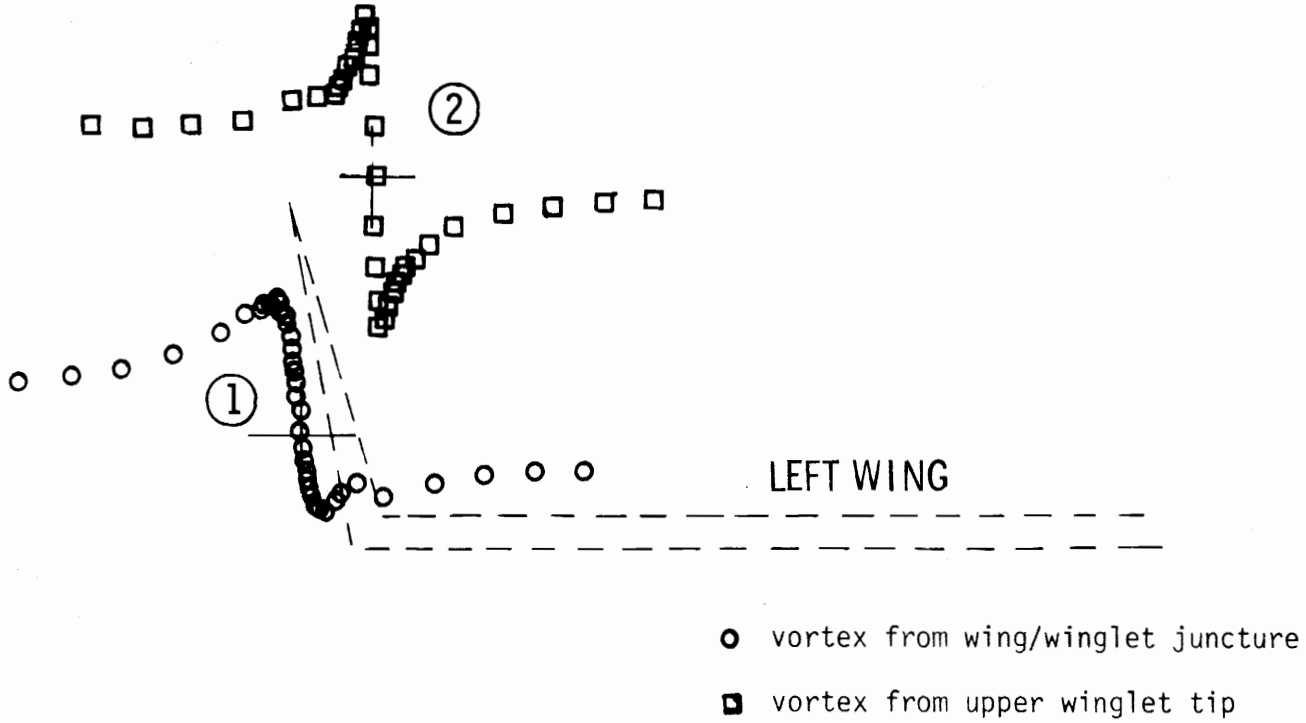

Fig. 51. Upper Winglet Vortices (Z/C = 5).

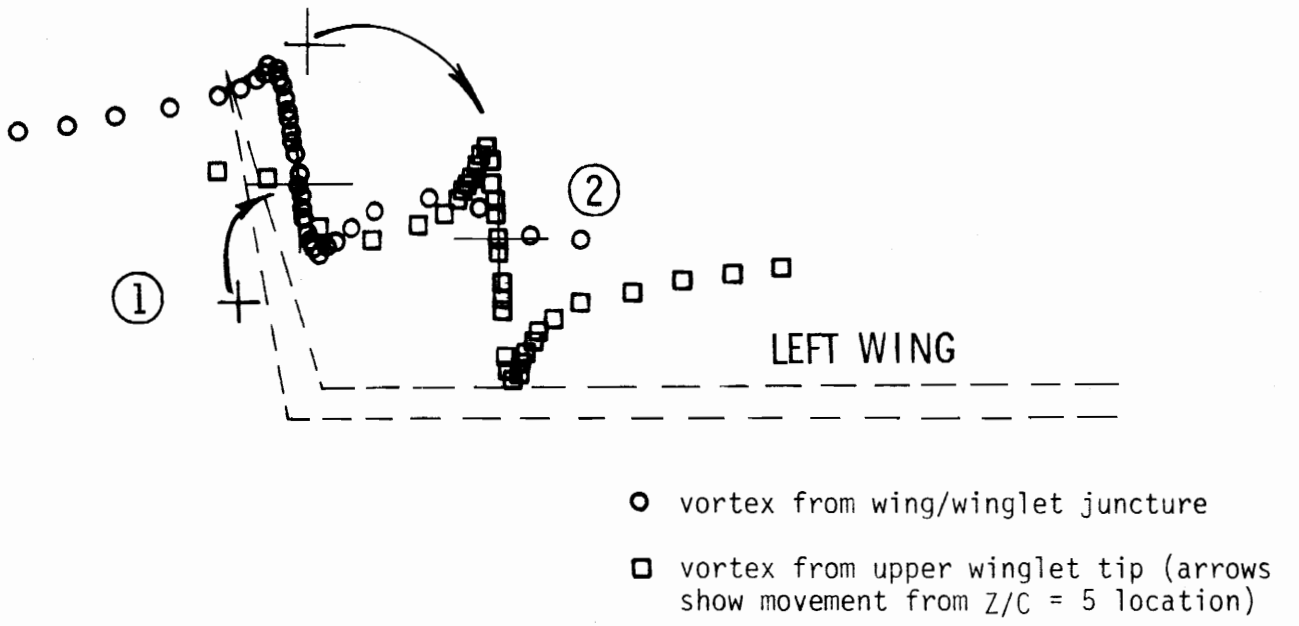

Fig. 52. Upper Winglet Vortices (Z/C = 20).

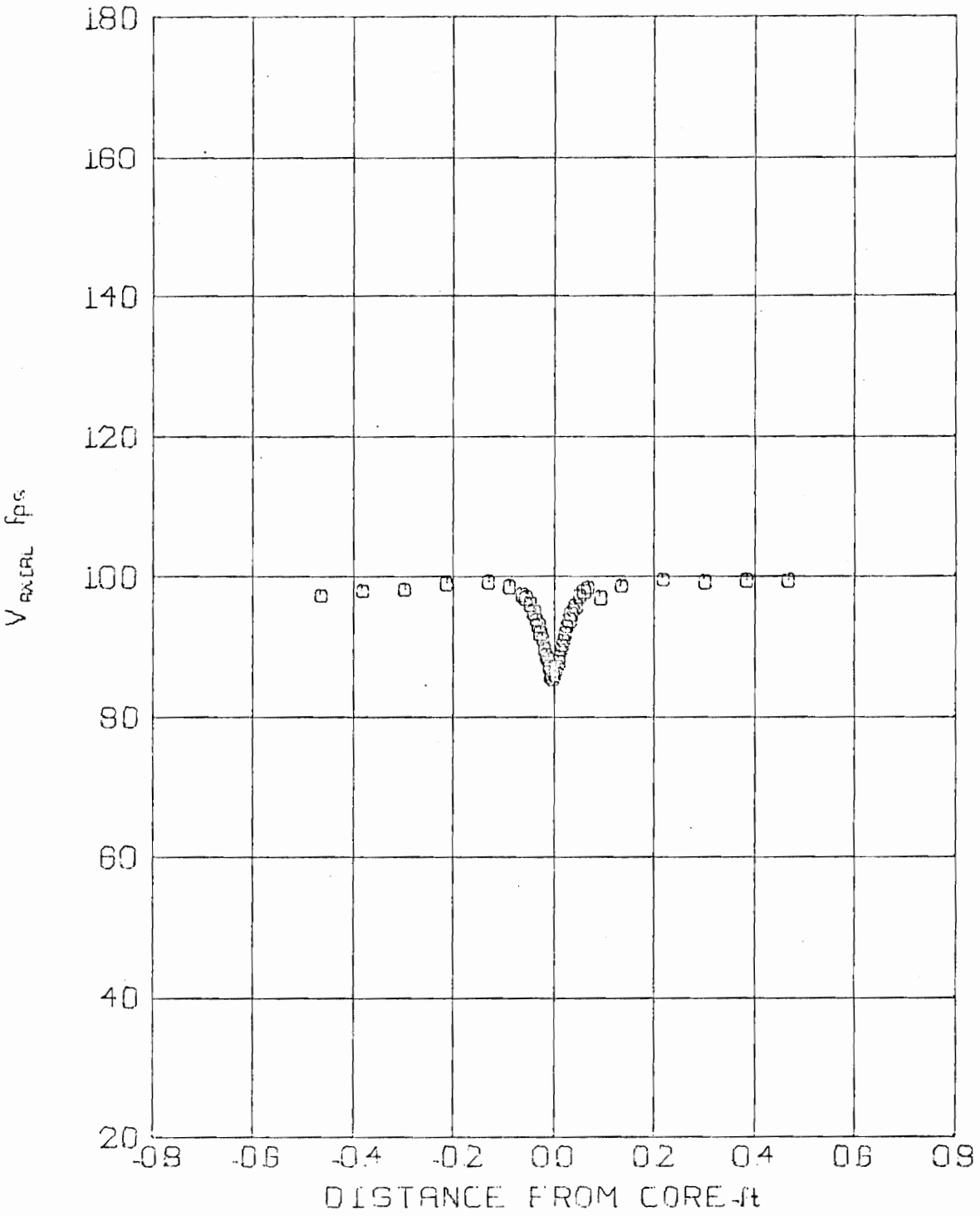

Fig. 53. Axial Velocity Profile, Upper Winglet Vortex 1.
V_∞ = 104.0 fps Z/C = 5

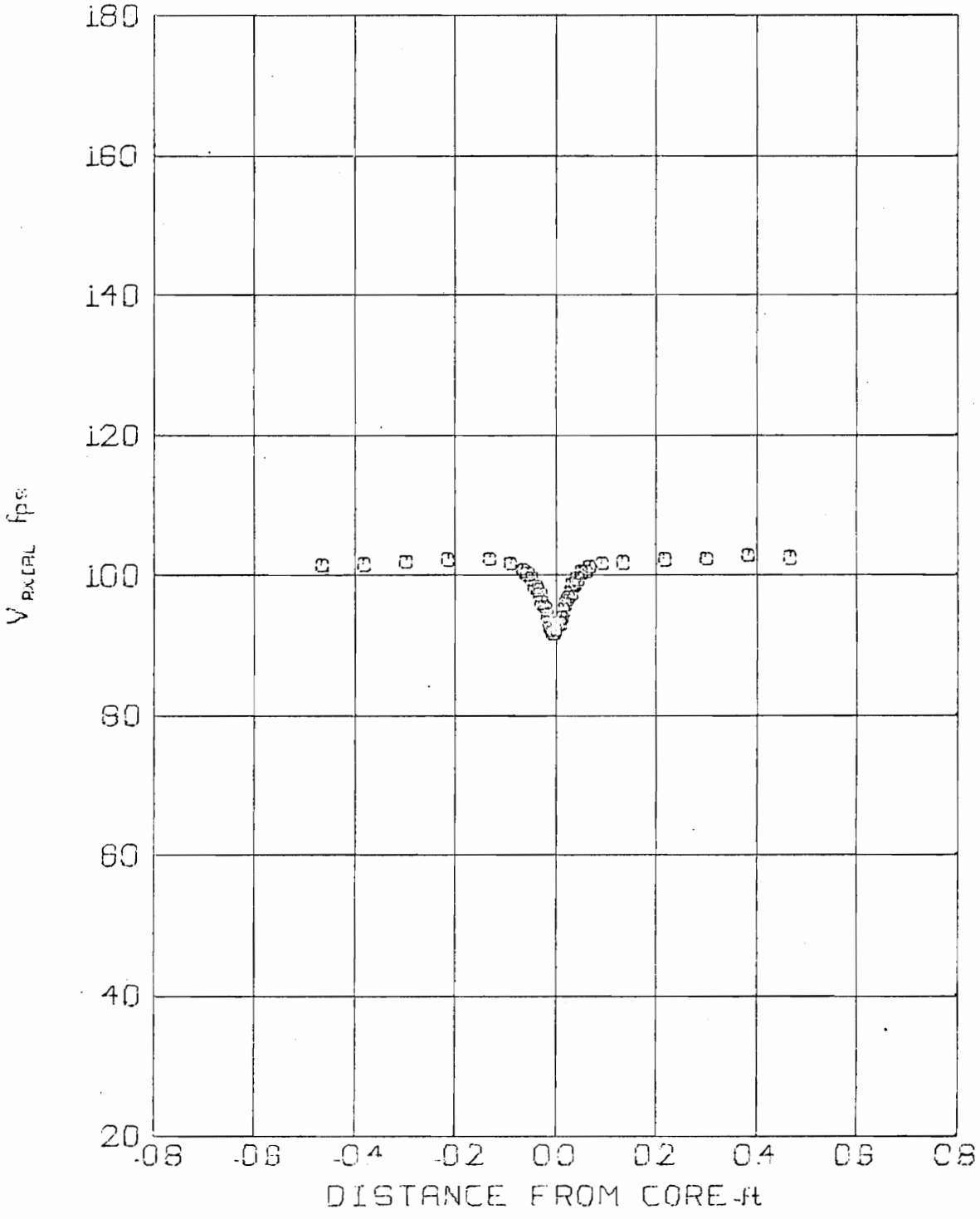

Fig. 54. Axial Velocity Profile, Upper Winglet Vortex 1.
V_∞ = 104.6 fps Z/C = 20

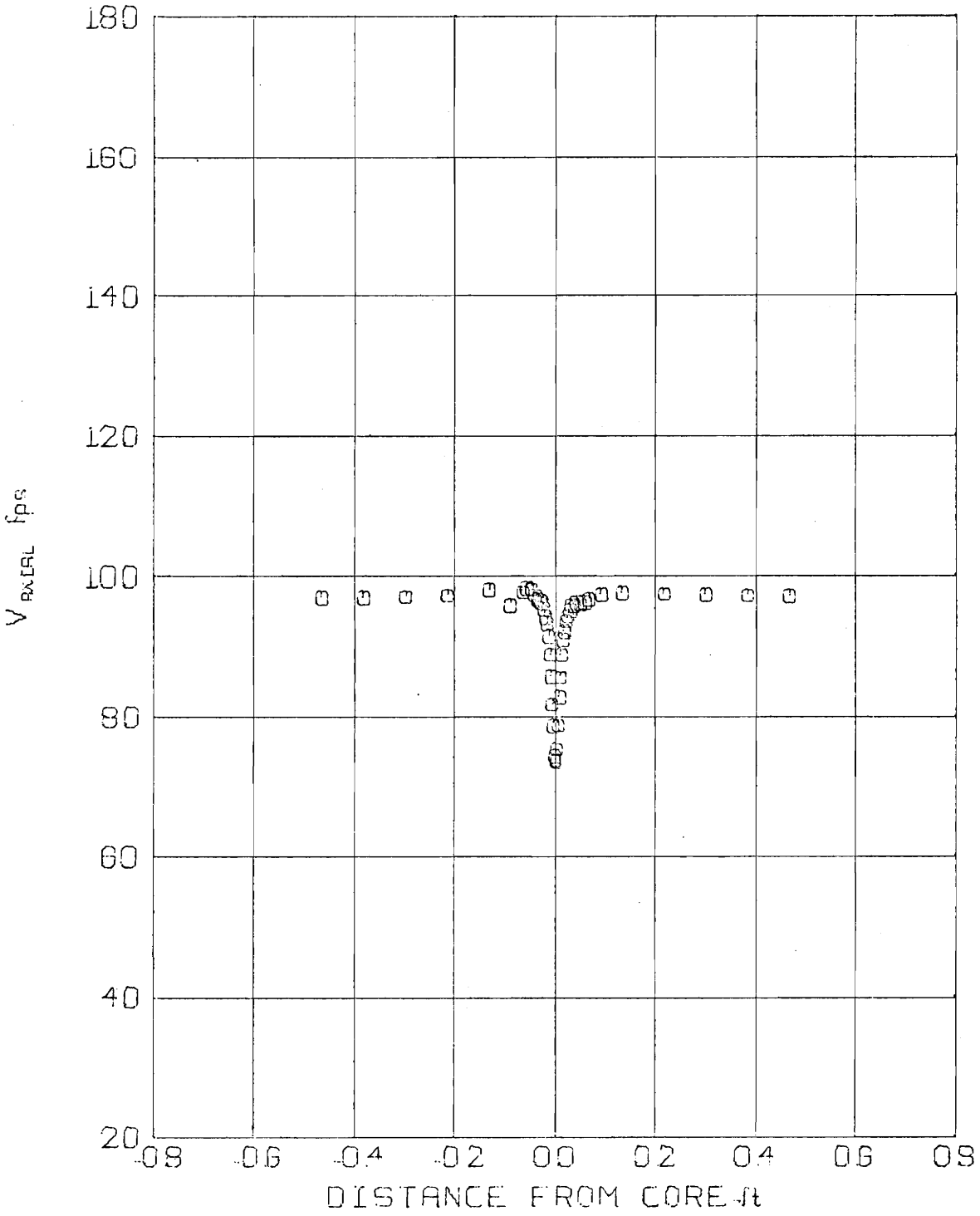

Fig. 55. Axial Velocity Profile, Upper Winglet Vortex 2.
V_∞ = 102.1 fps Z/C = 5

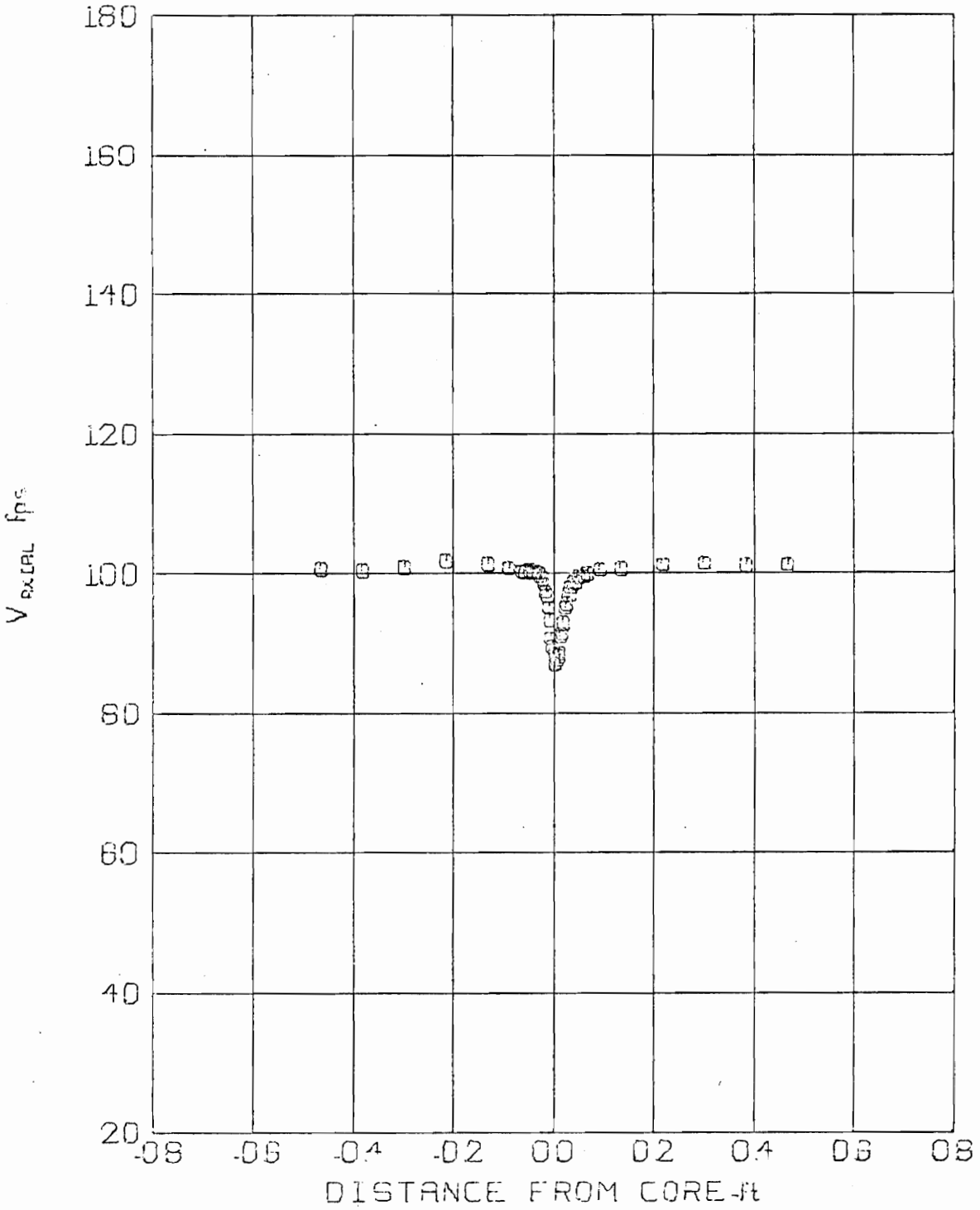

Fig. 56. Axial Velocity Profile, Upper Winglet Vortex 2.
V_∞ = 103.3 fps Z/C = 20

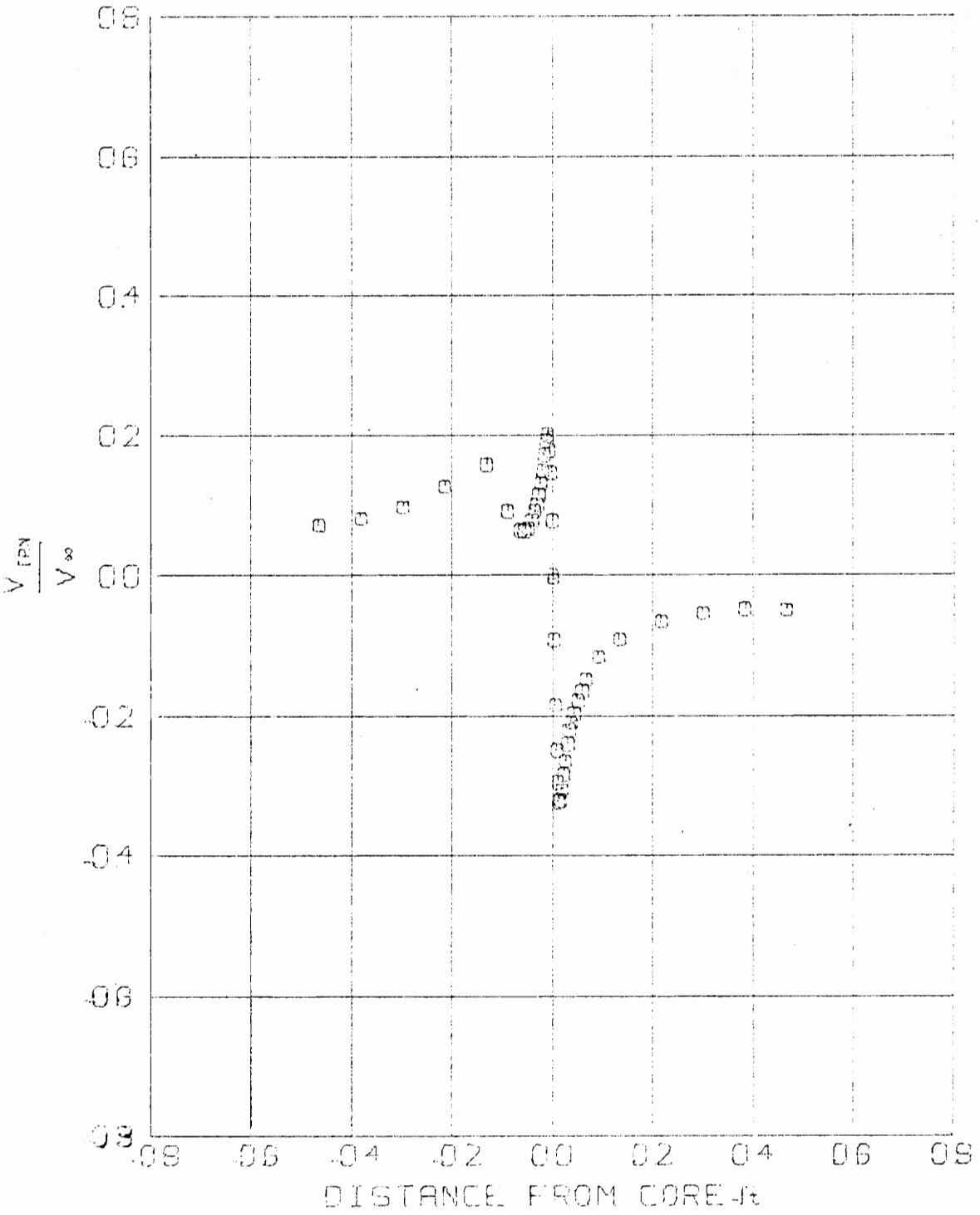

Fig. 57. Tangential Velocity Profile, Lower Winglet.
V_∞ = 102.9 fps Z/C = 5

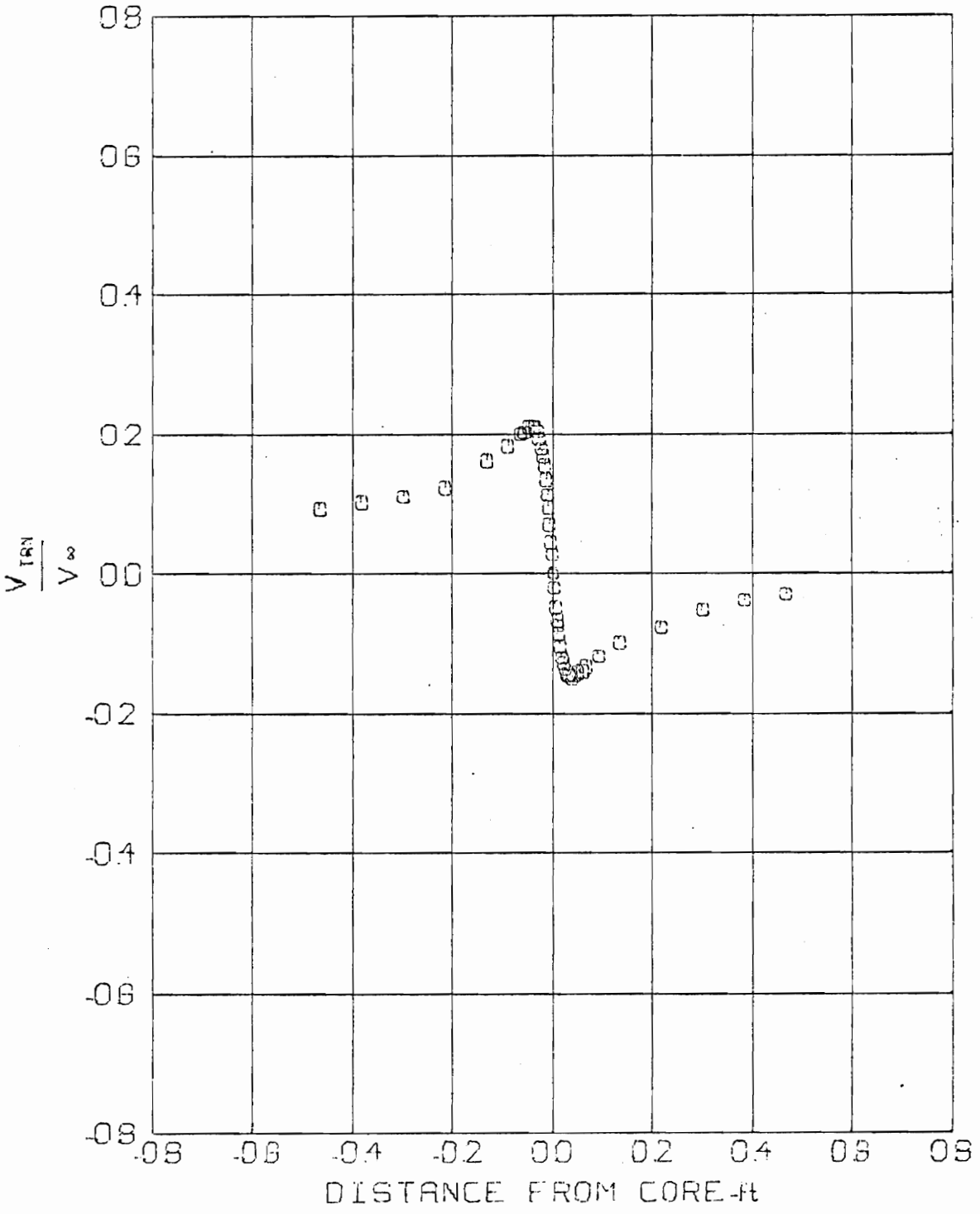

Fig. 58. Tangential Velocity Profile, Lower Winglet.
V_∞ = 104.0 fps Z/C = 20

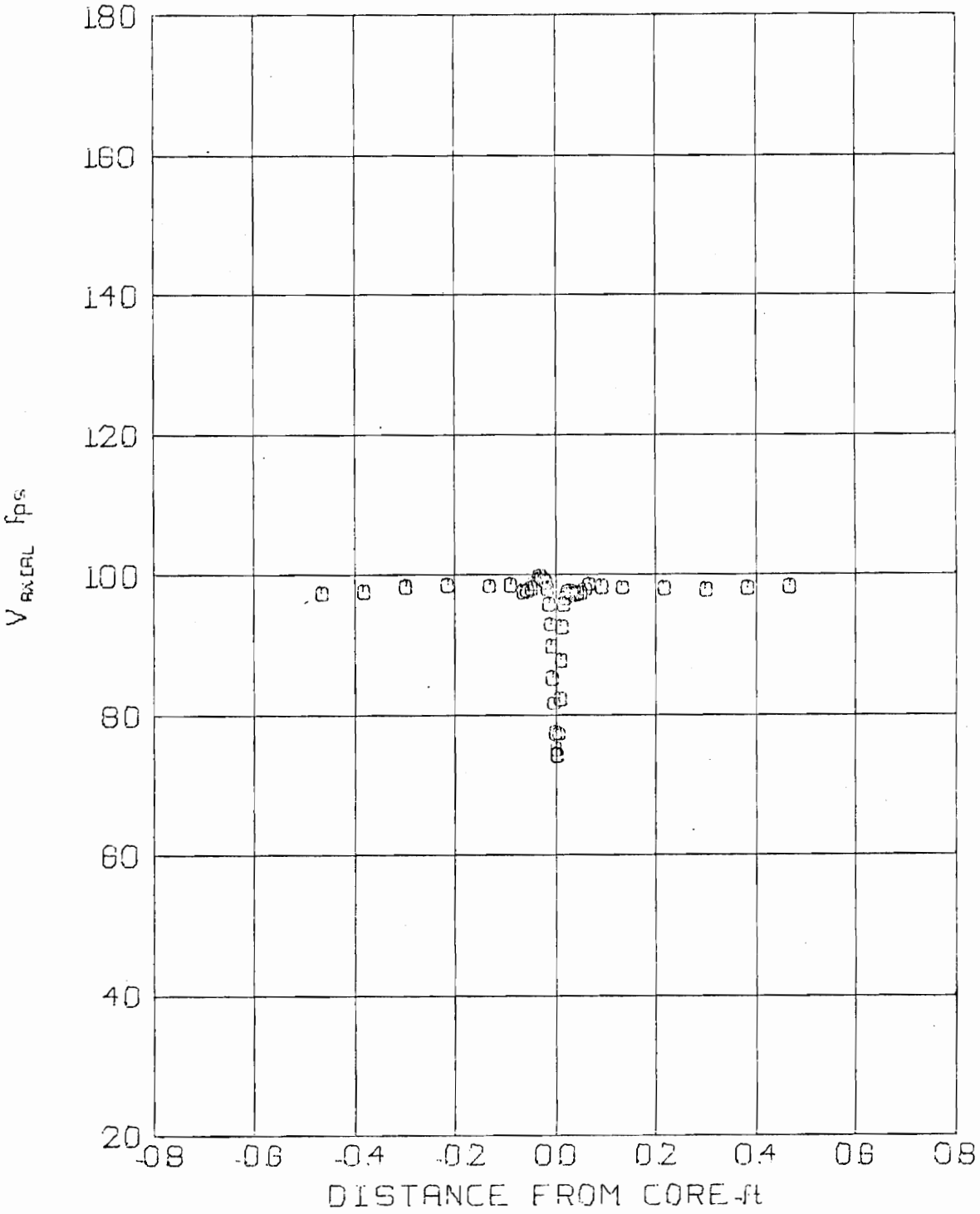

Fig. 59. Axial Velocity Profile, Lower Winglet.
V_∞ = 102.9 fps Z/C = 5

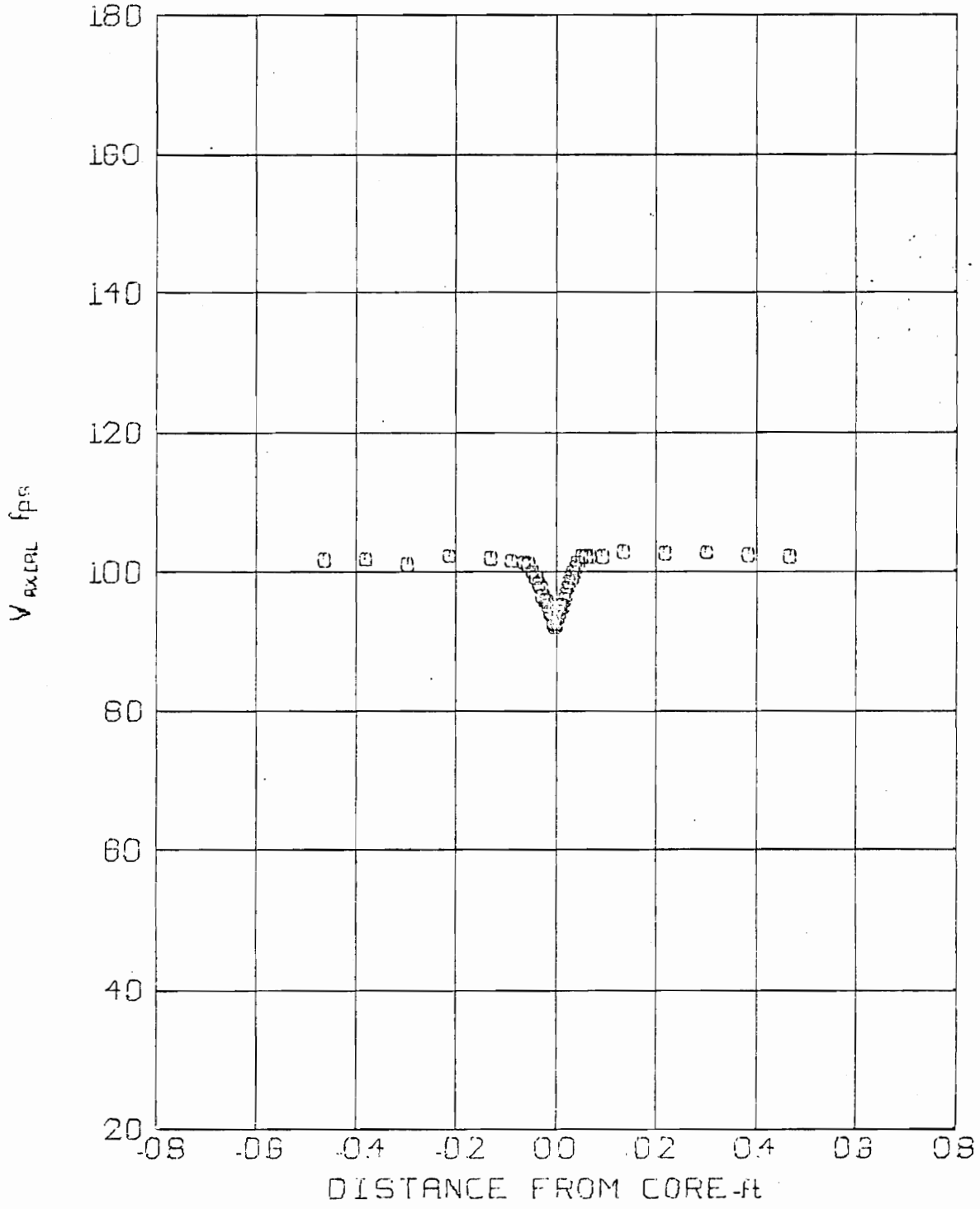

Fig. 60. Axial Velocity Profile, Lower Winglet.
V_∞ = 104.0 fps Z/C = 20

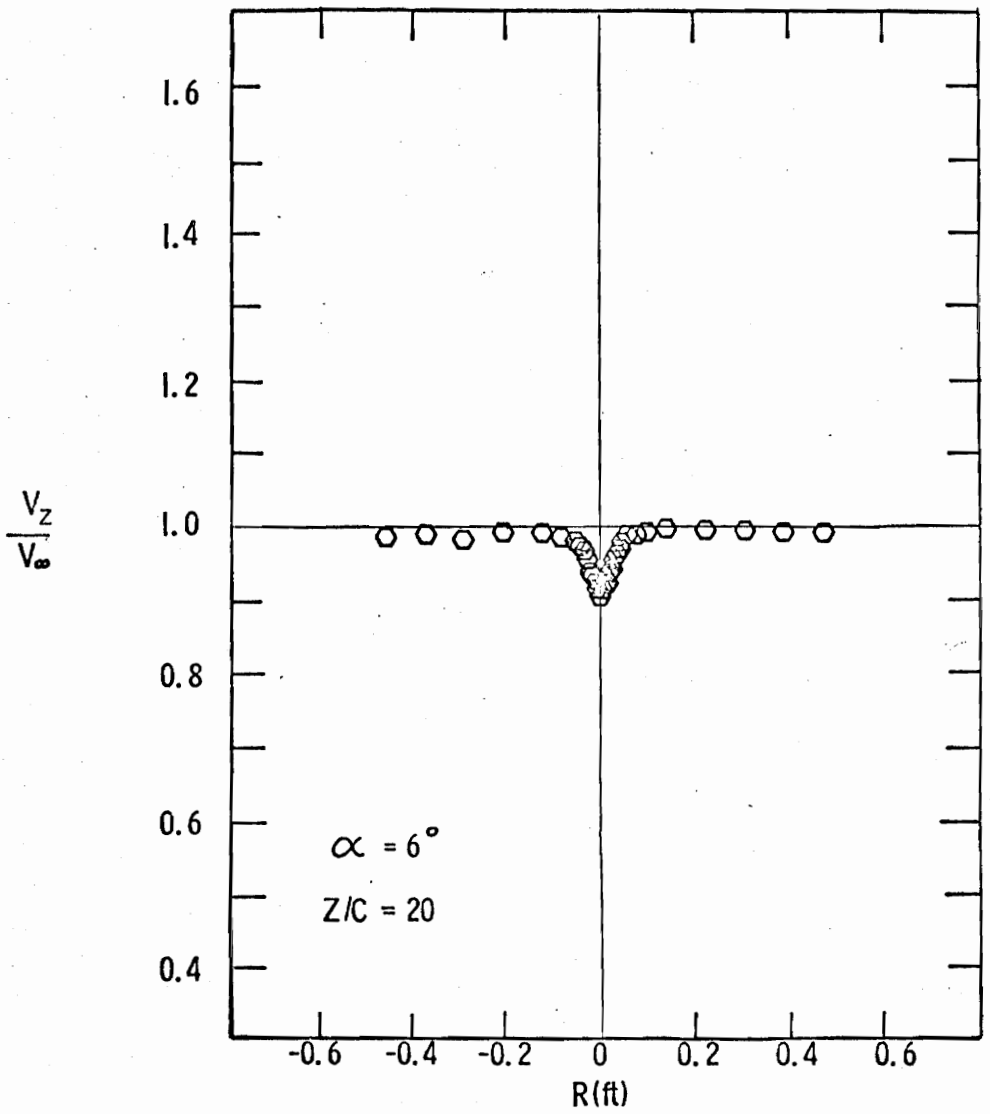

Fig. 61. Lower Winglet Axial Velocity Profile.

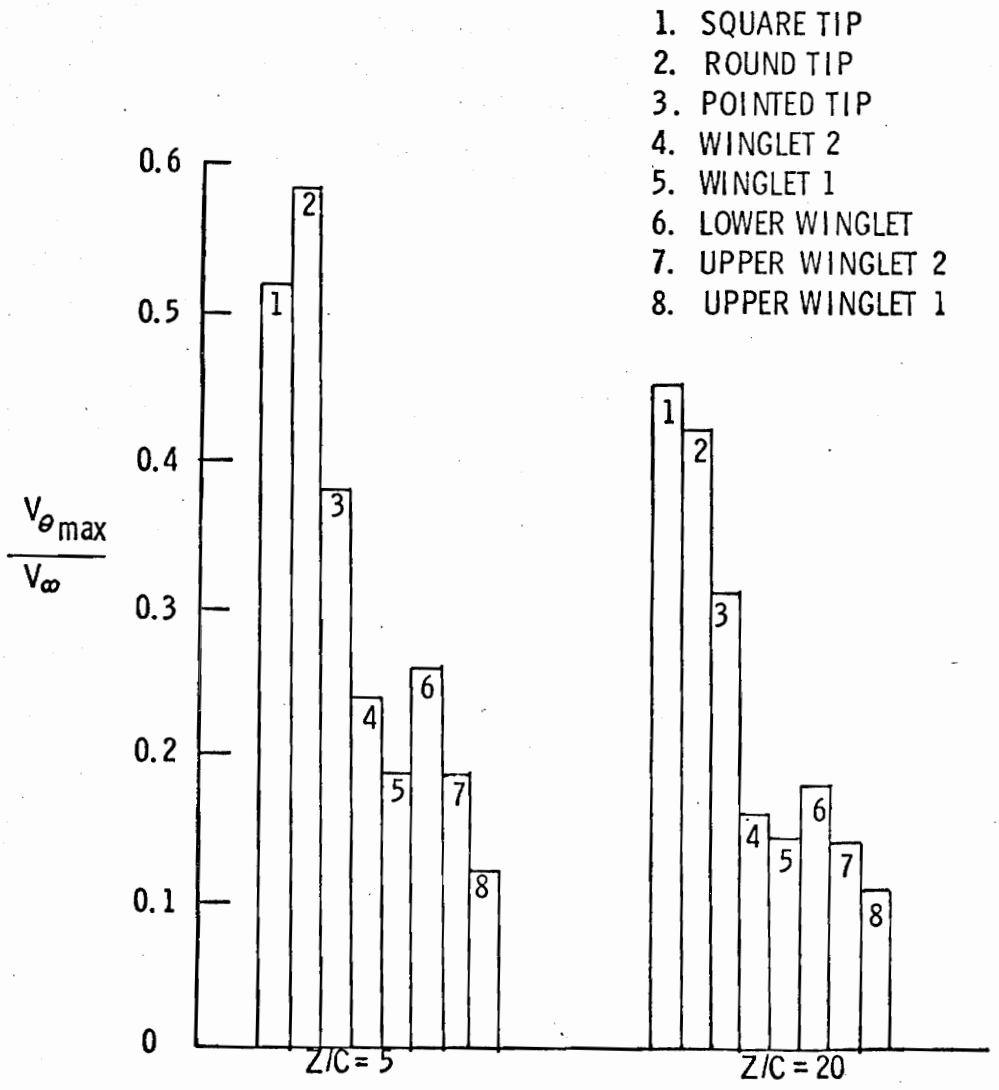

Fig. 62. Maximum Tangential Velocity Comparison.

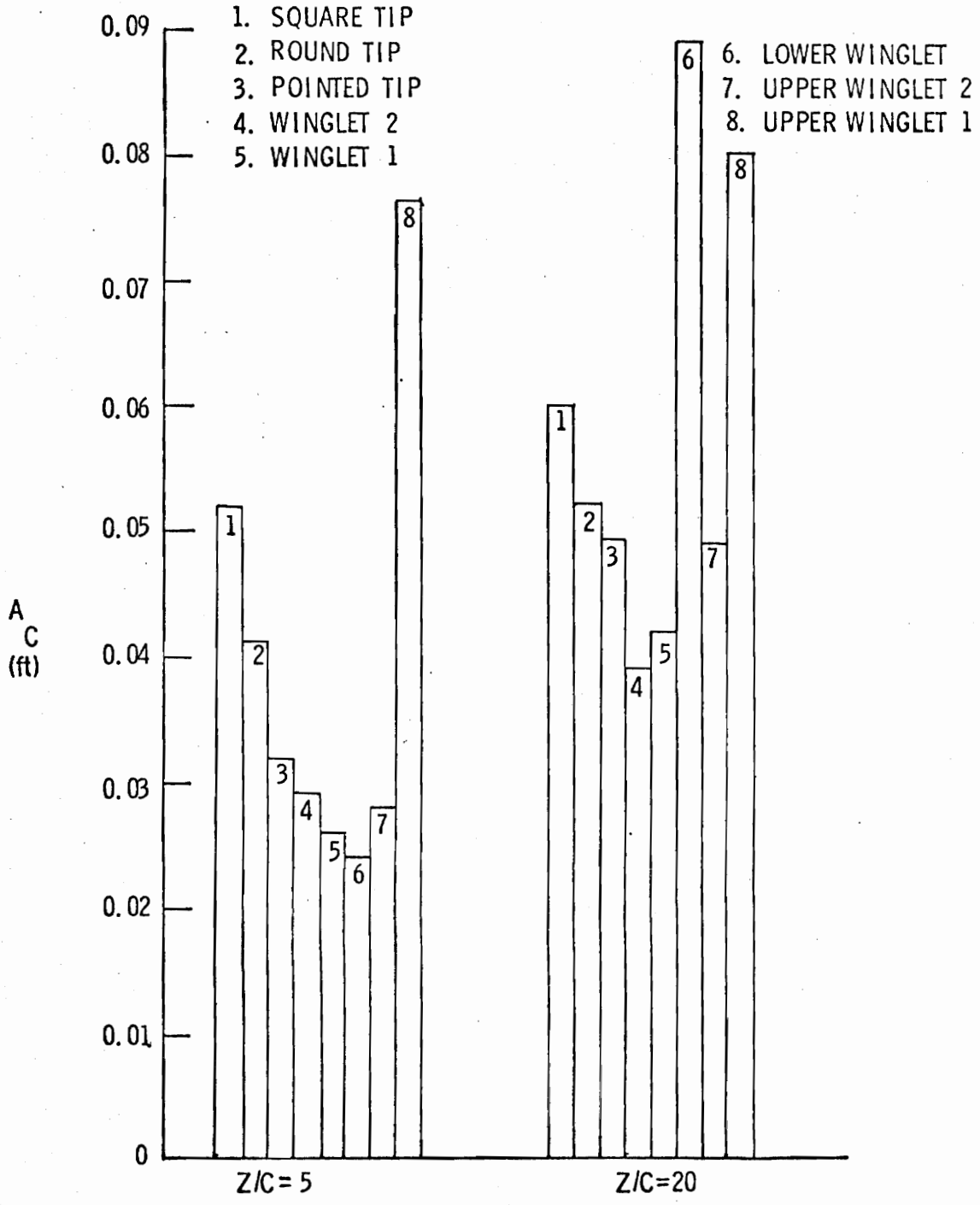

Fig. 63. Comparison of Core Size.

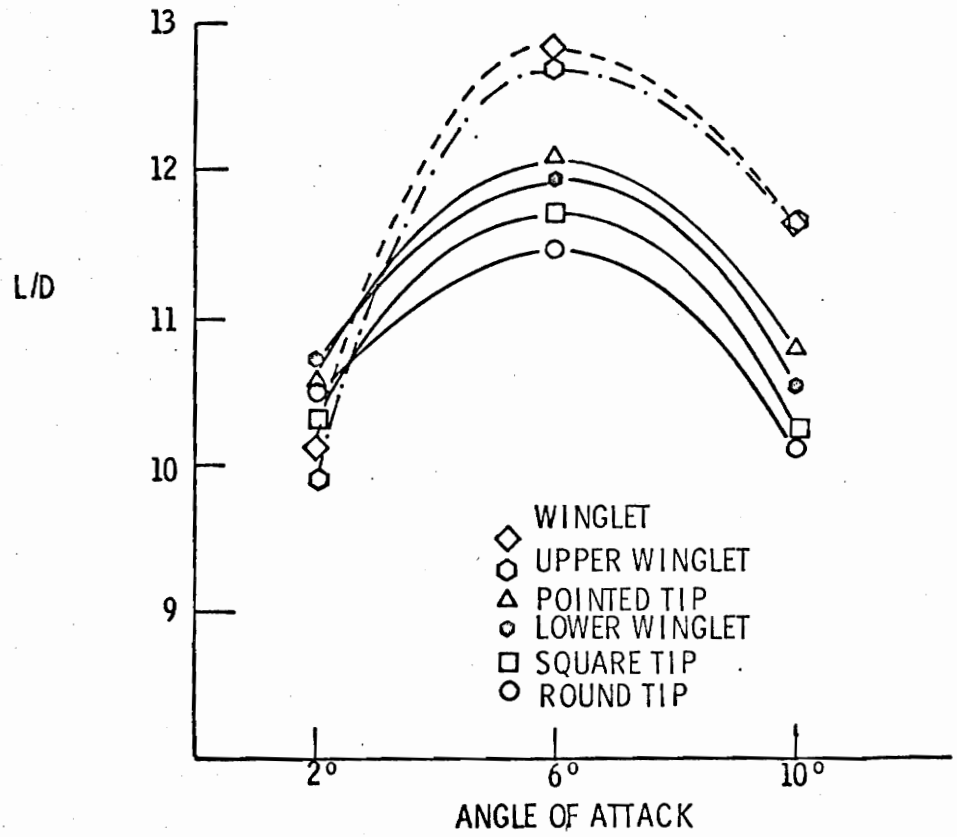

Fig. 64. Lift-Drag Ratio Comparison.

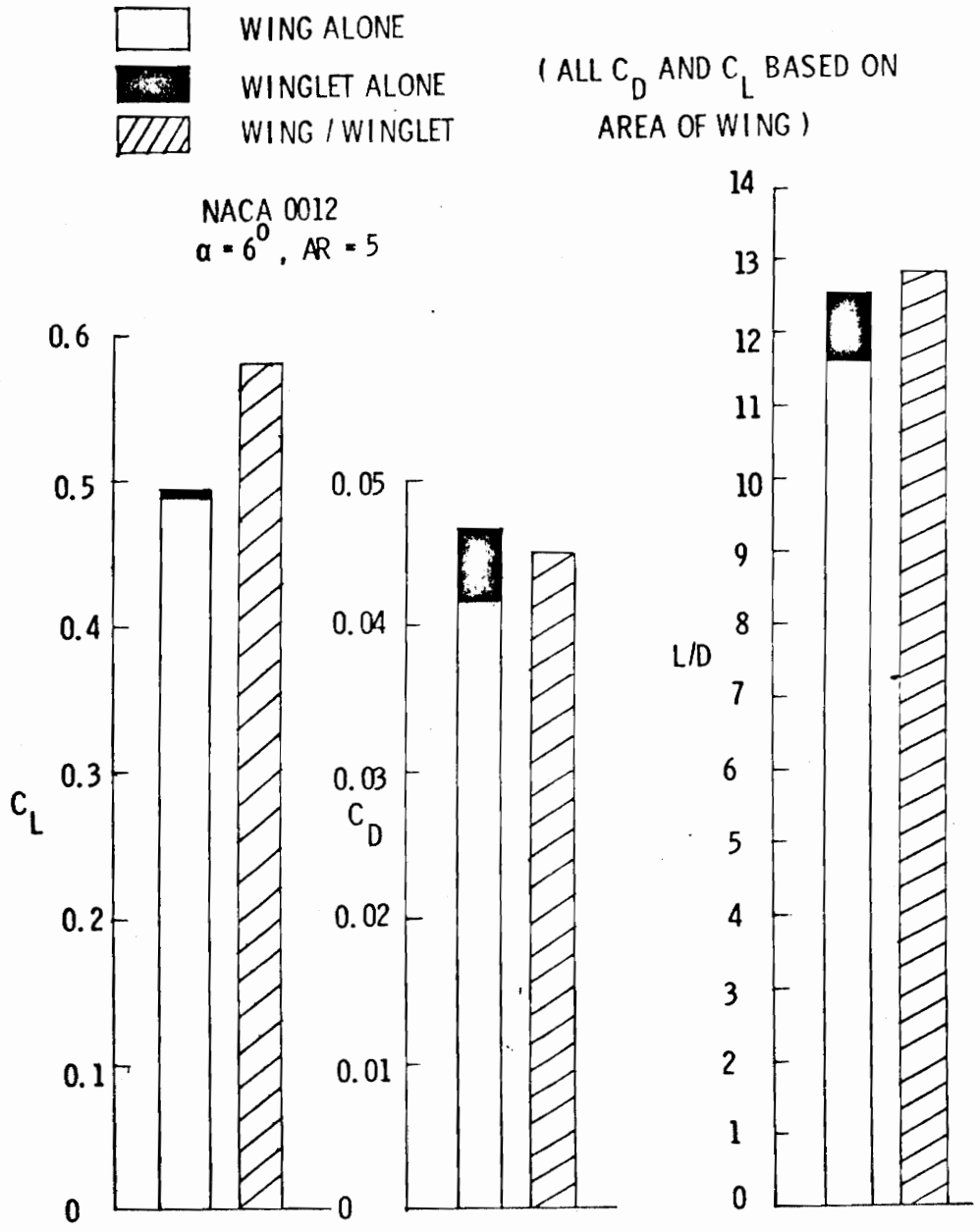

Fig. 65. Effect of Winglet on C_L & C_D.

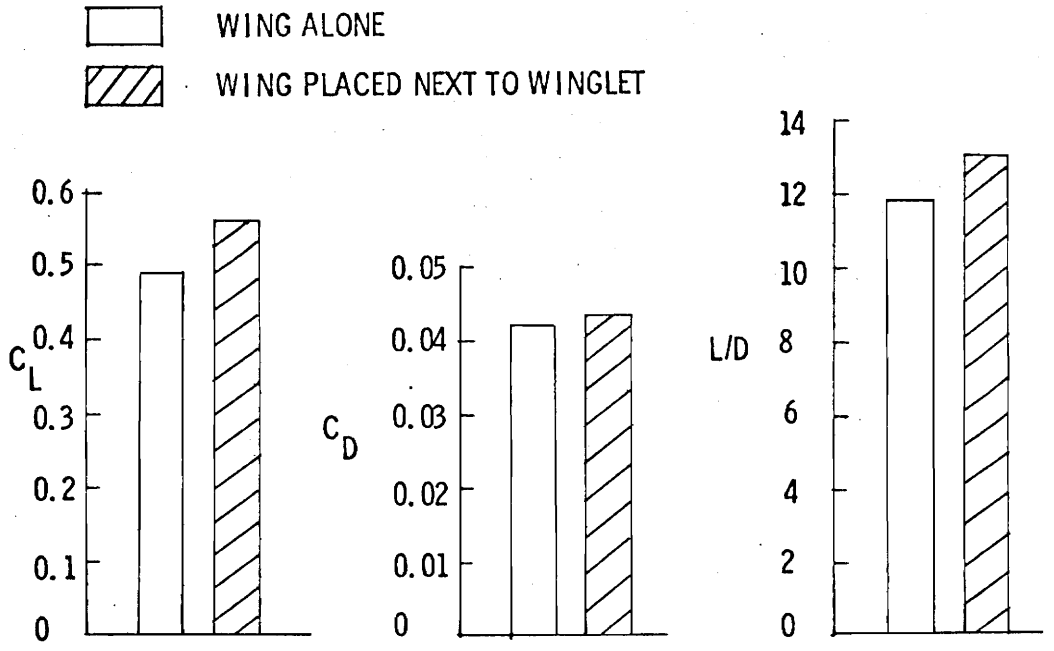

a. Effect of Winglet on Wing Forces.

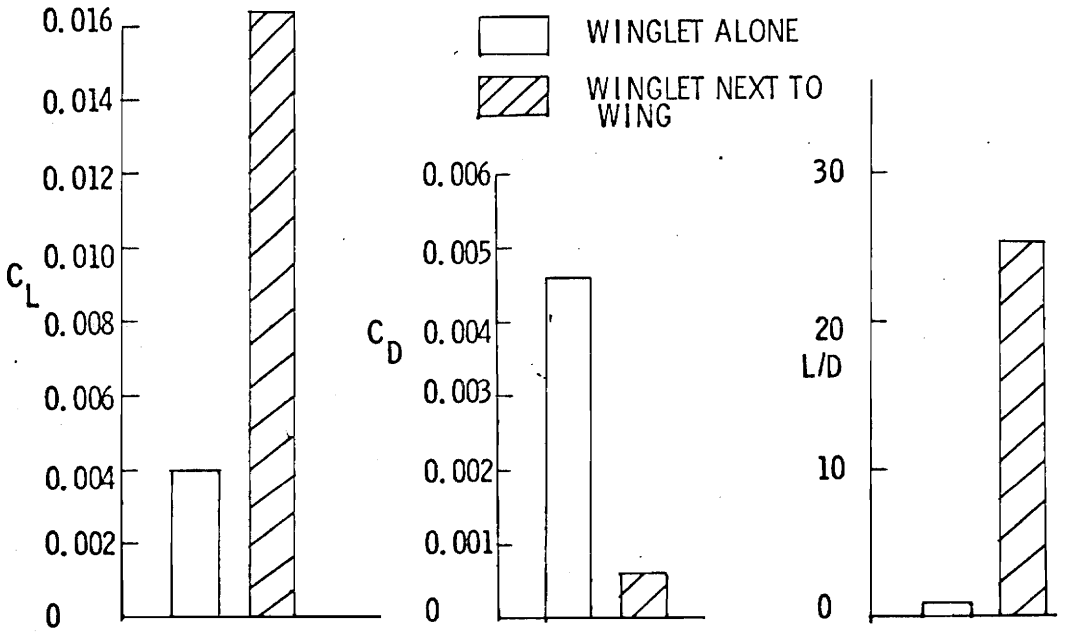

b. Effect of Wing on Winglet Forces.

Fig. 66. Interactive Effects of Wing/Winglet Forces.

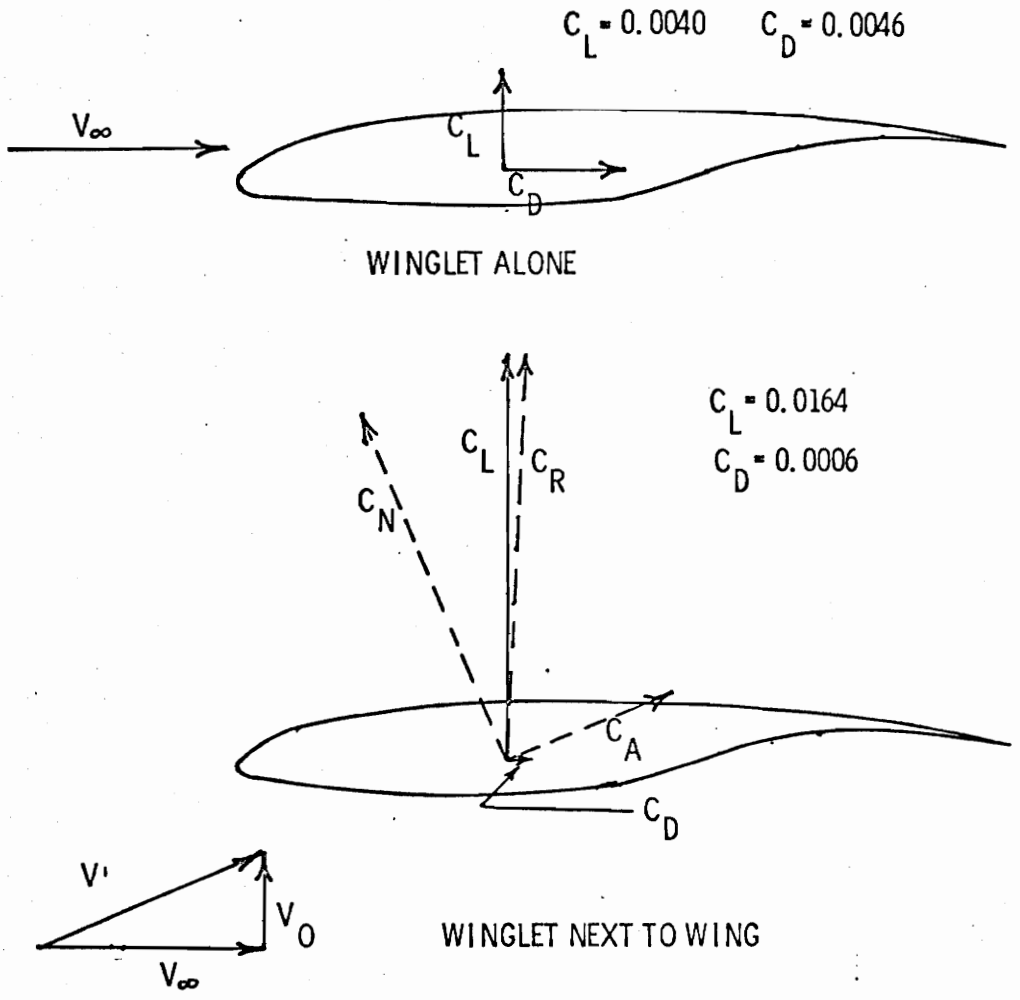

Fig. 67. Forces on Winglet.

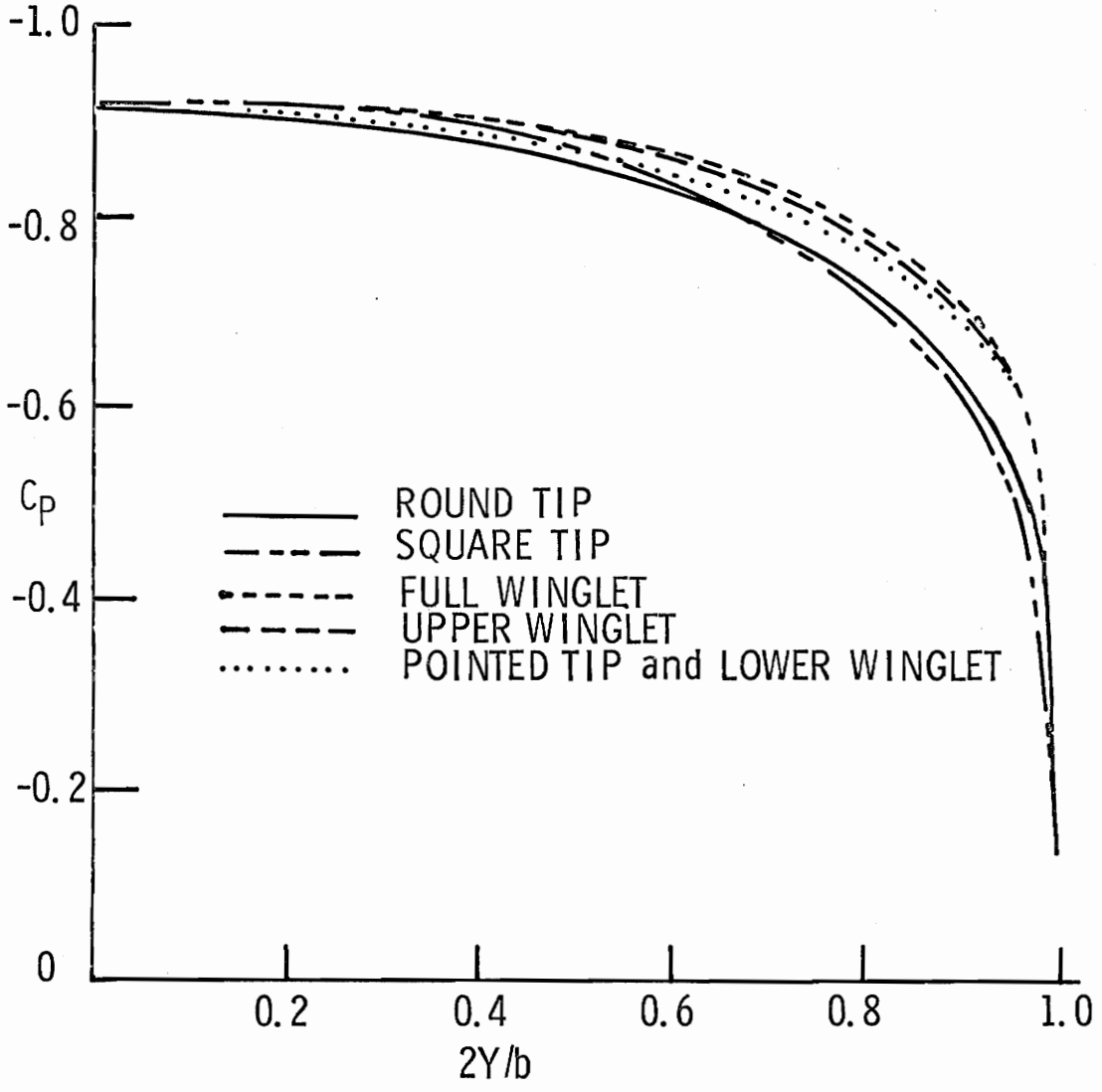

Fig. 68. Spanwise Pressure Distributions

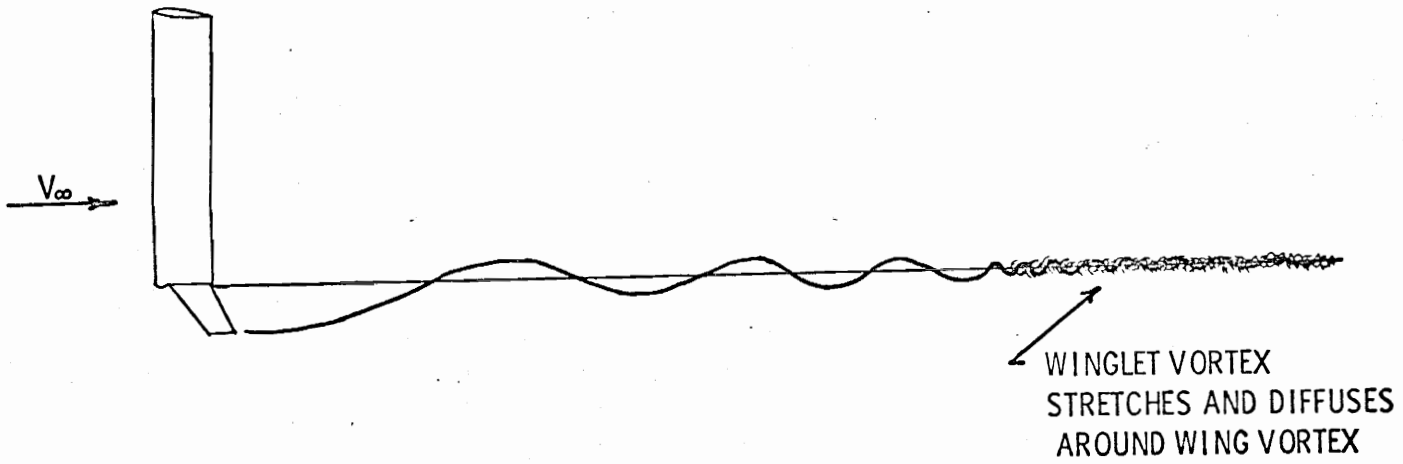

Fig. 69. Wing/Winglet Vortex Interaction.

VITA

Lieutenant Colonel Henry F. Faery, Jr., was born December 10, 1938 in Tampa, Florida. He graduated from the United States Military Academy, West Point, New York on June 8, 1960, and was commissioned a Second Lieutenant of Infantry in the U.S. Army. In August 1969, between two tours of duty in combat units in Vietnam, he received a degree of Master of Science in Aeronautical Engineering from Massachusetts Institute of Technology. He then taught in the Department of Mechanics at West Point from 1970-1974. LTC Faery was an Instructor in Fluid Mechanics, an Assistant Professor teaching Applied Aerodynamics, and finally an Associate Professor in charge of instruction in the Aero-Mechanics Group. Prior to initiation of his studies at Virginia Polytechnic Institute and State University, LTC Faery attended a one year course at the Marine Command and Staff College, Quantico, VA. Following completion of his studies at VPI and SU, he will return to West Point to continue instruction in the Department of Mechanics.

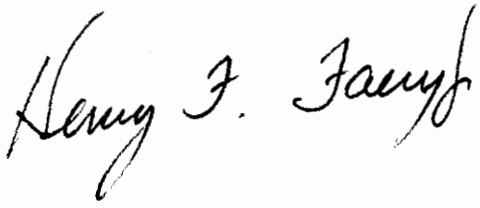

THE EFFECT OF WHITCOMB WINGLETS AND OTHER WINGTIP MODIFICATIONS ON WAKE VORTICES

by

Henry Frederick Faery, Jr.

(ABSTRACT)

Wind tunnel experiments have been conducted on six different wingtip configurations to determine their wake vortex characteristics. The trailing wingtip vortex was probed by a 1/8 inch diameter five hole yawhead pressure probe in the VPI & SU Stability Wind Tunnel. The vortex tangential and axial velocity profiles are compared at five and twenty chordlengths downstream.

Primary focus is placed on the Whitcomb winglet and its individual components, the upper winglet alone and the lower winglet alone. It is shown that the Whitcomb winglet and the upper winglet configuration both produce two distinct vortices of the same rotation. The maximum tangential velocity in each vortex is about 64 percent less than that produced by a conventional wingtip configuration. The axial velocity profiles exhibit strong velocity deficits throughout the vortex core.

Aerodynamic force tests were conducted to compare the lift and drag characteristics of the wingtip configurations. Both the Whitcomb winglet and the upper winglet configuration have a remarkable ability to increase the lift-drag ratio and reduce the drag coefficient.

Further tests were conducted to determine the aerodynamic force effects of the wing on the winglet and the winglet on the wing.

Also included is an analytical study to determine the downwash distribution on the wing both with and without winglets. An experimentally-obtained spanwise pressure distribution is employed in this theoretical approach. A simple application of the Biot-Savart law also analyzes the effect of different winglet dihedral angles on the wing downwash pattern.

It is concluded that the upper winglet configuration, although primarily designed to improve aerodynamic efficiency, also shows promise as a wake alleviation device. It produces two distinct, low intensity vortices of like sign. One vortex shows a tendency for early decay.